Università degli Studi di Cagliari

PHD DEGREE

Ingegneria elettronica ed informatica - Indirizzo "Elettronica e Telecomunicazioni"

Cycle XXXI

TITLE OF THE PHD THESIS

Innovative ISM and Diagnostic Applications of Microwaves

Scientific Disciplinary Sector

ING-INF/02

PhD Student: **Sergio Casu**

Coordinator of the PhD Programme **Fabio Roli**

Supervisor **Giuseppe Mazzarella**

Final exam. Academic Year 2017 – 2018

Thesis defence: January-February 2019 Session

Innovative ISM and Diagnostic Applications of Microwaves

Sergio Casu

Abstract

The widest employment of electromagnetic (EM) waves is probably in the telecommunication area. Nevertheless, the potential of electromagnetism goes beyond telecommunication and can find application in a variety of fields. Structures such as antennas and resonant cavities allow the generation of well-known EM fields that is possible to use in a controlled way. In this thesis, different uses of EM field are proposed, involving different areas. As a high power application, in the agriculture sector, a model to evaluate the feasibility of using EM waves to disinfect the superficial layer of the soil is presented. The variation of the dielectric constant due to the raise in temperature is taken into account and power and time of irradiation to obtain the desired profile of temperature of the soil is determined. A medium power application uses a resonant cavity as a (temperature) controlled environment in which an enzymatic reaction takes place in an aqueous solution. The yield of the reaction is compared with the yield obtained using conventional heating. As a low power application, healthcare sector is considered, and the design of an array of coil on a flexible substrate for magnetic resonance is presented. Furthermore, a numerical evaluation of the EM field, inside a full blood bag, is carried out, to compare it with the EM field generated by an RFID reader intended to be used for identification of blood bags.

Contents

1. Introduction

In these days electromagnetics is present in most aspects of our life. Electromagnetic waves have been studied since the XIX century and in the past century, the advances in different technological fields has brought to a widespread use of electromagnetics. Besides, electromagnetic waves have different characteristics and behavior and interact differently with the matter depending on their frequency (or wavelength). Therefore, for their nature, they can be used in very different ways and applications [1].

In figure 1.1 it is shown that the electromagnetic spectrum includes radio and microwaves, as far as infrared, visible light, ultraviolet and high energy waves such as X-rays and gamma rays, each of which can have application in various fields [2].

In the visible spectrum for example, sources of light, such as incandescent or fluorescent bulbs, have been used for over a hundred years for lighting homes, buildings and streets while today the more energy efficient LEDs (**L**ight **E**mitting **D**iodes) are replacing them. The same principles on which are based LEDs can be used to build LASERs (**L**ight **A**mplification by **S**timulated **E**mission of **R**adiation), a coherent source of light that can be used in telecomunication (as signal source for optical fibers), or for mechanical manufacturing (cut, soldering, etc...) or even in medical field such as for laser eye surgery. X-ray radiations also have medical application and can be used for radiography, which is a 2D mapping of the absorpion of a part of the body, or the more sophisticated Computer Tomography (also know

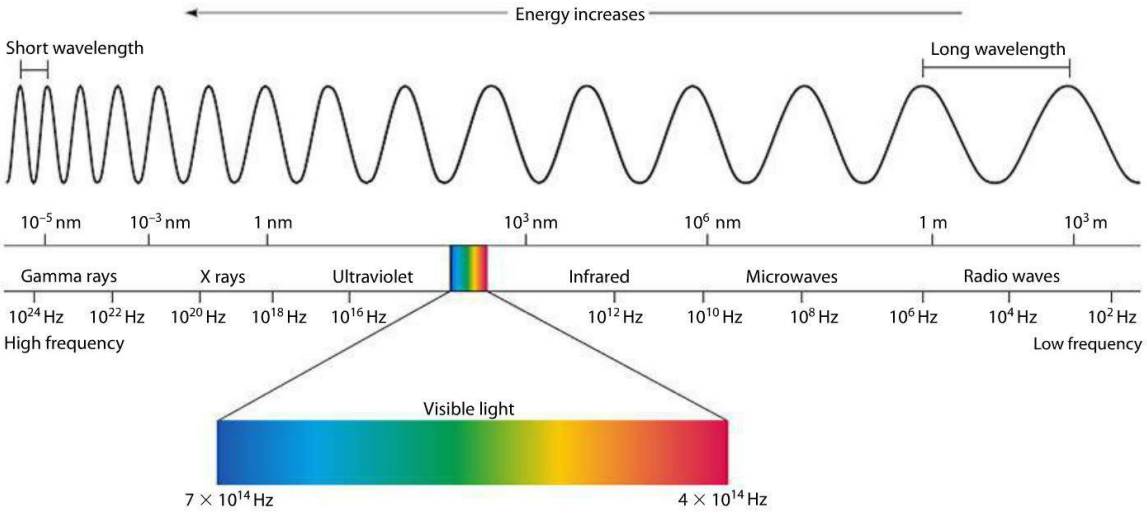

Figure 1.1 Electromagnetic spectrum

as CT scan) which allows to obtain a 3D mapping of the body. Infrared application have mainly military application, such as search and target acquisition, localization and tracking, identification and recoinnance, weapon guidance or self-guidance. Outside of the military applications, infrared technology are used to the detection of tumors, to inspection functionality in industrial production such as temperature control and measurements, or in the field of security and environment protection such as detection of intruders or measurement and monitoring of pollution.

Microwave spectrum has been used mainly for telecommunication purposes [2]. The propagating characteristics of the electromagnetic waves at these frequencies allows to transmit information over long distances. A point-to-point transmission in line-of-sight has very good performances. To overcome the roundness of the earth for very long distances, a number of repeaters can be used, installed approximately every 50 km, and a radio link is obtained. Exploiting the propagation in the troposphere, it is possible to create a radio link without the use of repeaters beyond the optical horizon, but the reception is weak and fluctuating. To get through this problem, satellite have been used as repeater to achieve longer distances with a reduced number of repeaters.

Another important application of microwaves is a RADAR system (**RA**dio **D**etection **A**nd **R**anging), which is a system that transmits electromagnetic waves in a given part of space and receives the waves reflected by the various targets, with the aim to obtain information about them, such as horizontal position, their height, their speed and possibly their shape. Radar systems were born for detecting aircrafts and had a development for military purposes. Over the years the increasing processing

power allowed to obtain better performance and new features such as automatic target tracking. Even if a radar, to be capable of detecting targets at very long distances, needs to use very high power, it is more a telecommunication application due to the importance of the processing of received signals to obtain information on the target.

Another field of application is in the study of signals coming from the universe which is the aim of radioastronomy. Radio emission due to remote celestial object are as weak as $10^{-12}\,\mu W$. The cosmic radiation extends from the γ-rays, X-rays and ultraviolet rays through the optical and infrared domain, to radio waves. most of the cosmic radiation in the electromagnetic spectrum is absorbed by the water vapour and carbon dioxide in the atmospheric layers or reflected back in space by the ionosphere, surrounding the earth. Only a few narrow *windows* in the visible, infrared and radio wavelengths allow us to peer at the sky from the earth. The radio astronomical bands range from 10 MHz to 300 GHz and can be detected by large modern radio telescopes which provide both high angular resolution and sensitivity.

Other important applications of microwaves goes under the name of **I**ndustrial, **S**cientific and **M**edical (ISM) applications. The International Telecommunication Union's (ITU) Radio Regulations (RR) [3] defines

> **ISM Applications**: Operation of equipment or appliances designed to generate and use locally radio frequency energy for industrial, scientific, medical, domestic or similar purposes, excluding applications in the field of telecommunications

Industrial applications are typically related to microwave heating [4]. When a material containing water is exposed to microwaves, the water molecules (which have an electric dipole) rotate so as to align their own dipole along the oscillating field direction so that the energy of the field is converted into thermal energy. To evaluate the increase of temperature, a good knowledge of the field distribution and the heat parameters are required to solve the heat transfer equation. Microwave heating leads to a quicker heating than with conventional processes (the penetration is much greater than in infrared so the heating process is more advantageous than with hot air).

Medical applications are mainly related to hypertermia therapy, for the treatment of cancer. In this process, the aim is to bring the tumors tissues to a temperature of 43 °C. To avoid superficial burns and to allows the heat to go deep up to several centimeters a suitable cooling system for the superficial part of the body (*water bolus* is used.

Scientific application can be very different from each other. An example is in the high energy applications, in which the electromagnetic field is used to supply energy to the system. In a thermonuclear fusion for example, where the plasma needs to be heated up, an electric current is used to induce a magnetic field to confine the plasma and to heat it exploiting Joule effect. In a similar way, particle accelerators uses electromagnetic field of high intensity but low voltage (respect to that required by a Van de Graaf accelerator) to let the particles to achieve high energies.

Finally, different kind of sensor uses electromagnetic waves for various applications. Using active sensors that exploit the doppler effect, volumetric detection (industrial tank gauging), velocity sensor or in general, detection of moving object are possible. On the other hand passive sensor are used in radiometry application, which are mainly used for temperature control such as in hypertermia or industrial processes, or again in medical diagnosis and imaging.

The next of this thesis works presents four different uses of microwaves in fields such as agricultural, industrial chemical processes and medical applications. The agricultural applications is for the disinfection of soils and provides the tools to design a disinfection procedure suitable for a given terrain of known characteristics, for the elimination of a specific bacteria, keeping the temperature to the critical value for the required amount of time.

As industrial application, a resonant cavity is used as a controlled environment, to irradiate a solution in which an enzymatic reaction occurs. The presented design procedure allows to obtain the parameters to set up the system to work at the required temperature, and has as objective to provide an apparatus which allows to relate the electromagnetic field to the kinetic parameters of the reaction considered.

Finally, in the second part, two medical-related applications are presented. In the first one, a flexible (easily adaptable to any body part) array of coils to be used as receiver coils for magnetic resonance imaging is designed and a prototype has been measured to verify its performances. In the second application, the influence of an RFId system, used for blood bag traceability, is examined and a numerical estimation of the field in the blood due to the typical electromagnetic fields produced by the RFId reader has been carried out, considering the raise in temperature due to a continuous exposition (worst case) of the field.

Part I.

Industrial and Scientific Applications

2. Soil Disinfection

Nowadays the scientific community's interest in biological and sustainable agriculture is widespread. "Bio-Agriculture" identifies precise cultivation methods, which allow the exclusive use of natural substances excluding chemical products, namely herbicides and pesticides. The health state of soil is a major concern in bio-agriculture. As a matter of fact, in this dynamic and complex system, many potentially harmful organisms are present. Well-known pathogens are bacteria, nematodes, Streptomycetes and fungi, such as Micrococcus agilis, Pseudomonas fluorescens, Bacillus licheniformis, Radopholus citrophilus, Verticillium dahliae, and Fusarium oxysporum. These biological populations damage the soil equilibrium, consuming nutrients and altering the chemical micro-environment conditions [1–4]. To control, or completely eliminate, the presence of risky and noxious agents, pesticides, e.g., Toxaphene [5], have been traditionally used for a long time. However, chemicals can exert harmful effects on plants, agricultural products, and humans [6] and therefore the current trend is to avoid their use. Different strategies and techniques have been investigated to reach such goal. The most popular is bioremediation, i.e., the pest management using other antagonist biological organisms, e.g., Lumbricus terrestris and Coccinellidae [7–9].

The main alternative to bioremediation is the use of electromagnetic energy, in particular at microwave frequencies, to increase the soil and pathogens temperature, maintaining a high enough temperature for a sufficient time in order to inhibit

Clay	Silt	Sand	Gravel
< 0.002	$0.002 \div 0.05$	$0.05 \div 2.0$	$2.0 \div 50.0$

Table 2.1 Classification of soil granulometric classes (diameter size in mm) (Soil Conservation Service, 1987)

and/or eliminate the soil pathogens without affecting the soil organic properties [1, 10, 11].

The main studies on soil response to microwave irradiation were conducted using radar remote sensing [12–16] and free-space techniques [17, 18] or driving structures, such as rectangular waveguides[19]. Furthermore, the studies on soil irradiation focused on the frequency response of the soil (on the determination of the electric parameters), i.e. the quantification of electric permittivity of several soil layers taking into account the content of water or moisture, [17, 20, 21] but also on the prediction and prevention of possible hydrological phenomena in areas with risk through satellite and geo-radar detection [22].

Regarding agricultural soils, nowadays the issue of the elimination of pathological agents is perceived as fundamental, especially when considering the quality of the cultivated products. In fact, soils are inhabited by very active populations, namely algae, fungi, and fungine roots, but also viruses, nematodes, and, finally, protozoa. Most of them find nutrients within the superficial layers of soil, mainly containing decomposing organic matter and humus. Since many biological species which are present in the soil can be pathogenic, the agricultural soil must be disinfected without affecting the organic nutrients, preserving good flora and fauna and eliminating the aforementioned harmful agents.

The present work provide a procedure to devise the disinfection of a terrain, aimed to the elimination of a known agent, by the knowledge of the physical characteristics of the soil and its moisture.

2.1. Soil Characterization

2.1.1. Physical Soil Properties

Soil is defined as a mixture of fragmented and eroded minerals, of decomposing organic matter and a certain amount of water and air. The main soil components are four and they are listed in Table 2.1. These features, i.e. its composition, influence the soil texture, which is an important characteristic identifying how the

studied ground retains water or moisture, which is a relevant, if not critical, parameter strongly influencing the value of the dielectric constant. Therefore, water and moisture amounts are fundamental quantities in the comprehension of the phenomenon here considered, i.e. soil disinfection. Since soil is a porous medium, it is possible to recognize in its texture macro-pores, which have a diameter greater than 60 µm, and micro-pores, with a diameter less than 10 µm. Typically, for farmland, porosity is around 70%. Such pores can be filled with water or air. If they mainly contain air, the soil can be classified as *dry* or *sandy*; on the other hand, if they are mainly filled in by water, the soil is called *clayey*, i.e. saturated soil. In pores, water can be found in different states: *vapor*, *free* and *bound water*, depending on the soil composition, which influences the affinity between water molecules and solid surfaces, leading to a different response of its electric dipoles to the applied MW energy. Therefore, it is necessary to define the hydrological field capacity (FC) as a function of the water content (*humidity*) in the soil, which varies depending on the ground porosity [20]

$$FC = 25.1 - 0.21 \cdot S + 0.22 \cdot C \tag{2.1.1}$$

where S and C are the percentages of sand and clay, respectively. From FC it is possible to obtain the volumetric amount of water (m_v), simply dividing the water fractional volume by the soil bulk density.

2.1.2. Soil Dielectric Constant

In order to establish the soil behavior under microwave exposition, it is necessary to determine the value of its relative dielectric constant ($\epsilon_s oil$) for humidity ranging from $0 \div 10\%$ (dry soil) to $30 \div 40\%$ (wet soil), and also $50 \div 90\%$ (peat). Usually, the soil behavior under radiation can also be measured using frequency domain or time domain reflectometry. But, since these techniques are expensive, in this work we actually exploited the empirical model developed by Hallikainen [17] and Dobson [23], i.e. equation (2.1.2), to quantify such physical parameter (both the real and the imaginary parts, ϵ'_s and ϵ''_s, respectively):

$$\epsilon_{soil} = (a_0 + a_1 \cdot S + a_2 \cdot C) + (b_0 + b_1 \cdot S + b_2 \cdot C)\, m_v + (c_0 + c_1 \cdot S + c_2 \cdot C)\, m_v^2 \tag{2.1.2}$$

in which a_j, b_j, and c_j are fitting parameters, reported in Table 2.2, which depend on the working frequency, and j refers to the soil component, i.e. 0 for none, 1 for sand, 2 for clay.

For the purpose of this work the temperature dependency, mainly due to the water, needs to be kept into account. To introduce the temperature in the dielectric

Frequency [GHz]		$\epsilon = (a_0 + a_1 \cdot S + a_2 \cdot C) + (b_0 + b_1 \cdot S + b_2 \cdot C) + (c_0 + c_1 \cdot S + c_2 \cdot C)$								
		a_0	a_1	a_2	b_0	b_1	b_2	c_0	c_1	c_2
ϵ'	**1.4**	2.862	-0.012	0.001	3.803	0.462	-0.341	119.006	-0.500	0.633
	4	2.927	-0.012	-0.001	5.505	0.371	0.062	114.826	-0.389	-0.547
ϵ''	**1.4**	0.356	-0.003	-0.008	5.507	0.044	-0.002	17.753	-0.313	0.206
	4	0.004	0.001	0.002	0.951	0.005	-0.010	16.759	0.192	0.290

Table 2.2 Hallikainen coefficients to evaluate real and imaginary part of dielectric constant

constant of soil, a weighted mean of the permittivity of the soil components (air, solid particles and water) has been calculated. For the dielectric constant ϵ_p of the particles, it can be used equation (2.1.2) with null m_v. Unfortunately the coefficients a_j, b_j, and c_j, are not given at the working frequency of 2.45 GHz, so a mean between the values of ϵ_p evaluated at the two frequencies, 1 GHz and 4 GHz, is used. For the dielectric constant of water ϵ_w, the complex model of Ray [24] is used, so that the dependency of the temperature in now introduced. Finally, having the three dielectric constants, a weighted mean is calculated, using as weights the corresponding volume fraction for every component. Let be θ_a, θ_w and θ_p the volume fraction of air, water and particles respectively, and using the same subscripts, be ϵ_a, ϵ_w and ϵ_s the permittivities of the components. Then dielectric constant of the mixture is obtained as

$$\begin{aligned} \epsilon'_{soil}(T) &= \theta_w \epsilon'_w + \theta_s \epsilon'_p + \theta_a \epsilon'_a \\ \epsilon''_{soil}(T) &= \theta_w \epsilon''_w + \theta_s \epsilon''_p \end{aligned} \tag{2.1.3}$$

where, by definition, $\theta_w = m_v$. To determine the volumetric fraction of the solid particles it can be used the porosity P [23], defined as

$$P = 1 - \frac{\rho_b}{\rho_p} \tag{2.1.4}$$

which represents the empty space inside the mixture, where ρ_b is the density of the bulk soil (i.e. dry soil, without water) and ρ_p is the density of the solid particles (i.e. soil without air and water). Knowing the volumetric fractional content of water $\theta_w = m_v$, the space filled by the air is then $\theta_a = P - m_v$ while for the solids $\theta_p = 1 - P$.

2.1.3. Soil Biological Environment

Soil is a living medium, in fact, thanks to water and air circulating in pores, and also to nutrients, it represents a favorable environment for microbial life. Bacteria, fungi, plants, and animals, e.g. invertebrates and small vertebrates, find suitable conditions to survive and reproduce, creating a fragile interacting dynamic system.[3, 25] Each of them has a specific role, function, and position in the soil matrix, but it is necessary to distinguish between pathological and risky agents [26] (nematodes, fungi, and parasites) and favorable organisms, e.g. earthworms. These biological entities are mainly composed by water, ranging from 80 to 90%, and hence represent a target to MW energy. The studies performed by Komarova [1] underlined that microwaves exert a lethal influence on bacteria, thanks to the remarkable increase in temperature and to the bio-effects of non-ionizing radiations, the explanation of which remains, in part, still unclear [10, 11, 27].

Actually, some harmful agents are able to withstand high temperatures, keeping alive several colonies, even for long times of exposition. Experimental findings show that the treatment efficiency is strictly related to the exposure time, therefore, to reach the lethal temperature, such information should be related to power levels and soil properties, so that future in situ actions can be designed and undertaken[18]. In this study, we assume that the temperature of 60 °C must be reached for about 7 min of exposition within a layer about 3-cm thick, this value was chosen according to the information from Soil Survey Division Staff (1993). Since the temperature would rise with time for a constant microwave applied power, i.e. the heat source within the soil volume, the exposure time has to be carefully regulated for a few minutes by a suitable reduction of the horn power or turning off the generator. But more insight in the critical parameters for the performance of soil disinfection has to be provided.

2.2. Heat Transfer

The main parameter to guarantee the efficiency of the disinfection is the temperature. In this application the temperature is indirectly controlled by means of the electromagnetic field, which is used to supply energy to the soil.

To determine the temperature it is necessary to evaluate how the heat distribute within the soil. Due to the high losses of the soil caused by the presence of water, the field is more intense close to the surface and it vanishes as the depth increases. This leads to a higher heat generation in proximity of the surface and a lower heating deep in the soil. Similarly, the temperature resulting from this heating will follow

the same trend. Intuitively, the gradient of temperature brings to an exchange of heat from the hot zones to the cold deeper zones. The heat flux that occurs in presence of a difference in temperature is due to a phenomenon called ***conduction*** and it is one of the three ways of heat transfer.

While the heating of the soil is underway, there is a difference of temperature between soil and air. If the air is stationary, e.g. no macroscopic motion take place in the fluid, an heat flux would exists through the interface, due to conduction phenomenon. But in general a bulk fluid motion exists. If we assume a motion along the interface, a slowed-down layer of the fluid close to the surface, called *boundary layer*, absorbs heat from the soil, sweeps it downstream and then the heat is mixed on the stream. This carry of heat due to the motion of a fluid is the second mode a heat transfer can occur and is known as ***convection***.

For the sake of completeness, the third mechanism of heat transfer, called ***radiation***, is briefly explained. Every body at a nonzero temperature constantly emits thermal radiation. The energy of this radiation is transported by electromagnetic waves and the intensity of the radiation depends upon the temperature of the body and the nature of its surface. Contrary to conduction and convection, radiation heat transfer doesn't require the presence of a material medium. Actually it is more efficient in vacuum, in which conduction and convection are suppressed. Since the thermal radiation varies as the fourth power of the absolute temperature, this phenomenon can be neglected at low temperatures.

The next sections are devoted to present the formalism to quantify the heat fluxes due to the mechanisms of conduction and convection of heat.

2.2.1. Conduction

It is well known from the thermodynamics that temperature is related to microscopic quantities such as kinetic energy of molecules. Naturally, higher temperature are associated to higher molecular energies and conduction can be seen as the energy transfer from the more energetic to the less energetic particles.

As a straightforward example let's analyze what happens within a gas in which a temperature gradient exists. Consider an imaginary plane orthogonal to the direction of temperature increase, so that on one side of the plane the particles are more energetic than on the other side. Even assuming absence of collisions between the particles, they continuously cross the plane, so that the hottest particles goes to the cooler region and the colder ones goes toward the hotter region. In this situation a *net transfer* of energy take place and the heat goes from the high to the low temperatures. If any collision arises the process is heightened. The tranfer of

energy due to the random motion of the particles is a process of *diffusion* of energy and is governed by the *diffusion equation* [28], which is used to describe a number of physical problems.

The same reasoning is valid for fluids in which molecules are closer to each other and interaction between them are more frequent. In solids, it can still be considered the same effect but in this case the molecules are bounded together and energy exchange is due to lattice vibrations.

For a quantitative analysis of heat flux due to conduction in a medium, from a macroscopic point of view, two experimentally observed behaviors need to be noticed, which where stated by Joseph Fourier in his book *Théorie Analitique de la Chaleur* in 1822, in the empirical law that now bears his name:

> **Fourier Law**: the heat flux, q ($\mathrm{W/m^2}$), resulting from a thermal conduction is proportional to the magnitude of the temperature gradient and opposite to it in sign.

which, if we call k the coefficient of proportionality, can be written as

$$q_x = -k\frac{dT}{dx} \tag{2.2.1}$$

where k is called *thermal conductivity*. A simple dimensional analysis of (2.2.1) reveals that k have to be measured in $\mathrm{W\,m^{-1}\,K^{-1}}$.

Clearly, equation (2.2.1) refers to a 1D stationary case. In the more general case, the temperature depends on position and time, i.e. $T = T(x, y, z, t) = T(\vec{\mathbf{r}}, t)$, and for a fixed time t_i and a constant value of temperature T_j, the equation $T(\vec{\mathbf{r}}, t_i) = T_j$ defines an instantaneous isothermal surface.

To complete the problem in the 3D space, two other equations analogous to (2.2.1) are introduced, for both directions y and z, leading to the system

$$\begin{aligned} q_x &= -k\frac{\partial T(\vec{\mathbf{r}}, t)}{\partial x} \\ q_y &= -k\frac{\partial T(\vec{\mathbf{r}}, t)}{\partial y} \\ q_z &= -k\frac{\partial T(\vec{\mathbf{r}}, t)}{\partial z} \end{aligned} \tag{2.2.2}$$

Now, if we recognize in the heat flux a vector quantity, $\vec{\mathbf{q}} = (q_x, q_y.q_z)$, and using the gradient definition $\nabla = \left(\frac{\partial}{\partial x}, \frac{\partial}{\partial y}, \frac{\partial}{\partial z}\right)$, the previous equation (2.2.2) can be rewritten as

$$\vec{\mathbf{q}} = -k(\vec{\mathbf{r}}, T)\ \nabla T(\vec{\mathbf{r}}, t) \tag{2.2.3}$$

where the thermal conductivity coefficient, k, has been considered in the most general case in which can be function of both position and temperature $k = k(\vec{\mathbf{r}}, T(\vec{\mathbf{r}}, t))$.

Thermal conductivity is a property of the matter that quantify the rate at which energy is transferred by the diffusion process. It is strongly influenced by the structure of the matter and then by its physical state. In general the thermal conductivity of a solid is larger than that of a liquid, which is larger than that of a gas. In the equations (2.2.2), the implicit assumption of isotropic material has been done, which means that thermal conductivity has been considered the same in every direction, $k_x = k_y = k_z = k$. Another common property of most materials is that they are nearly homogeneous, so that $k = k(T)$, is independent of the position. Unfortunately, the temperature dependency is strong, unless to consider a very restricted range of temperature. Usually, thermal conductivity of gases increase with temperature at low pressures, while it may raise or fall for liquids and solids. In any case, k needs to be determined to solve (2.2.3).

The three dimensional expression of Fourier Law alone (2.2.3) is not enough to solve heating problems and require some additional considerations. In particular, since heat flux and temperature depend on each other, a method to eliminate heat flux from the equation is required.

To solve this situation, the *First Law of Thermodynamics* comes to help, that states:

> **First Law of Thermodynamics** : Energy cannot be created or destroyed in an isolated system.

where an *isolated system* is a system that can't exchange matter or energy (work or heat) with the outside. Of course an isolated system is very restrictive, and in practice we find *closed systems*, which can't exchange matter with the outside but energy is allowed, or *open systems*, which can exchange matter and energy. If the former is considered, the first law can be written [29], in a rate basis (i.e. over the time), as

$$Q = W + \frac{dU}{dt} \tag{2.2.4}$$

where Q is the heat exchanged, W is the work done by (or on) the system and U is the internal energy of the system. Both Q and W are measured in J/s or W, while U is measured in J. The term dU/dt is the rate of change of internal thermal energy over time.

In the (2.2.4), work can assume different expressions. For example, if the only work considered is due to compression or expansion of a gas, it assumes the well known form $p\,dV$, where p is the pressure and dV is the change in volume. In the

special case in which no work is done (i.e. constant volume), equation (2.2.4) says that the heat transfer is due only to the change in internal energy.

As stated previously in the chapter, temperature is related to the energies of molecules, the sum of which yields the internal energy of the system. That said, it is possible to express the internal energy in function of the temperature of the system. Actually, the internal energy of a complex system can't be measured, but using the definition of a closed system (wtih no work), it can be said that to an amount of heat given to the system, corresponds an increase of internal energy so that a raise of temperature is observed. Even if we can't measure the internal energy, its variation can be quantified as the amount of heat given to the system. The ratio between the heat supplied to the system and the reciprocal raise in temperature, for a given amount of matter, m, is a property of the matter [30]

$$C = \frac{Q}{\Delta T} \qquad [\mathrm{J/K}] \tag{2.2.5}$$

and is called *heat capacity* or *thermal capacity*. This quantity is an *extensive property*, which means that it depends on the amount of matter considered, but it can be expressed per unit of mass, making it an *intensive property*, which is called *specific heat capacity*

$$c = \frac{Q}{m\Delta T} \qquad [\mathrm{J\,kg^{-1}\,K^{-1}}] \tag{2.2.6}$$

With this definition in mind, and taking into account equation (2.2.4) with zero work, we can relate the internal energy of the system to the change in temperature

$$Q = \frac{dU}{dt} = mc\frac{dT}{dt} \tag{2.2.7}$$

which is the relation being sought.

Now considering a finite volume R, delimited by its surface S, with outward unit normal vector $\vec{\mathbf{n}}$, the heat flux leaving the region through an infinitesimal element of surface dS can be written as

$$(-k\nabla T) \cdot (\vec{\mathbf{n}} dS) \tag{2.2.8}$$

Inside the volume, a generation (or consumption) of heat can take place. For example, if an external electromagnetic field is applied, it causes an heating of the volume, which has to be considered in the heat balance. Referring to this term as

$P(\vec{\mathbf{r}})$ [W/ m^3] the heat collected in the region R is

$$Q = -\oint_S (-k\nabla T)\cdot(\vec{\mathbf{n}}dS) + \int_R P\,dR \tag{2.2.9}$$

Using equation (2.2.7), referred to an infinitesimal element of volume dR, and introducing the density of the matter ρ [kg/ m^3]

$$dQ = \left(\frac{dm}{dR}\right) c\frac{dT}{dt}dR = \rho c\frac{dT}{dt}dR \tag{2.2.10}$$

the rate of energy increase in the whole volume becomes

$$Q = \int_R \rho c\frac{\partial T}{\partial t}dR \tag{2.2.11}$$

where the partial derivative is used because T is function of both $\vec{\mathbf{r}}$ and t. Combining (2.2.11) with (2.2.9) we obtain

$$\int_R \rho c\frac{\partial T}{\partial t}dR = \oint_S (k\nabla T)\cdot(\vec{\mathbf{n}}dS) + \int_R P\,dR \tag{2.2.12}$$

Now using the *divergence theorem* which states that for any continuous function of position $\vec{\mathbf{A}}$ the following equivalence stands

$$\oint_S \vec{\mathbf{A}}\cdot\vec{\mathbf{n}}\,dS = \int_R \nabla\cdot\vec{\mathbf{A}}\,dR \tag{2.2.13}$$

equation (2.2.12) becomes, after rearranging [29]

$$\int_R \left(\nabla\cdot k\nabla T - \rho c\frac{\partial T}{\partial t} + P\right) dR = 0 \tag{2.2.14}$$

The final step is to notice that equation (2.2.14) to be true in any arbitrary region R needs its integrand to vanish, so that

$$\rho c\frac{\partial T}{\partial t} = \nabla\cdot(k\nabla T) + P \tag{2.2.15}$$

which is the *heat conduction equation* in a three dimensional space. It is worth to remember that (2.2.15) holds under the assumption of

- *incompressible medium*, which means that no work due to expansion/compression have to exist

- *no convection*, meaning that the medium can be a liquid or a gas but it needs to still, no bulk motion exists.

If k is independent or has very little variation with the position, then it can be factored out of the divergence and the heat equation becomes

$$\rho c \frac{\partial T}{\partial t} = k\nabla^2 T + P \tag{2.2.16}$$

where the *Laplacian* operator $\nabla^2 T = \nabla \cdot \nabla T$ has been used.

2.2.2. Convection

In presence of a fluid (liquid or gas) flowing on a surface, in addition to the conductive heat transfer due to random motion of molecules, a further exchange of heat between the surface and the fluid occurs, due to the bulk motion and to the difference of temperature between them. The cumulative effects due to random motion and bulk motion is called *convective* heat transfer, while the only effect due to the bulk motion is called *advection*.

When the fluid is in motion respect to a bounding surface, close to the surface the velocity of the fluid needs to be zero, which means that in this region conductive heating exists and is dominant. Moving away from the surface a gradual increase of the velocity is observed, up to a value u_∞ characterizing the fluid motion. This region of variable velocity is referred as *velocity boundary layer*. Furthermore, if a difference of temperature exists between the surface temperature T_s and the temperature of the fluid stream T_∞, then a region, called *thermal boundary layer*, in which the temperature varies between T_s and T_∞ is present, that can be of different size as that through which the velocity varies. If $T_s > T_\infty$, a convective heat transfer arise from the surface to the outer flow. It is clear that what happens in the velocity boundary layer depends on the surface properties as well as on the flow characteristics which strongly influences the heat transfer, and that's the reason why fluid dynamics needs to be used to define the behavior of the fluid.

There are different ways how convective heat transfer can occurs, depending on how the flux is generated, and can be classified as *forced* convection, *free* or *natural* convection, and the last *mixed* convection which is a combination of the other two. Forced convection is obtained using external means such as fans or pumps. On the other hand, free convection is not externally generated, but it arises as a consequence of the body forces due to the density changes as a result of the changes in temperature in the flow. These forces are actually generated by the pressure gradients enforced on the whole fluid. The main player of these imposed

forces, called *buoyancy forces*, is the gravity and so the pressure gradient is the normal hydostatic pressure gradient existing in every bulk fluid. The term *forced convection* refer to the convective heating that take place when the bouyancy forces can be neglected. If these forces are comparable to other applied forced velocities in the fluid, then it's called a mixed free and forced convection. The types of convection considered this far doesn't take into account phase changes, such as boiling or condensation, which can increase or decrease the amount of heat involved. Regardless of the nature of the convection process, the following rate equation [28] describes the heat flux exchange

$$q = h\left(T_s - T_\infty\right) \tag{2.2.17}$$

which is knonw as *Newton's law of cooling* and states that the heat flux q ($\mathrm{W/m^2}$) is proportional to the difference of temperature of the surface T_s and the temperature of the fluid T_∞, being h ($\mathrm{W\,m^{-2}\,K^{-1}}$) the coefficient of proportionaly which is called *convection heat transfer coefficient*.

To evaluate the h coefficient, the knowledge of the surface and the characteristics of the fluid are required. Among the others, transport properties, such as thermal conductivity k and kinematic viscosity ν and thermodynamic properties such as the density ρ and the specific heat capacity c of the fluid are required. Besides, the velocity u and the nature of the fluid motion relative to the surface has to be known, whether it is a laminar or a turbulent flow.

The determination of the convective coefficient is the main problem in the study of convective heat transfer, so that analytical and numerical methods have been developed to calculate it. Despite everything, to assess the h coefficient is a complex task and many situations still remain in which the prediction of the coefficient requires to use experimental data.

Equation (2.2.17) is a local equations, and h and the temperatures varies with the position. Usually, it is useful to define an overall convection coefficient $\bar{h}$, such that, if Q is the total heat transfer rate from the surface A, then

$$Q = \bar{h}A\left(\bar{T}_s - \bar{T}_\infty\right) \tag{2.2.18}$$

where $\bar{T}_s$ and $\bar{T}_\infty$ are the mean temperature of the surface and the fluid respectively.

When the convection coefficient is known, the equation (2.2.17) can be used as a boundary condition for the conduction problem. In Table 2.3, typical ranges of values for the different types of convection are given.

Process	h $(\mathrm{W\,m^{-2}\,K^{-1}})$
Free convection	
Gases	2–25
Liquids	50–100
Forced convection	
Gases	25–250
Liquids	100–20000
Convection with phase change	
Boiling or condensation	2500–100000

Table 2.3 Tipical values of convective heat transfer coefficient

2.2.3. Electromagnetic Heating

While deriving equation (2.2.15), the effect of energy generation inside the volume V has taken into account including the term P. In the general case, this term is variable with position so an expression is required to solve the equation.

If the region is subjected to an external electromagnetic field, the term P is strictly connected with the electric field $\vec{\mathbf{E}}$. To determine the relationship between the two quantities, the following entity [31] is used

$$\vec{\mathbf{S}} = \frac{1}{2}\vec{\mathbf{E}} \times \vec{\mathbf{H}}^* \qquad [\mathrm{W/m^2}] \tag{2.2.19}$$

which is known as *Poynting vector*, expressed in the frequency domain. As the measure unit suggests, being a power density, it is related somehow to the energy supplied by the electromagnetic field. Considering the same region R used in section 2.2.1, delimited by the surface S, the flux of $\vec{\mathbf{S}}$ through the surface can be calculated using the divergence theorem

$$\oint_S \vec{\mathbf{S}} \cdot \vec{\mathbf{n}}\, dS = \int_R \nabla \cdot \vec{\mathbf{S}}\, dR \tag{2.2.20}$$

and developing the divergence

$$\nabla \cdot \vec{\mathbf{S}} = \frac{1}{2}\nabla \cdot \left(\vec{\mathbf{E}} \times \vec{\mathbf{H}}^*\right) = \frac{1}{2}\left[\left(\nabla \times \vec{\mathbf{E}}\right) \cdot \vec{\mathbf{H}}^* - \left(\nabla \times \vec{\mathbf{H}}^*\right) \cdot \vec{\mathbf{E}}\right] \tag{2.2.21}$$

Substituting Maxwell's equations in the form

$$\begin{aligned} \nabla \times \vec{\mathbf{E}} &= -j\omega\mu\vec{\mathbf{H}} \\ \nabla \times \vec{\mathbf{H}} &= j\omega\epsilon\vec{\mathbf{E}} + \sigma\vec{\mathbf{E}} \end{aligned} \tag{2.2.22}$$

and separating ϵ in its real and imaginary part, $\epsilon = \epsilon_1 - j\epsilon_2$, equation (2.2.21) becomes

$$\begin{aligned} \nabla \cdot \vec{\mathbf{S}} &= \frac{1}{2}\left(-j\omega\mu\vec{\mathbf{H}} \cdot \vec{\mathbf{H}}^* + j\omega\epsilon_0\left(\epsilon_1 + j\epsilon_2\right)\vec{\mathbf{E}}^* \cdot \vec{\mathbf{E}} - \sigma\vec{\mathbf{E}}^* \cdot \vec{\mathbf{E}}\right) = \\ &= \frac{1}{2}\left(-j\omega\mu\left|\vec{\mathbf{H}}\right|^2 + j\omega\epsilon_1\left|\vec{\mathbf{E}}\right|^2 - \omega\epsilon_2\left|\vec{\mathbf{E}}\right|^2 - \sigma\left|\vec{\mathbf{E}}\right|^2\right) \end{aligned} \tag{2.2.23}$$

that integrating on R and taking into account equation (2.2.20) yields

$$\begin{aligned} \oint_S \vec{\mathbf{S}} \cdot \vec{\mathbf{n}}\, dS = &- j\,2\omega \int_R \left(\frac{1}{4}\mu\left|\vec{\mathbf{H}}\right|^2 - \frac{1}{4}\epsilon_1\left|\vec{\mathbf{E}}\right|^2\right) dR + \ldots \\ &\ldots - \frac{1}{2}\int_R \omega\epsilon_2\left|\vec{\mathbf{E}}\right|^2 dR - \frac{1}{2}\int_R \sigma\left|\vec{\mathbf{E}}\right|^2 dR \end{aligned} \tag{2.2.24}$$

The previous equation can be interpreted as a power balance equation. The left-hand side is the integral of a flux of power density, that flow outward the volume. In the first term of the right-hand side instead, we can recognize inside the brackets the difference between magnetic and electric energies stored, while the remaining terms are the energies dissipated due to joule effect. In fact, if we call $\vec{\mathbf{S}_r}$ the real part of the poynting vector, the real part of equation (2.2.24), rewritten as

$$\begin{aligned} -\oint_S \vec{\mathbf{S}_r} \cdot \vec{\mathbf{n}}\, dS = \int_R \frac{1}{2}\,\omega\,\epsilon_{2,\text{eff}}\left|\vec{\mathbf{E}}\right|^2 dR = \int_R \frac{1}{2}\,\sigma_{\text{eff}}\left|\vec{\mathbf{E}}\right|^2 dR \\ \epsilon_{2,\text{eff}} = \epsilon_2 + \frac{\sigma}{\omega} \\ \sigma_{\text{eff}} = \omega\epsilon_2 + \sigma \end{aligned} \tag{2.2.25}$$

stats that the active power entering the volume R is dissipated in the same region. The two effects of losses in the dielectric and conductivity are put together as an effective imaginary part of the dielectric constant $\epsilon_{2,\text{eff}}$, or an equivalent conductivity σ_{eff}.

Going back to the heat equation (2.2.15), the effect of volumetric heat generation owed to the electromagnetic field can be expressed as the integrand of one of the

two integrals in equation (2.2.25), so that

$$P(\vec{\mathbf{r}},T)=\frac{1}{2}\,\omega\,\epsilon_{2,\mathrm{eff}}\,(T)\left|\vec{\mathbf{E}}(\vec{\mathbf{r}})\right|^2=\frac{1}{2}\,\sigma_{\mathrm{eff}}(T)\left|\vec{\mathbf{E}}\,(\vec{\mathbf{r}})\right|^2 \tag{2.2.26}$$

which reveals that to solve the heat equation, besides the expression of the effective conductivity, the knowledge of the electric field is also required.

2.3. Electromagnetic Background

Irradiation of the terrain requires the generation of an electromagnetic field. The most effective devices able to generate electromagnetic fields are guided structures, resonant cavities and antennas. The first two are closed structure, and would require to place the soil sample within the equipment, which is unacceptable. Antennas, on the other hand can be used to generate an electromagnetic field in an open environment, can be directed toward the soil we want to irradiate and, if the physical dimensions allows it, can be easily moved.

The field generated by an antenna is a complicated function, and usually to obtain an analytical expression, different approximations have to be used. Depending on these approximationd the field is classified in two main categories, the *near-field* and the *far-field*. The former is the field around the antenna where the energy is stored statically in the spatial region surrounding the antenna. Conversely, the latter take places away from the antenna and it has propagative behavior, travels away from the antenna and it will keep to exist even if the antenna is turned off. The far field region, called *Fraunhofer zone*, is defined as the spatial region where the distance of a point from the antenna respects the following conditions

$$\begin{aligned} r &> \frac{2D^2}{\lambda} \\ r &\gg D \\ r &\gg \lambda \end{aligned} \tag{2.3.1}$$

where D is the diameter of the smaller sphere that can contain the antenna while λ is the wavelength. Obviously the transition between near-field and far-field is not abruptly, so a region exists where the far-field gradually predominates on the near-field.

In the Fraunhofer zone, the field propagates as a spherical wave, which locally (i.e. in any point of a wavefront) behaves like a plane wave. So, if the hypothetical receiver is far enough from the antenna such that from any point of its body it sees

a plane wavefront, the problem can be simplified so that the spherical wave can be treated as a plane wave.

2.3.1. Plane Waves

A plane wave is a solution of the Maxwell's equations in the case of absence of sources and characterized by the wavefront to be a plane orthogonal to the direction of propagation. Under the following assumption

- isotropic medium, which means that ϵ and μ are scalars (instead of matrices)
- homogeneous and non-dispersive medium in space, that brings ϵ and μ to be independent on position
- homoeous medium in time, which allows to express ϵ and μ as the Fourier transform of the Green function of the medium

the Maxwell's equations in the frequency domain becomes

$$\nabla \times \vec{\mathbf{E}} = -j\omega\mu\vec{\mathbf{H}} \qquad \epsilon\nabla \cdot \vec{\mathbf{E}} = 0 \tag{2.3.2}$$

$$\nabla \times \vec{\mathbf{H}} = j\omega\epsilon\vec{\mathbf{E}} \qquad \mu\nabla \cdot \vec{\mathbf{H}} = 0 \tag{2.3.3}$$

where ϵ and μ are intended to be evaluated at frequency f_0, so are constants.

Looking for a solution of the electric field that is constant on every plane orthogonal to a generic direction identified by the vector $\vec{\mathbf{k}}$, and remembering that in a 3D space the equation of a plane is

$$\xi\left(\vec{\mathbf{r}}\right) = \vec{\mathbf{k}} \cdot \vec{\mathbf{r}} = const \tag{2.3.4}$$

the electric field solution $\vec{\mathbf{E}}$ is a function of ξ, such that

$$\vec{\mathbf{E}}(\vec{\mathbf{r}}) = \vec{\mathbf{E}}^{+}e^{-j\xi} + \vec{\mathbf{E}}^{-}e^{j\xi} = \vec{\mathbf{E}}^{+}e^{-j\vec{\mathbf{k}}\cdot\vec{\mathbf{r}}} + \vec{\mathbf{E}}^{-}e^{-j(-\vec{\mathbf{k}})\cdot\vec{\mathbf{r}}} \tag{2.3.5}$$

where $\vec{\mathbf{E}}^{\pm}$ are two complex constant vectors. The solution (2.3.5) is the sum of two terms, each being a plane wave, of *amplitude* $\vec{\mathbf{E}}^{\pm}$ and direction of propagation defined by the so called *propagation vector* $\pm\vec{\mathbf{k}}$, where the sign + is referred to a wave propagating forward, along $\vec{\mathbf{k}}$, and the sign − is for the wave propagating backward in the direction of $-\vec{\mathbf{k}}$. The propagation vector verifies the condition

$$\vec{\mathbf{k}} \cdot \vec{\mathbf{k}} = \omega^2\epsilon\mu \tag{2.3.6}$$

The corresponding $\vec{\mathbf{H}}$ field of a plane wave can be determined by the knowledge

of $\vec{\mathbf{E}}$

$$\vec{\mathbf{H}} = \frac{1}{\omega\mu}\vec{\mathbf{k}} \times \vec{\mathbf{E}} \tag{2.3.7}$$

All the equation of this section hold in the case of $\vec{\mathbf{k}}$ being complex. From equation (2.3.6) it can be seen that if ϵ is complex, than the propagation vector is complex too. In this situation it can be expressed as

$$\vec{\mathbf{k}} = \vec{\boldsymbol{\beta}} - j\vec{\boldsymbol{\alpha}} \tag{2.3.8}$$

where $\vec{\boldsymbol{\beta}}$ is a real vector that plays the role of the vector defining the direction of propagation, while $\vec{\boldsymbol{\alpha}}$ is also a real vector but identifies the direction on which the wave attenuates, as can be seen by the following

$$\vec{\mathbf{E}} = \vec{\mathbf{E}}^{+}\ e^{-j\vec{\mathbf{k}}\cdot\vec{\mathbf{r}}} = \left(\vec{\mathbf{E}}^{+}\ e^{-\vec{\boldsymbol{\alpha}}\cdot\vec{\mathbf{r}}}\right) e^{-j\vec{\boldsymbol{\beta}}\cdot\vec{\mathbf{r}}} \tag{2.3.9}$$

where the term within the brackets is the amplitude of the wave and is now attenuated by the exponential term. If the two vectors are parallel, then the wave is called *homogeneous*, and it propagates and attenuates along the same direction. If the direction of $\vec{\mathbf{k}}$ is explicited by a unit vector $\vec{\mathbf{u}}_k$, so that $\vec{\mathbf{k}} = k\vec{\mathbf{u}}_k$, equation (2.3.7) can be written as

$$\begin{aligned} \vec{\mathbf{H}} &= \frac{1}{\zeta}\vec{\mathbf{u}}_k \times \vec{\mathbf{E}} \\ \zeta = \frac{\omega\mu}{k} &= \frac{k}{\omega\epsilon} = \sqrt{\frac{\mu}{\epsilon}} \quad [\Omega] \end{aligned} \tag{2.3.10}$$

where ζ, the *characteristic impedance* of the medium, has been introduced. It is easy to see that it is the ratio between the magnitude of electric and magnetic field

$$\zeta = \frac{\left|\vec{\mathbf{E}}\right|}{\left|\vec{\mathbf{H}}\right|} \tag{2.3.11}$$

The definition (2.2.19) can be used to obtain information on how the flux of power of a plane wave behaves. Substituting the expression of electric and magnetic field,

the Poynting vector is

$$\begin{aligned}\vec{\mathbf{S}} &= \frac{1}{2}\left[\vec{\mathbf{E}}_0\ e^{-j\vec{\mathbf{k}}\cdot\vec{\mathbf{r}}}\right] \times \left[\frac{1}{\omega\mu}\vec{\mathbf{k}} \times \vec{\mathbf{E}}_0\ e^{-j\vec{\mathbf{k}}\cdot\vec{\mathbf{r}}}\right]^* = \\ &= \frac{\left|e^{-j\vec{\mathbf{k}}\cdot\vec{\mathbf{r}}}\right|^2}{2\omega\mu}\ \vec{\mathbf{E}}_0 \times \vec{\mathbf{k}}^* \times \vec{\mathbf{E}}_0^* = \\ &= \frac{\left|e^{-j\vec{\beta}\cdot\vec{\mathbf{r}}}\right|^2 \left|e^{-\vec{\alpha}\cdot\vec{\mathbf{r}}}\right|^2}{2\omega\mu}\ \left[\left|\vec{\mathbf{E}}_0\right|^2 \vec{\mathbf{k}}^* - (\vec{\mathbf{k}}^* \cdot \vec{\mathbf{E}}_0)\ \vec{\mathbf{E}}_0^*\right]\end{aligned} \tag{2.3.12}$$

For an homogeneous wave $\vec{\mathbf{k}} = k\vec{\mathbf{u}}_k$, where $\vec{\mathbf{u}}_k$ is a real unit vector, and $\vec{\mathbf{k}}^* \cdot \vec{\mathbf{E}}_0 = 0$. So for an homogeneous plane wave the Poynting vector assume the form

$$\vec{\mathbf{S}} = \frac{k^*}{2\omega\mu}\left|\vec{\mathbf{E}}_0\right|^2 e^{-2\vec{\alpha}\cdot\vec{\mathbf{r}}}\ \vec{\mathbf{u}}_k = \frac{\left|\vec{\mathbf{E}}_0\right|^2}{2\zeta^*} e^{-2\alpha\vec{\mathbf{u}}_k\cdot\vec{\mathbf{r}}}\ \vec{\mathbf{u}}_k \tag{2.3.13}$$

where, in absence of losses, ζ^* is a real quantity, so that $\vec{\mathbf{S}}$ is a real vector too, meaning that only a flux of active power is associated to the plane wave and its direction of propagation is inherited by $\vec{\mathbf{k}}$.

2.4. Model Description

Despite the use of microwaves for soil disinfection has been presented in other scientific works, the problem is kept just as experimental work and there is a lack of a model that allows to foresee the temperature response of the soil subjected to a known electromagnetic field. The present section is devoted to develop a numerical model that tries fill this void. The model solves the heat equation for the soil in the presence of an irradiating electromagnetic field. The coupling between heat equation and electromagnetic phenomena makes the problem a complex one. To keep it simple (and then more usable), an approach that separates the dynamics of the heat and the electromagnetic field is proposed.

The study of electromagnetic soil heating can be carried out solving the heat equation inside the soil. The problem can be modeled assuming the soil to be on the half-space $z > 0$, and an incident plane wave with angular frequency ω and amplitude $\vec{\mathbf{E}}_i = E_i\vec{\mathbf{u}}_y$, propagating along the positive z-direction, orthogonal to the surface of the soil.

The input impedance of the soil is different from the free space one, therefore, to avoid a high reflected power, a suitable matching network is necessary. It can be obtained using a grid made of metallic rods disposed parallel to each others at an

appropriate distance. The grid is then placed parallel to the soil at a given distance. This structure acts as a series reactance, and for a suitable distance between the bars and from the soil allows to maximize the absorbed power from the soil.

In addition, to avoid dispersion of power due to the side lobes of the antenna, a conical or piramidal structure needs to be used, equipped on the wall, with absorbent material, which delimits the volume where the irradiation occurs and avoid the power due to the side lobes to harm people or plants in the surrounding.

Under these conditions the irradiated power from the antenna (from the main lobe) can be assumed to be absorbed by the soil (thanks to the matching structure) and the problem can then be lead to a one dimensional problem dependent only on the z coordinate. Clearly the assumption of an infinite soil and a plane wave is not realistic but it allows the evaluation of the heating phenomenon in an easily manageable way, and the solution is still valid in the (real) portion of the terrain illuminated by the antenna.

As in the most electromagnetic problems, the characterization of the materials used is essential. In this case, the following electromagnetic properties of the soil are assumed to be known

- $\epsilon(z,T)$ and $\sigma(z,T)$, dielectric constant and conductivity of the soil, assumed to be independent of z (but not of T) for $z > Z_\infty$, being $\epsilon_\infty(T)$ and $\sigma_\infty(T)$
- $\epsilon_{rc}(z,T) = \dfrac{\epsilon(z,T)}{\epsilon_0} - j\dfrac{\sigma(z,T)}{\omega\epsilon_0}$, relative complex dielectric constant
- $\kappa_E(z,T) = \beta_E(z,T) - j\alpha_E(z,T)$, complex propagation constant in the layer

Besides the electromagnetic parameters, the soil needs to be characterize by its thermophysical properties

- $\kappa(z,T)$ and $c(z,T)$, thermal conductivity and specific heat capacity
- h_c, mean convection coefficient on the surface of the soil
- $\rho(z,T)$, density of the soil
- T_0, initial temperature of the soil

Furthermore, the dynamics of the thermal processes is assumed to be slower than that of the electromagnetic field. Assuming a suited temporal discretization for the former, the thermal properties, along with the temperature, can be considered constant in every time step during the evaluation of the electromagnetic field. This allows to evaluate the electromagnetic field at fixed temperature and then the thermal dynamics with the determined field, alternatively.

Let then $T(z)$ be the temperature at a given instant, remembering that in the deepest part of the soil ($z \to \infty$) it assumes the unperturbed value T_0. A normalized

(to the characteristic impedance of the vacuum ζ) local impedance of the medium can be defined as

$$Z(z) = \frac{1}{\zeta}\frac{E(z)}{H(z)} \tag{2.4.1}$$

and deriving

$$\frac{dZ}{dz} = \frac{1}{\zeta H^2}\left(\frac{dE}{dz}H - E\frac{dH}{dz}\right) \tag{2.4.2}$$

Using (2.3.5) and (2.3.7) to calculate the derivatives within the brackets, it follows that

$$\begin{aligned} \frac{dE(z)}{dz} &= -j\omega\mu_0[-H(z)] \\ \frac{d[-H(z)]}{dz} &= -j\omega\epsilon_0\epsilon_{rc}[z,T(z)]E(z) \end{aligned} \tag{2.4.3}$$

and substituting in equation (2.4.2)

$$\begin{aligned} \frac{dZ}{dz} &= j\frac{\omega\mu_0}{\zeta} - j\frac{\omega\epsilon_0}{\zeta}\,\epsilon_{rc}[z,T(z)]\,\frac{E^2}{H^2} = \\ &= j\beta_0 - j\beta_0\epsilon_{rc}[z,T(z)]\,Z^2(z) = j\beta_0\,\left\{1-\epsilon_{rc}\left[z,T(z)\right]\,Z^2(z)\right\} \end{aligned} \tag{2.4.4}$$

The equation (2.4.4) is in the form of a *Riccati equation* and can be solved numerically, given the boundary condition

$$\lim_{x\to\infty} Z(z) = \frac{1}{\sqrt{\epsilon_\infty(T_0)}} \tag{2.4.5}$$

Actually, from a practical point of view, this condition can be imposed at the depth Z_∞, choosing Z_∞ such that

$$\exp\left\{-\int_0^{Z_\infty}\alpha_E[z,T(z)]dz\right\} \ll 1 \tag{2.4.6}$$

The knowledge of the impedance allows to calculate the reflection coefficient Γ at the interface air-soil and, using the incident wave, the fields on the surface $E(0)$ and $H(0)$. These values can now be used to determine the field inside the soil. From the first equation of (2.4.3), substituting the magnetic field as in (2.4.1), the electric field can be estimated as a solution of

$$\frac{dE(z)}{dz} = \frac{j\omega\mu_0}{\zeta}\frac{E(z)}{Z(z)} \tag{2.4.7}$$

which was the missing source in (2.2.26), here reported

$$P(\vec{\mathbf{r}},T)=\frac{1}{2}\,\omega\,\epsilon_{2,\text{eff}}\,(T)\left|\vec{\mathbf{E}}(\vec{\mathbf{r}})\right|^2=\frac{1}{2}\,\sigma_{\text{eff}}(T)\left|\vec{\mathbf{E}}\,(\vec{\mathbf{r}})\right|^2 \tag{2.2.26}$$

necessary to solve the heat transfer equation.

When the volumetric power production is evaluated for a given time, the solution of the thermal aspect of the problem can be carried out. The one-dimensional heat transfer equation, in the form (2.2.16),

$$\rho c\frac{\partial T(z,t)}{\partial t}=k\frac{\partial^2 T(z,t)}{\partial z^2}+P(z) \tag{2.4.8}$$

can be discretized in time and space. Given a spatial step Δz and a time step Δt, let the discretized temperature function be $T_{q,n}=T(q\Delta z,n\Delta t)$ so that the discretized equation becomes

$$\begin{aligned}T_{q,n+1}&=T_{q,n}+\frac{\Delta t}{\rho[q\Delta z,T_{q,n}]c[q\Delta z,T_{q,n}]}\times\cdots\\&\cdots\times\left\{k[q\Delta z,T_{q,n}]\frac{T_{q+1,n}-2T_{q,n}+T_{q-1,n}}{(\Delta z)^2}+P(q\Delta z)\right\}\qquad q>0\end{aligned} \tag{2.4.9}$$

where P(z) is obtained from (2.2.26) considering the temperature distribution at the n-th time step (i.e. $t=n\Delta t$).

The equation (2.4.9) is valid for $1\leqslant q\leqslant Q-1$. Defining $Z_\infty=Q\Delta z$, we have $T_{Q,n}=T_0$ that stands $\forall n$. On the other side, in $z=0$, the boundary condition is obtained matching the heat flux due to conduction to the heat flux due to convection. Using Fourier Law (2.2.1) and (2.2.17) the boundary condition becomes

$$k(0,t)\left[\frac{\partial T(0,t)}{\partial z}\right]=h_c\,(T(0,t)-T_A) \tag{2.4.10}$$

where T_A is the temperature of the air above the soil. Following the same reasoning as before, the previous equation can be discretized as

$$T_{1,n}=T_{0,n}+\frac{h_c\Delta z}{k[0,T_{0,n}]}(T_{0,n}-T_A)=\left(1+\frac{h_c\Delta z}{k[0,T_{0,n}]}\right)T_{0,n}-\frac{h_c\Delta z}{k[0,T_{0,n}]}T_A \tag{2.4.11}$$

and inverted to obtain $T_{0,n}$

$$\begin{aligned}T_{0,n}&=\left(1+\frac{h_c\Delta z}{k[0,T_{0,n}]}\right)^{-1}\left\{T_{1,n}+\frac{h_c\Delta z}{k[0,T_{0,n}]}T_A\right\}\simeq\cdots\\&\cdots\simeq\left(1+\frac{h_c\Delta z}{k[0,T_{1,n}]}\right)^{-1}\left\{T_{1,n}+\frac{h_c\Delta z}{k[0,T_{1,n}]}T_A\right\}\end{aligned} \tag{2.4.12}$$

where the approximation $k[0, T_{0,n}] \simeq k[0, T_{1,n}]$ has been used.

Summarizing the procedure, equation (2.4.4) is solved numerically to obtain the function $Z(z)$. The knowledge of the impedance allows to solve (2.4.7) for the electric field $E(z)$ in the soil, which in turn can be used to evaluate the power density in (2.2.26), such that every term in the heat equation is defined. The analysis of the thermal process can now be carried out. At the time $t = 0$, the system is assumed to be at the temperature T_0, such that $T(z, 0) = T_0$, or in a discrete form $T_{q,0} = T_0$. Using equation (2.4.9) is then possible to determine $T_{q,1}$ for all the $Q - 1$ spatial point for $0 < q < Q$. Then only two points remain to evalueate at time $n = 1$, $T_{0,1}$ and $T_{Q,1}$. The latter is simply defined by the boundary condition $T_{Q,n} = T_0$ which is true for every n (consequence of the choise of Z_∞). The former is find out using the convective boundary condition at $z = 0$, from the (approximated) finite difference equation (2.4.11). The spatial distribution of temperature at the instant $t = \Delta z$ is now fully determined. Using this knowledge the cycle can start again, the volumetric power density can be calculated for $n = 1$, and repeating all the steps, the temperature distribution at $n = 2$ can be determined, and so on for all the time steps.

The time step need to be chosen to avoid instability. If the maximum stable time step is too small, an *implicit method* [32] can be used. In such cases (2.4.9) can be rewritten as

$$\begin{aligned} -T_{q,n-1} = -T_{q,n} + \frac{\Delta t}{\rho[q\Delta z, T_{q,n}]c[q\Delta z, T_{q,n}]} \times \cdots \\ \cdots \times \left\{ k[q\Delta z, T_{q,n}] \frac{T_{q+1,n} - 2T_{q,n} + T_{q-1,n}}{(\Delta z)^2} + P(q\Delta z) \right\} \end{aligned} \tag{2.4.13}$$

valid for $1 < q < Q - 2$, while for $q = Q - 1$ the term $T_{q+1,n}$ is known and equal to T_0. Also, for $q = 0$, equation (2.4.11) is used in the form

$$T_{1,n} = \left(1 + \frac{h_c \Delta z}{k[0, T_{0,n-1}]} \right) T_{0,n} - \frac{h_c \Delta z}{k[0, T_{0,n-1}]} T_A \tag{2.4.14}$$

which leads to a system in Q equations and Q unknowns where without any constraint on Δt.

Fields	Coordinates (WGS84 GD) Longitude	Latitude	Soil Texture (%) Sand	Slit	Clay
A	9.166919204	39.70296945	29	50.1	20.9
E	9.221810497	39.68763253	22.4	50.6	27
F	9.223684117	39.69001663	29.3	45.5	22.2
G	9.217435689	39.73173653	5.9	90.8	3.3
H	9.159000279	39.68831217	17.7	52	30.3

Table 2.4 Physical parameters of different types of terrain

2.5. Simulations and Results

2.5.1. Linear Model

To evaluate the feasibility of the method proposed for the disinfection, and to acquire a better understanding of how the heat distributes without considering second order effects, an initial test has been performed considering the characteristics of the soil as constant with temperature.

The soil used for this test is defined from a thermophysical point of view by a density of $\rho = 1200\,\mathrm{kg\,m^{-3}}$, specific heat $c = 1200\,\mathrm{J\,kg^{-1}\,K^{-1}}$ and thermal conductivity $k = 0.5\,\mathrm{W\,m^{-1}\,K^{-1}}$, while the convection coefficient used is $h_c = 2.0\,\mathrm{W\,m^{-2}\,K^{-1}}$.

The value of soil moisture used for the simulation were acquired from a measurement campaign performed on Sardinia farmland using TDR (time domain reflectometry) and gravimetric measures. Hence, data on the superficial layer of soil were directly exploited. The texture of analyzed soils is reported in Table 2.4 [33, 34]. By the knowledge of these values the dielectric constant can be determined using Hallikainen model.

To obtain an appropriate disinfection of the soil, a critical temperature needs to be reached. Experimental evidence has shown that the treatment efficiency improves for prolonged exposure time. Nevertheless, too high temperatures needs to be avoided because could be harmful for organic nutrients. Since the temperature would increase if a constant microwave power is continuously provided to the soil, than the electromagnetic radiation needs to be accurately controlled. Therefore the critical temperature can be reached using a high power while can be maintained lowering the power or switching on and off the generator.

For the purpose of this test, the critical temperature considered is 60 °C, to be kept for 30 min in the first layer of 2.5 cm. The air and the soil are initially at the temperature of 20 °C. The soil is assumed to be illuminated by an antenna,

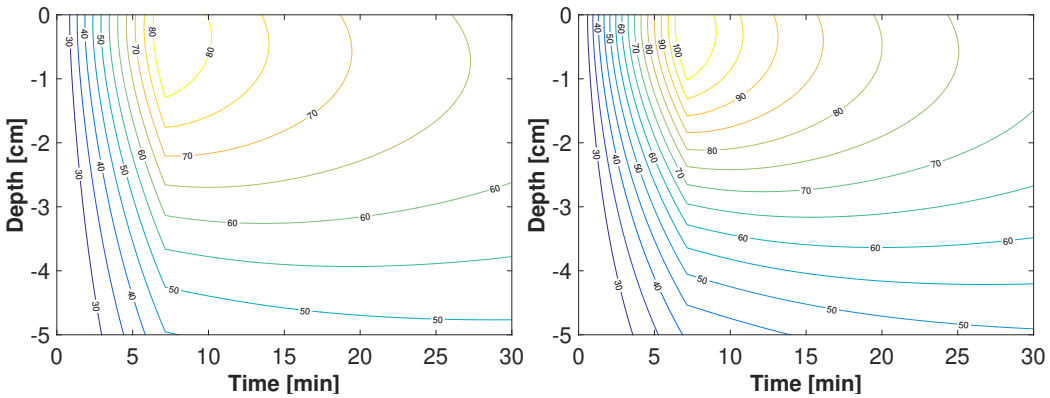

(a) Field A - Soil moisture 20% **(b)** Field A - Soil moisture 40%

Figure 2.1 Linear model results

such as a horn antenna [17, 18], with a gain of 10 dB at the working frequency of $f = 2.4\,\text{GHz}$, placed at a distance of 0.95 m from the soil and directed such that an orthogonal incidence occurs. Under these conditions, an incident Poynting vector (i.e. power density) is obtained over an illuminated area of $A_i = 0.72\,\text{m}^2$. After a few attempts, it can be found that a power of 8 kW (corresponding to a power density of $11\,\text{kW/m}^2$ on the surface of the soil) supplied to the antenna for a time period of 7.2 min allows to achieve the required heating for the required amount of time, as shown in figure 2.1a, which are referred to the characteristics of field A in table 2.4. The figure also shows that the soil heating is a process significantly faster than heat transmission, which is the reason why the soil keeps an almost constant temperature profile for a long time after a short heating time.

The water content is a critical parameter in soil disinfection, in fact the higher the amount of water, the better the heating. Unfortunately a too fast heating can easily lead to an overheating on the terrain close to the surface, as shown in figure 2.1b, which is dangerous for organic nutrients. It means that a previous knowledge of the soil moisture is required for a good planning of the disinfection. On the other hand, for a very dry soil, were the heating would be harder to obtain, the addition of a controlled amount of water to the soil (i.e. irrigation) can be very useful before the treatment to achieve the desired heating.

2.5.2. Nonlinear model

The linear model is useful for a preliminary analysis of the problem but it is based on the assumption that all the parameters describing the soil are constant with temperature (and position), which is a rough approximation, so as a further

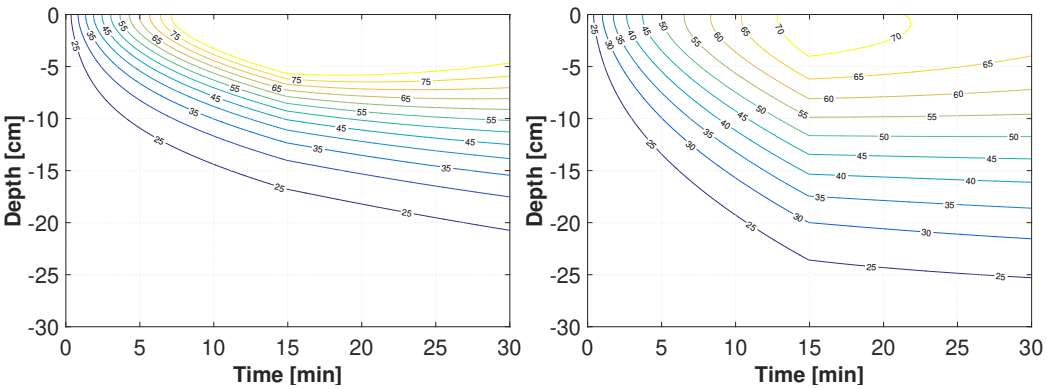

(a) Field A – $m_v = 20\%$ – Linear model **(b)** Field A – $m_v = 20\%$ – Nonlinear model

Figure 2.2 Comparison of linear and non linear model in the same situation

step to improve the model, temperature dependency is now introduced and different profile of soil moisture are used.

First of all, it could be interesting to compare the linear and nonlinear model in the same situation. For the comparison, let the aim of the disinfection be to get rid of the fungus *F. oxysporum*, whose fractional survivor expression in function of time and temperature is presented in [35]. If the survival fraction desired after the treatment is 1×10^{-9}, it can be reached after 55 min at 70 °C, 6.5 min at 75 °C or 1.3 min at 80 °C. Using as a reference the central value of temperature and assuming, as in the previous section, an incident power density of 11 kW/ m^2, the prediction of the linear model is that 13 min of irradiation are necessary to obtain a temperature of (at least) 75 °C in the first 5 cm of depth as shown in 2.2a. Instead using the nonlinear model, i.e. thermal parameters dependent on temperature, all other things being equal, the temperature of 75 °C isn't even reached and the temperature of 70 °C is kept for 6.5 min only in a layer of 1.7 cm as can be seen in figure 2.2b. Moreover, the two figures show that the nonlinear model predict a lower temperature on the surface of the soil, in fact, after about 6 min the temperature is already 75 °C on the linear model, while 70 °C are reached only after 13 min using the nonlinear model. This is mainly due to the lowering of the electric conductivity as the temperature increases. Indeed a lower conductivity leads into a deeper penetration of the electromagnetic field which in turn leads to a more uniform distribution of the energy given to the soil, that is the reason why the surface temperature isn't able to raise up as fast and as high as in the linear model (less energy is absorbed by the superficial layer).

The results presented up to now are all referred to a soil characterized by a

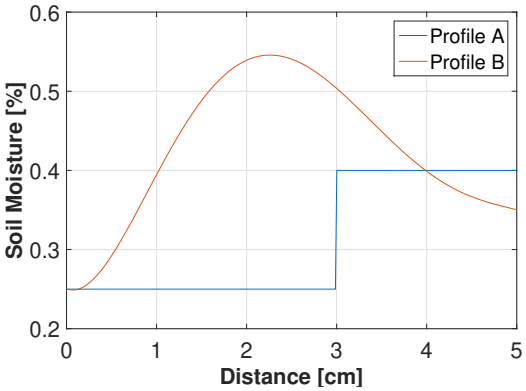

(a) Different profiles of m_v

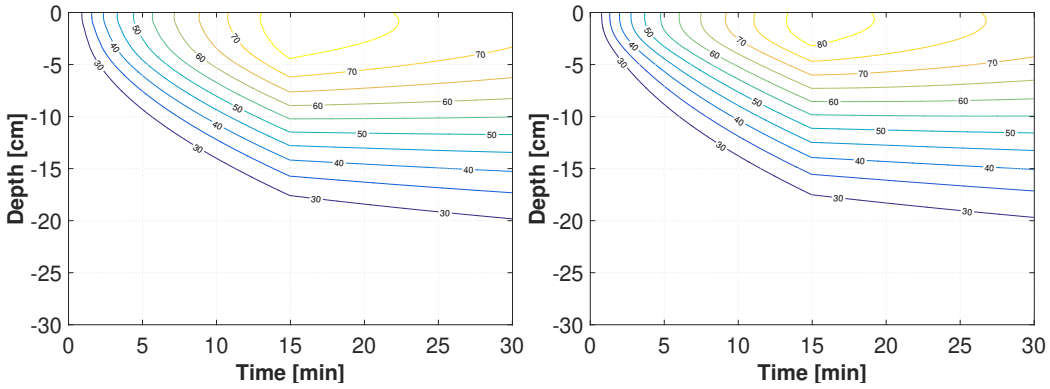

(b) Field A – m_v Profile A

(c) Field A – m_v Profile B

Figure 2.3 Comparison of nonlinear model for different moisture profiles

constant value of m_v, but in a real situation the humidity can be variable with depth, especially if an irrigation has been done to supply the soil with an amount of water suitable for the treatment. In these cases, the humidity profile needs to be taken into account in the model. In the figure 2.3a, two different profiles are reported, where the variation of humidity occurs in the first 3 cm of the soil. Beyond this depth, the last value is kept for every z. As can be seen in the figures 2.3b and 2.3c, profile B leads to higher superficial temperature because of its higher humidity close to the surface, while in deep, the differences between the two cases are very small. The comparison of the two graphs confirms what previously stated, that an appropriate irrigation can be exploited to obtain the desired temperature profile in the upper layer which is the layer of interest.

It is worth investigating the response of the model to different terrain. For this purpose an analysis has been carried out to see the temperature profile in the soil A, G and H, while using the moisture distribution B. In figure 2.4 the temperature profiles of the terrains have been plotted on the same axis. It is clear that every

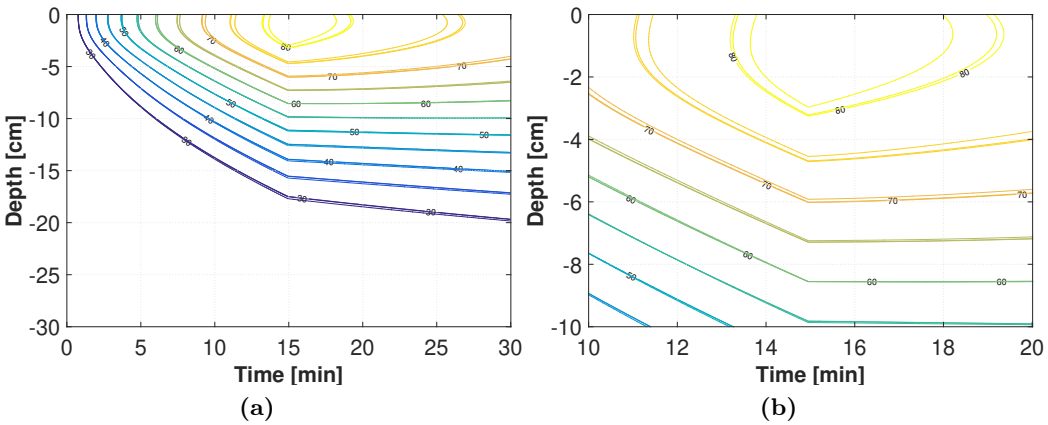

Figure 2.4 Comparison of nonlinear model for different moisture profiles

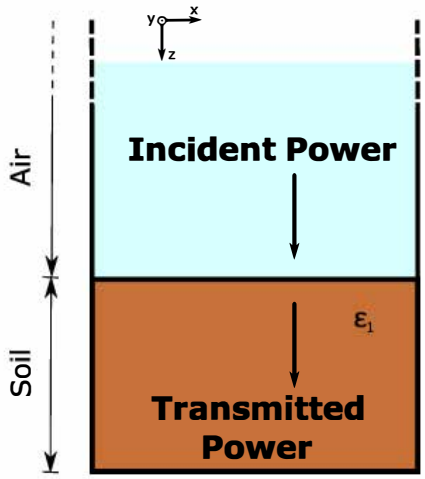

Figure 2.5 Geometry for the linear and nonlinear model

distribution is very close to each other, being different at the highest temperature (but only for the field labeled as H). The very similar behavior of the soils suggests that their thermal parameters have little variation with the composition and with temperature. This is in agreement with the (implicit) assumption done when the equation (2.2.16) has been used, in place of (2.2.15), where k is factored out of the divergence operator for the assumption of little variation respect of the position.

2.5.3. Modified Nonlinear Model for Raised Beds

The previous model has been developed using the geometry pictured in figure 2.5, which describes cultivations on farmland. However, in all the situations where

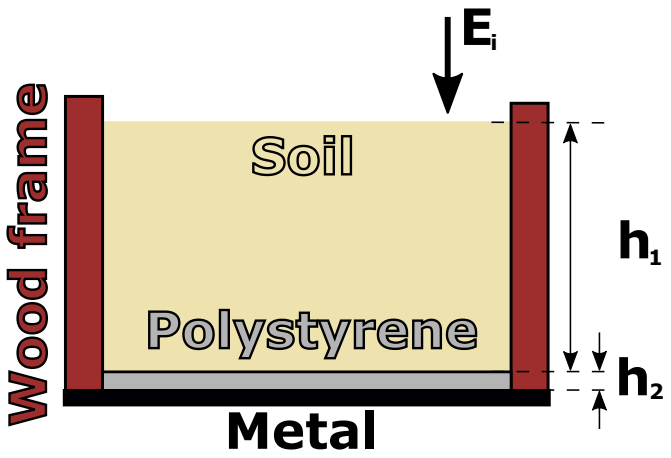

Figure 2.6 Geometry for the raised bed

a controlled environment is required, often the choice goes to the cultivation on greenhouses. In fact, despite its high costs, it presents a number of advantages such as the control of air parameters (temperature, humidity, speed, CO_2) and soil (temperature, pH, electrical conductivity, moisture, nutrients and even radiation to which is subjected) in addition to foster the growth of plants and protect them from elements. With the purpose to create the best environment possible for a specific cultivation, greenhouses are often equipped with structures such as raised beds. As shown in figure 2.6, they are essentially a framework with walls typically made of wood and the bottom made of wood or metal metal, that can be filled with the desired soil. In some cases it is desirable to have a thermal insulation layer on the bottom of the box, that can be made of polymers such as polystirene.

It is clear that these different materials change the problem to be solved. In particular the presence of the polystirene and the metallic object on the bottom causes the boundary condition of the electromagnetic problem to be changed. Specifically, the electromagnetic field now propagates along a layer of polystirene of thickness d, and reaches the metal which, as a first approximation (i.e perfect electric conductor), imposes the tangential electromagnetic field, which is the only component of the field, to be null. Moreover, from a thermal point of view, the presence of the insulation layer causes the thermal boundary condition to change as well.

Since the geometry of the problem isn't changed, a planar incidence is still in act on layers orthogonal to its direction of propagation. This allows to easily adapt the model to the raised beds. Technically, to take into account the presence of the polystirene put on the metal, it is sufficient to modify the impedance in (2.4.5) with the impedance of a transmission line closed on a short circuit [36]. If we call β_p and Z_p the secondary constant of the line related to the polystirene layer, then the new

Field	Soil Texture (%) Sand	Slit	Clay	ρ_b $\mathrm{kg\,m^{-3}}$	Soil Parameters c[@20 °C] $\mathrm{J\,kg^{-1}\,K^{-1}}$	k[@20 °C] W/m/K	h_c[@20 °C] $\mathrm{W\,m^{-2}\,K^{-1}}$
A	29	50.1	20.9	1400	893	2.47	2.0
B	95	1.5	3.5	1320	1069.4	5.18	2.0

Table 2.5 Physical parameters of different types of terrain

boundary condition becomes

$$Z(H) = \frac{1}{\zeta}\Big[jZ_p \cdot \tan(\beta_p h_2)\Big] \tag{2.5.1}$$

where, the term inside the brackets is the input impedance of the polystirene posed on the metallic bottom.

The thermal problem also require a modification, in particular, the previous condition $T(Z_\infty, t) = 20\,^\circ\mathrm{C}$, needs to be changed with a null heat flux condition, namely

$$\left.\frac{\partial T(z,t)}{\partial z}\right|_{z=H} = 0 \tag{2.5.2}$$

The adjusted model is then used to compare two different soils (Table 2.5), one of each with its own moisture profile shown in figure 2.7a. This time the disinfection aims to the elimination of the fungi *S. rolsfii*, which requires to maintain a temperature of 70 °C for about 7 min, or 80 °C for 4 min, to obtain a survival fraction of 1×10^{-8}. It can be seen from figures 2.7b and 2.7c, how the soil B requires a long irradiation time to reach the required temperature for disinfection, due mainly to the very low moisture of 10% for almost all the soil depth, but when the temperature is reached on the surface, it goes down faster respect to what happens for soil A. In fact, field B requires about $25\,\mathrm{kW\,m^{-2}}$ for 30 min for the disinfection, or 11 kW for almost 40 min. For a faster heating of this soil, irrigation is strongly recommended.

Also a comparison between farmland and raised beds can be interesting. As the figure 2.7b and figure 2.3c show, in a raised bed the temperature is reached faster than in farmland. This effect can be attributed to the different reflection the wave is subjected to at the bottom of the box causing a different distribution of the field in the soil.

Finally, $Z(0)$, i.e. the input impedance of the soil, can be compared between the two cases of figure 2.7. It can be seen in figure 2.8 that in case A, the input

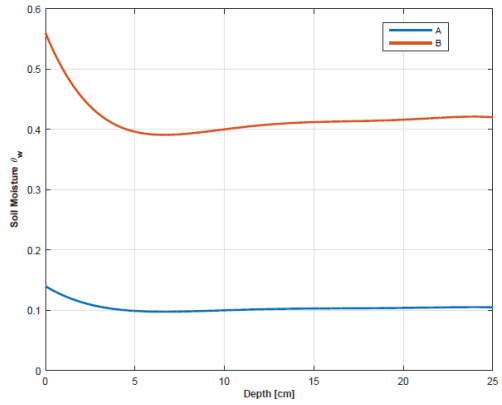

(a) Different profiles of m_v

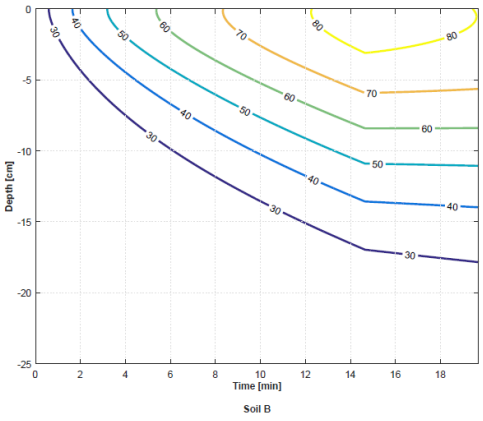

(b) Field A with moisture profile A

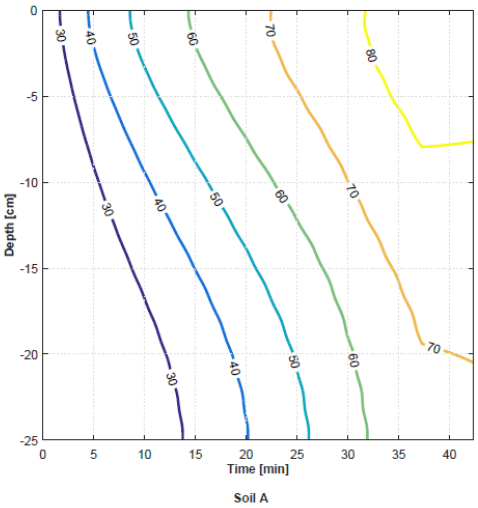

(c) Field B with moisture profile B ($S_i = 25\,\mathrm{kW/m^2}$)

Figure 2.7 Temperature profile of high moisture soil (A) versus dry soil (B)

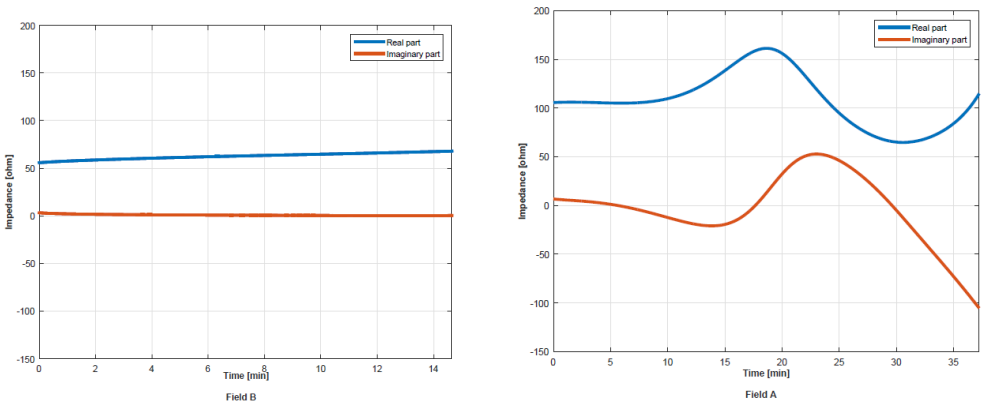

(a) (b)

Figure 2.8

impedance over time is quite constant and keeps low values both in the real and imaginary part, while for the case B the impedance strongly varies with time, basically due to the temperature increase in the whole bulk (while for case A, high temperature are reached only close to the surface). Besides, case B presents high values of impedance, while the time varying behavior leads to a variation over time of the absorbed power, making difficult the design of the optimal setup for the treatment. Again, it suggest that the irrigation of the soil is required.

2.5.4. Robustness and Convergence Test

From the discussion carried out up to now, it results that while solving the problem of the electromagnetic heating of the soil, the temperature is strongly influenced by the dielectric constant which, in turn, it has a strong dependency on the moisture. On the countrary, the thermal parameters present just a slightly dependency on temperature, so even an overheat of the soil doesn't lead to a change in the thermal processes of the system (how the heat flows in the soil).

It is then mandatory an analysis of the robustness of the model to a variation of the humidity. To evaluate this effect, the case A in the previous section has been repeated using humidity distribution equals to 90% and 110% of the initially value used. As figure 2.9a shows, there is no substantial variation to temperature profiles between the three situation. Even the surface temperature reported in figure 2.9b supports this statement, showing that the critical temperature is reached in each case in an interval of 40 s.

Besides the robustness of the algorithm, some convergence tests has been carried

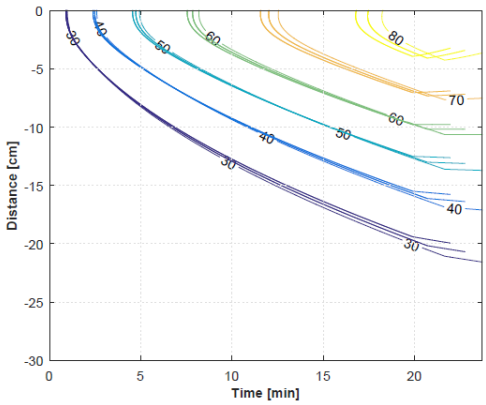

(a)

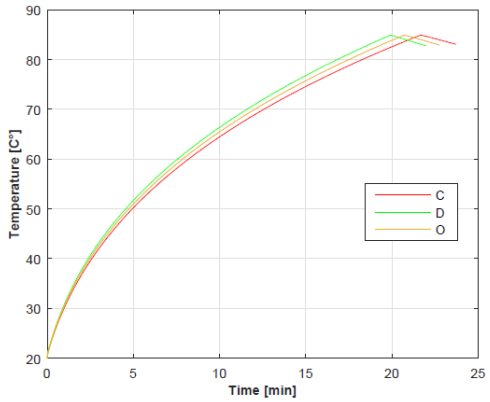

(b)

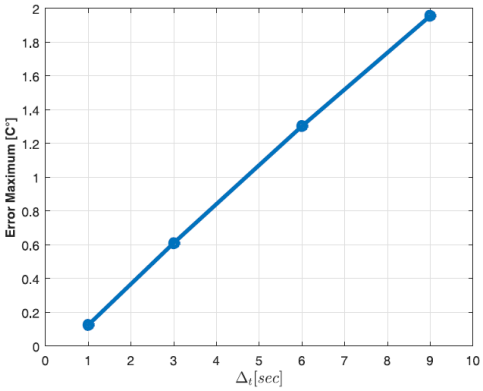

(a)

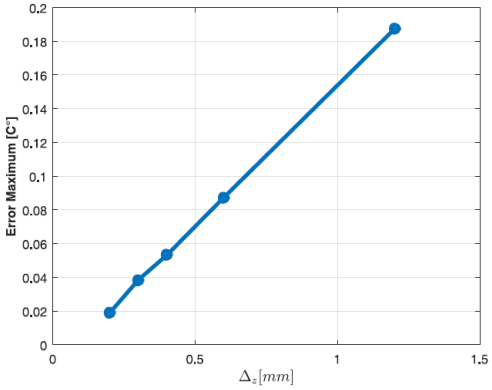

(b)

out, to evaluate the best Δt and Δz. It is worth noting that the convergence of Δt and Δz can be examined in an independent way thanks to the use of an implicit scheme described in section 2.4. To evaluate the best Δt, first the distribution is calculated using a small time step $\Delta t = 0.5$. The resulting temperature profile is assumed as *exact*. Then, different Δt are used to evaluate the temperature, assuming the same $\Delta z = 0.15$ for every run. The maximum temperature error between the runs and the correct one is reported in 2.9a where it can be seen that for a time step of 3 s to 5 s a smaller error of 1 °C is obtained, a value well inside the need of the application.

In the same way, the spatial step is evaluated using as reference value$\Delta z = 0.15$. All the simulation has been carried out using $\Delta t = 1$ s. Figure 2.9b shows that errors due to large Δz are very small. However a too large Δz could affect the results of the electromagnetic part of the solution, so that $\Delta z = 0.12$ mm has been

used, together with $\Delta t = 0.5\,\mathrm{s}$ for the simulations.

3. Resonant Cavity as a Bioreactor

Electromagnetic fields exert forces over all charged particles and therefore can be a factor [1] for the development of chemical and biochemical reactions. As a matter of fact, such reactions involve interaction between the charged part of the molecules involved and such interaction can be modified by an external electromagnetic field. And the highest field level, the strongest the effect. In the last decades, a huge member of researches on such effects has been completed, pushed by the widespread use of electromagnetic sources close and very close to the population (cellular phones, wireless local area network, and so on). As a consequence, many results have been found on the electromagnetic effects on the biochemical reactions in the human body [2]. However, the most significant effect is due to the increase of temperature, which has a strong effect on the kinetic of the biochemical reactions. Therefore, the same increase can be obtained in industrial biochemical reaction using eletromagnetic field as heating source [3].

Actually, electromagnetic heating is more effective [4–6] and faster than traditional heating since the heat is produced directly into the reactive solution [7]. Furthermore, reaction enhancement due to electromagnetic heating is stronger than the traditional one (at the same temperature). This can be due to both thermal and nonthermal effects [8–11]. Among the former, electromagnetic field can selectively heat the reagents or lead to hot spots and local overheating [12]. The latter would derive from the electromagnetic interaction mechanism. The electromagnetic field

acts directly on the molecules modifying their internal dipoles, which are usually responsible for the interaction. Therefore, it has a direct and specific effect on some specific molecules in the reaction medium, leading to apparent variations in the kinetic frequency factor and in the activation energy [13]. However, no widely accepted reason to explain why microwave radiation sometimes enhances chemical and biochemical processes have been reached, despite the significant research activity on this point. This is one of the reasons which have prevented a full exploitation of the electromagnetic technology at microwave frequencies in biochemistry. But an equally strong reason is the need for a precise temperature control.

In effect, the interactions between radio frequency electromagnetic fields and kinetics, particularly in the case of biochemical reactions, probably have not yet been properly investigated. Most of the studies in the scientific literature about this topic reveal the absence of a precise temperature prediction and control in microwave-irradiated reactors. But kinetic mechanisms in biochemical reactions are often complex, with many steps and different possible routes, on which the effect of temperature and of the EM field exposition can be not the same. As a consequence of the latter, just a single reaction step can be conditioned by the induced orientation of dipolar reactants and of enzyme active sites, leading to a (better or worse) modification in the coordination between the reactive couple (e.g., the substrate molecule and the enzyme active site or an inhibitor and the active site) [14]. Only a detailed temperature distribution knowledge, together with the availability of precise experimental kinetic data, could support an effective study on these phenomena. Moreover, enzymes (which act as catalysts in biochemical reactions) are complex and fragile protein molecules with an activity strictly dependent on temperature. In particular, their catalytic ability strongly increases with temperature, but over a certain critical temperature, their activity quickly and irreversibly falls, due to the protein structure denaturizing. Therefore, small differences in the local experimental conditions (e.g., a local overheating, not detectable by the normally used temperature measure devices) can bring to very different experimental results, apparently without explanation. To give some literature cases about enzyme kinetics, positive effects on the yields of isomerase [15] and amylase [16] catalyzed reactions, and on the lipase catalyzed transesterification (for biodiesel production) [17, 18], have been noted by the authors, probably not due only to a thermal (heating) effect, but it is impossible to exactly know the local experimental conditions and so the real explanation of the registered effect.

A controlled electromagnetic environment is very useful to evaluate the enhancement in microwave irradiate reactions. But in addition to an environment is manda-

tory to study nonthermal effects of electromagnetic fields. As a matter of fact, nonthermal and thermal effects operate concurrently, and so the former are hard to detect (or even to show their existence).

But the largest part of the researches on microwave-enhanced biochemical reactions has been conducted at a power level high enough to increase significantly the reaction temperature. In many other cases, the exposition conditions have not been monitored. As a result in a detailed way (both from the chemical and fluid dynamic point of view and from the electromagnetic one), only the net effect of electromagnetic field has been recorded, but no detailed information has been obtained.

Therefore, an experimental apparatus which is able to irradiate biochemical reactions in a controlled way seems still lacking. A resonant cavity is a good instrument to study the effect of a uniform electromagnetic field incident on the sample, and with particular symmetric geometries it is possible to irradiate more samples in the same time. Such cavities allow to easily obtain different mode distribution with the required rotational symmetry. But for a proper design of the cavity, it would be required to take into account also the behavior of the reagents. However, this has not been done in the literature so far. It will be shown that such a cavity allows a controlled exposition of biochemical reactions to electromagnetic fields and allows also an intrinsic feedback control of temperature, at least for reactions in aqueous solutions.

The aim of this work is to design and analyze the electromagnetic behavior of a microwave-fed resonant cavity. After the design and assessment operations, the working cavity will be simulated in order to foresee the effect of the EM field exposition on the multitube reactor positioned inside, with respect to both the internal temperature distribution and the reaction yield of the enzymatic homogeneous hydrolysis of sucrose (as a simulation case study) in an aqueous (polar) medium, for which detailed physical, chemical, and kinetic parameters are known. This is a preparatory phase to real cavity realization and operation in order to experimentally evaluate the effect of the electromagnetic exposition on organic biological material to be processed (like Carta and Desogus did [8]).

Such results are a first step toward a more ambitious objective, i.e., to find a relationship between kinetic parameters (Arrhenius frequency factor and activation energy) of a microwave-irradiated reaction and the characteristics of the microwave field employed.

3.1. Resonant Cavities

Resonant cavities are structures in which an electromagnetic field is confined. Usually they are realized as hollow metallic objects, empty or filled with dielectric, or as in the case of *dielectric resonators*, using a piece of a high permittivity dielectric.

A field that can exist in a cavity is called a *mode* and is related in some way to the corresponding waveguide mode. It propagates between the end walls of the cavity, so that a stationary pattern arises. Besides, the metallic wall imposes the field to be null on it, so that only particular wavelengths (or frequencies) can exist in the structure. This behavior makes resonant cavities suitable for frequency-selective applications such as filters and oscillators. Moreover, since the field of a mode is derived by functions of propagating waves, the field distribution of every mode presents its own symmetry, which can be exploited in all the applications where the same amount of electromagnetic energy have to be given to different samples.

3.1.1. Theory of Waveguides

A resonant cavity can be seen as a waveguide closed to the extremities by a metal cover that act as a short circuit, so the starting point to study a resonant cavity is to study the waveguide from which it originates.

The study of a waveguide [19] starts with Maxwell equations (in the frequency domain). Assuming a solution in the form

$$\vec{\mathbf{E}}(x,y,z) = \left[\vec{\mathbf{e}}(x,y) + e_z(x,y)\vec{\mathbf{i}_z}\right] e^{-j\beta z} \tag{3.1.1a}$$

$$\vec{\mathbf{H}}(x,y,z) = \left[\vec{\mathbf{h}}(x,y) + h_z(x,y)\vec{\mathbf{i}_z}\right] e^{-j\beta z} \tag{3.1.1b}$$

the components of the curls, keeping into account the z-dependence $e^{-j\beta z}$, can be written in cartesian coordinates, as

$$\frac{\partial E_z}{\partial y} + j\beta E_y = -j\omega\mu H_x \qquad \frac{\partial H_z}{\partial y} + j\beta H_y = j\omega\epsilon E_x \tag{3.1.2a}$$

$$-j\beta E_x - \frac{\partial E_z}{\partial x} = -j\omega\mu H_y \qquad -j\beta H_x - \frac{\partial H_z}{\partial x} = j\omega\epsilon E_y \tag{3.1.2b}$$

$$\frac{\partial E_y}{\partial x} - \frac{\partial E_x}{\partial y} = -j\omega\mu H_z \qquad \frac{\partial H_y}{\partial x} - \frac{\partial H_x}{\partial y} = j\omega\epsilon E_z \tag{3.1.2c}$$

from which the transverse components of the fields can be expressed in function of

the longitudinal ones

$$H_x = \frac{j}{k_c^2}\left(\omega\epsilon\frac{\partial E_z}{\partial y} - \beta\frac{\partial H_z}{\partial x}\right) \qquad H_y = \frac{-j}{k_c^2}\left(\omega\epsilon\frac{\partial E_z}{\partial x} + \beta\frac{\partial H_z}{\partial y}\right) \tag{3.1.3a}$$

$$E_x = \frac{-j}{k_c^2}\left(\beta\frac{\partial E_z}{\partial x} + \omega\mu\frac{\partial H_z}{\partial y}\right) \qquad E_y = \frac{j}{k_c^2}\left(-\beta\frac{\partial E_z}{\partial y} + \omega\mu\frac{\partial H_z}{\partial x}\right) \tag{3.1.3b}$$

where the *cut-off* wavenumber $k_c^2 = k^2 - \beta^2$ has been introduced, while $k = \omega\sqrt{\mu\epsilon}$ is the wavenumber that in presence of dielectric loss can be considered as complex.

The solutions of the problem can be classified depending on the z-components of the field. If $E_z = H_z = 0$, both electric and magnetic field are transverse to the direction of propagation and these solutions are referred as **T**ransverse **E**lectro **M**agnetic (**TEM**) modes. It can be shown that TEM modes can exist only in presence of two or more conductors, which is not the case of a waveguide where only the conductor delimiting the field exists. Other solutions in addition to TEM modes are possible, where only one of the fields, $\vec{\mathbf{E}}$ or $\vec{\mathbf{H}}$, have the longitudinal component. If the electric field is transverse to the direction of propagation (i.e. $E_z = 0, H_z \neq 0$) the solution is called **T**ransverse **E**lectric mode, instead if the magnetic field is the one to be transverse, the solution is called **T**ransverse **M**agnetic mode.

In both cases (TE and TM modes), the general solution is obtained finding the expression of the only one tangential component existing, that satisfies the Helmholtz equation. For example, in a TE problem the Helmholtz equation needs to be solved for H_z,

$$\nabla^2 H_z + k^2 H_z = 0 \tag{3.1.4}$$

and looking for solutions in the form $H_z(x, y, z) = h_z(x, y)e^{-j\beta z}$, (3.1.4) becomes

$$\left(\frac{\partial}{\partial x^2} + \frac{\partial}{\partial y^2} + k_c^2\right) h_z(x, y) = 0 \tag{3.1.5}$$

This equation is solved again using separation of variables such that $h_z(x, y) = X(x)Y(y)$, which leads to solutions of the type

$$h_z(x, y) = (A\cos k_x x + B\sin k_x x)\ (C\cos k_y y + D\sin k_y y) \tag{3.1.6}$$

where the constants k_x and k_y satisfy $k_c^2 = k_x^2 + k_y^2$.

The analysis proceeds imposing the boundary conditions. Considering the geometry of a rectangular waveguide, as shown in figure 3.1, on the walls the tangential

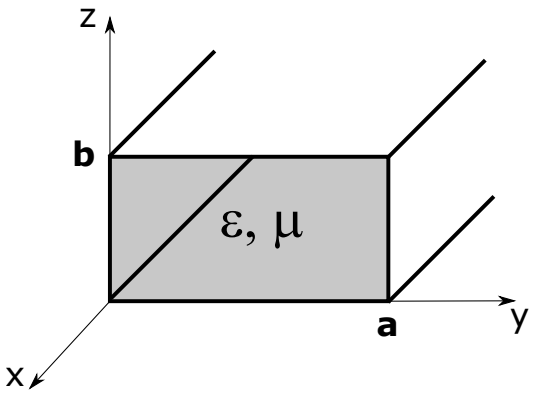

Figure 3.1 Rectangular waveguide geometry

component of the electric field have to be null such that

$$\begin{aligned} e_x(x,y) &= 0 \qquad \text{at } y = 0, b \\ e_y(x,y) &= 0 \qquad \text{at } x = 0, b \end{aligned} \tag{3.1.7}$$

Using equations (3.1.3), in the particular case of TE modes ($E_z = 0$), the electric field can be determined, and using (3.1.7), it can be found that $B = D = 0$ and

$$k_x = \frac{m\pi}{a} \qquad m = 0, 1, 2, \ldots \tag{3.1.8}$$

$$k_y = \frac{n\pi}{b} \qquad n = 0, 1, 2, \ldots \tag{3.1.9}$$

and finally the electric and magnetic fields becomes

$$H_z = A_{mn} \cos\frac{m\pi x}{a} \cos\frac{n\pi y}{b} e^{-j\beta z} \tag{3.1.10a}$$

$$E_x = \frac{j\omega\mu n\pi}{k_c^2 b} A_{mn} \cos\frac{m\pi x}{a} \sin\frac{n\pi y}{b} e^{-j\beta z} \tag{3.1.10b}$$

$$E_y = \frac{-j\omega\mu m\pi}{k_c^2 a} A_{mn} \sin\frac{m\pi x}{a} \cos\frac{n\pi y}{b} e^{-j\beta z} \tag{3.1.10c}$$

$$H_x = \frac{j\beta m\pi}{k_c^2 a} A_{mn} \sin\frac{m\pi x}{a} \cos\frac{n\pi y}{b} e^{-j\beta z} \tag{3.1.10d}$$

$$H_y = \frac{j\beta n\pi}{k_c^2 b} A_{mn} \cos\frac{m\pi x}{a} \sin\frac{n\pi y}{b} e^{-j\beta z} \tag{3.1.10e}$$

The propagation constant β requires further attention. In fact, it is

$$\beta = \sqrt{k^2 - k_c^2} = \sqrt{k^2 - \left(\frac{m\pi}{a}\right)^2 + \left(\frac{n\pi}{b}\right)^2} \tag{3.1.11}$$

which is real only if $k > k_c$. If this condition is not verified, β becomes imaginary and

the term $e^{-j\beta z}$ becomes an attenuation term such that the mode cannot propagate away from its source of excitation. A cut-off frequency can be determined for every mode

$$f_{c_{mn}} = \frac{k_c}{2\pi\sqrt{\epsilon\mu}} = \frac{1}{2\pi\sqrt{\epsilon\mu}}\sqrt{\left(\frac{m\pi}{a}\right)^2 + \left(\frac{n\pi}{b}\right)^2} \tag{3.1.12}$$

which represent the frequency over which the mode can propagate. If the operating frequency is under the cut-off frequency, the mode is called *cutoff* mode or *evanescent* mode. The mode with the lowest cut-off frequency is known as *dominant* mode.

The study of TM modes follows the same procedure used for TE modes. The Helmholtz equation is solved for E_z, which has the same general solution as in (3.1.6). The boundary conditions can be applied directly to $e_z(x, y)$, which leads to the satisfaction of the boundary condition also to $e_x(x, y)$ and $e_y(x, y)$. Table 3.1 summarizes the results for TM modes. A close examination of the field expressions tells that electromagnetic field is identically null for $m = 0$ or $n = 0$, so that the first TM mode is TM_{11}.

Of course, the procedure to calculate the modes of a waveguide is general and can be applied to different structures, keeping into account the geometry. For example, for a cylindrical waveguide, Helmholtz equation can be solved in cylindrical coordinates, which, using separation of variables, leads to a Bessel's differential equation for the ρ-dependent function, which has the form of a Bessel funcion of first kind $J_n(k_c\rho)$, and to an ordinary differential equation for the ϕ-dependent one. The boundary condition is then applied to E_z when solving for TM solutions, which are satisfied when the Bessel function nullifies. Identifying with n the order of the Bessel function, with m the m-th zero of the same function and with p_{nm} the root corresponding to the m-th zero of $J_n(x)$, the cut-off wavenumber of the mode is determined by imposing the boundary condition. In Table 3.1 the expression of the fields among the others, are reported for the cylindrical waeguide.

3.1.2. Cylindrical Resonant Cavitiy

Resonant cavities can be analyzed using the results of the corresponding waveguide. Let be d the length of a section of a waveguide, closed to its borders by an electric conductor. Inside the waveguide, a propagating wave toward the positive direction z exist. On the closed extremity it is subjected to a reflection originating a wave propagating in the opposite direction. From Table 3.1 and considering the forward and backward traveling waves, the tangential field (E_ρ, E_ϕ) of a cylindrical

Quantity	TM_{mn} Rectangular Waveguide	TM_{nm} Cylindrical Waveguide
k	$\omega\sqrt{\epsilon\mu}$	$\omega\sqrt{\epsilon\mu}$
k_c	$\sqrt{\left(\frac{m\pi}{a}\right)^2+\left(\frac{n\pi}{b}\right)^2}$	$\frac{p_{nm}}{a}$
β	$\sqrt{k^2-k_{c_{mn}}^2}$	$\sqrt{k^2-k_{c_{nm}}^2}$
f_c	$\frac{1}{2\pi\sqrt{\epsilon\mu}}\sqrt{\left(\frac{m\pi}{a}\right)^2+\left(\frac{n\pi}{b}\right)^2}$	$\frac{p_{nm}}{2\pi a\sqrt{\epsilon\mu}}$
E_z	$B_{mn}\sin\frac{m\pi x}{a}\sin\frac{n\pi y}{b}e^{-j\beta_{mn}z}$	$(A\sin n\phi+B\cos n\phi)J_n(k_c\rho)e^{-j\beta_{nm}z}$
H_z	0	0
$E_x\|E_\rho$	$\frac{-j\beta_{mn}m\pi}{k_c^2a}B_{mn}\cos\frac{m\pi x}{a}\sin\frac{n\pi y}{b}e^{-j\beta_{mn}z}$	$\frac{-j\beta_{nm}}{k_c}(A\sin n\phi+B\cos n\phi)J_n'(k_c\rho)e^{-j\beta_{nm}z}$
$E_y\|E_\phi$	$\frac{-j\beta_{mn}n\pi}{k_c^2b}B_{mn}\sin\frac{m\pi x}{a}\cos\frac{n\pi y}{b}e^{-j\beta_{mn}z}$	$\frac{-j\beta_{nm}n}{k_c^2\rho}(A\cos n\phi-B\sin n\phi)J_n(k_c\rho)e^{-j\beta_{nm}z}$
$H_x\|H_\rho$	$\frac{j\omega\epsilon n\pi}{k_c^2b}B_{mn}\sin\frac{m\pi x}{a}\cos\frac{n\pi y}{b}e^{-j\beta_{mn}z}$	$\frac{j\omega\epsilon n}{k_c^2\rho}(A\cos n\phi-B\sin n\phi)J_n(k_c\rho)e^{-j\beta_{nm}z}$
$H_y\|H_\phi$	$\frac{-j\omega\epsilon m\pi}{k_c^2a}B_{mn}\cos\frac{m\pi x}{a}\sin\frac{n\pi y}{b}e^{-j\beta_{mn}z}$	$\frac{-j\omega\epsilon}{k_c^2}(A\sin n\phi+B\cos n\phi)J_n'(k_c\rho)e^{-j\beta_{nm}z}$

Table 3.1 Main parameters for TM_{mn} modes

waveguide, can then be expressed as

$$\vec{\mathbf{E}}_t(\rho,\phi,z) = \vec{\mathbf{e}}_t(\rho,\phi)\left(A^+e^{-j\beta_{mn}z} + A^-e^{j\beta_{mn}z}\right) \tag{3.1.13}$$

for both TE_{nm} and TM_{nm} modes, where A^+ and A^- are arbitrary constant of the corresponding wave. For the tangential field to be null on the closed extremities, must be $A^+ = -A^-$ and the additional following condition needs to be satisfied

$$\beta_{mn}d = l\pi \qquad l = 0,1,2,\ldots. \tag{3.1.14}$$

$$d = \frac{l}{2}\frac{2\pi}{\beta_{mn}} = \frac{l}{2}\lambda_g \tag{3.1.15}$$

λ_g being the in-guide wavelength. Equation 3.1.14 states that only cavities long an integer number of half wavelength allows the existence of the corresponding mode. From the propagation constant (for TM_{nm} modes only)

$$\beta_{mn} = \sqrt{k^2 - \left(\frac{p_{nm}}{a}\right)^2} \tag{3.1.16}$$

it is possible to define the resonant frequency [20] of a mode as

$$f_{nml} = \frac{1}{2\pi\sqrt{\epsilon\mu}}\sqrt{\left(\frac{l\pi}{d}\right)^2 + \left(\frac{p_{nm}}{a}\right)^2} \tag{3.1.17}$$

which can be used to determine the dimensions of the cavity by the knowledge of the working frequency.

Differently to a waveguide, a resonant cavity doesn't shows any cut-off frequency, so that a mode can exist only at its own resonant frequency and not for greater frequencies.

3.2. Cavity Design

In this work, the studied resonant cavity is intended to be used as a controlled environment where a chemical reaction occurs. The cavity is then partially filled with materials in which the reaction takes place. In principle, the presence of a non homogeneous material inside the cavity makes the results obtained in the previous sections not suitable for the analysis. Nevertheless, if the material content is limited, it is licit to assume that a small variation of the fields occurs and even if the perturbed field cannot be approximated with the field of an empty cavity (expecially close to the water as will be shown in a while), the results in the previous

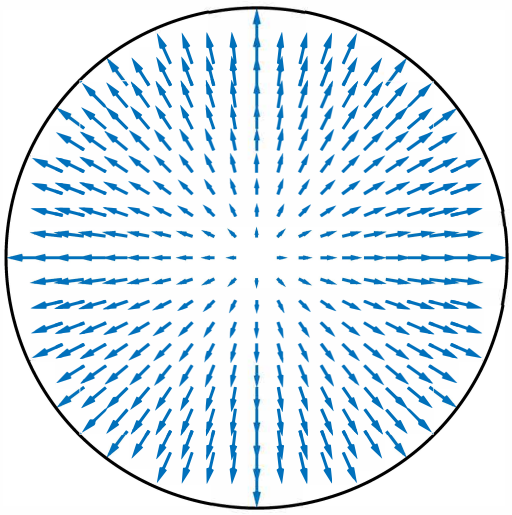

Figure 3.2 Electric field in a cross section of a circular waveguide

sections can still be used as a starting point for the design.

The chemical reactions under test are enzymatic reactions. Enzymes are biological catalysts, that is, they are able to speed up a particular reaction. Chemical reactions happen at a characteristic reaction rate at a given temperature and chemical concentration. Typically, reaction rates increase with increasing temperature because there is more thermal energy available to reach the activation energy necessary for breaking bonds between atoms. On the other hand, enzymes are very sensible to temperature and can get inactivate if in an overheated environment. The reactions considered in this work occurs in an aqueous medium, which means that, if the system is subjected to electromagnetic waves, it is easily heated and for this reason the power used to feed the cavity have to be controlled.

The water solution flows into a pipe that goes through the cavity, along its length. As stated before, the transversal section of the pipe needs to be small enough to preserve the theoretical behavior of the cylindrical cavity. As a benefit to this choice, a uniform irradiation of the solution is achieved since the small radius of the pipe (respect to the penetration depth of the water) avoids the strong attenuation of the field due to the high losses of the medium. To better exploit this fact, multiple smaller pipes are used (instead of a central one), radially disposed around the longitudinal axis of the cavity. With this arrangement, to keep the same irradiation of the solution in every tube, a radial (ϕ-independent) mode needs to be used. As can be seen from table 3.1, the first mode that satisfies the radial condition is the TM_{01} (figure 3.2) which is then chosen for the design. The physical dimensions of the cavity are selected on the basis of operating frequency, so that

the TM_{01} mode occurs at that frequency. There are a few constrains in choosing the working frequency. It is known that water has its highest losses at frequencies around 10 GHz, which slightly moves depending on the temperature of exercise, but for the previous consideration a too high frequency have to be avoided, to keep the penetration depth as high as possible. Between the ISM (free licence) bands, the two closest frequency bands are at 2.45 GHz and 5.8 GHz, so the former is chosen for this application.

The use of equation (3.1.17) has been obtained for a cavity filled with a homogeneous dielectric, but can still be used as a starting point to fix the dimension of the cavity. In fact, in the formula, only the radius a and the ratio l/d have to be determined. For the radius, commercial tubes with standard dimensions are available and the diameter of $2a = 72.1\,\text{cm}$ is used, so that only the length d and an appropriate l-number remain to be fixed. The latter is chosen such that a length d greater than the diameter can be used to obtain the wanted resonant frequency.

Before the choice of the length, the dielectric constant requires further attention. As stated before, the formula (3.1.17) is valid for a cylindrical cavity filled with an homogeneous medium and, if tubes filled with water pass through the cavity the condition is not respected anymore. Thus an equivalent dielectric constant is used that can be estimated as a weighted mean of the dielectric constants of the water, the air and the tubes, being the weights the volumes of the corresponding materials

$$\epsilon_{avg} = \frac{V_a\epsilon_a + V_p\epsilon_p + V_w\epsilon_w}{V_a + V_p + V_w} \tag{3.2.1}$$

where V is the volume and ϵ the dielectric constant, the subscript indicating the material (a – air, p – pipe, w – water). A better approximation can be obtained using a correcting factor that takes into account the field inhomogeneity (at least in part), introducing F_w as

$$F_w = \left|\frac{E(r_c)}{E(0)}\right|^2 \tag{3.2.2}$$

and correcting equation (3.2.1) in

$$\epsilon_{avg} = \frac{V_a\epsilon_a + V_p\epsilon_p + V_w\epsilon_w F_w}{V_a + V_p + V_w} \tag{3.2.3}$$

where r_c is the distance between the cavity axis and the tube axis, while $E(r)$ is the field in the empty cavity. The distance of the tubes from the axis of the cavity can be chose to center the resonant frequency of the mode to the desired working frequency.

Finally, the cavity is fed by a coaxial line at $50\,\Omega$. Given the geometry and the

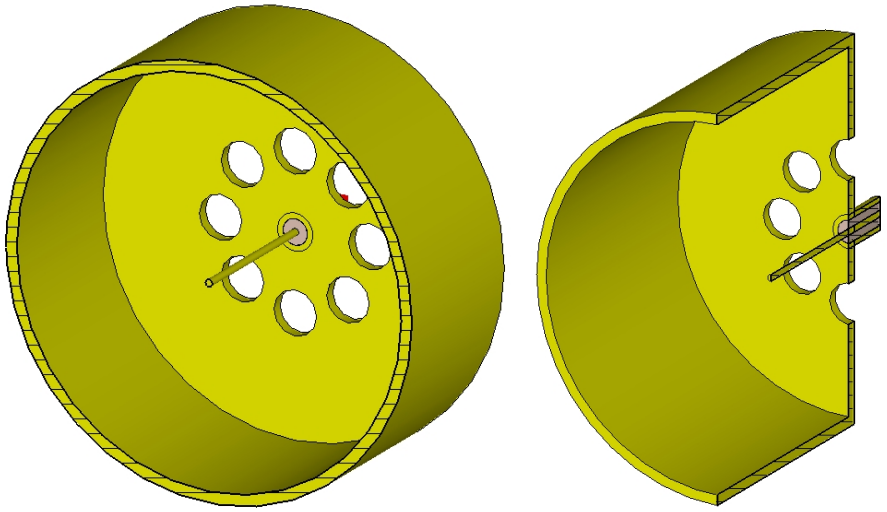

Figure 3.3

radial mode chosen, the line is disposed coaxially with the cavity, and only the core enter inside the cavity as shows the figure 3.3, so that it can best excite the required mode. Small variation of the length of the core inside the cavity can be used to a fine tuning of the resonant frequency.

3.3. Multiphysics Theoretical Model Description

3.3.1. Fluid Dynamics

To have, inside the tubes, the most favorable conditions of reproducibility, it was chosen to focus our attention, from the fluid dynamic point of view, on the laminar flow regime. In fact, such kind of fluid motion consists of the lowest mixing level as possible, and all the fluid elements advance in the axial direction, with the radial and azimuthal components of the velocity vector being zero. For cylindrical smooth pipes, as the used plexiglass tubes can be approximately considered, the laminar flow regime takes place for $Re < 2100$, being Re the *Reynolds number*, which can be defined as follows

$$Re = \frac{\rho u_z d}{\mu} \tag{3.3.1}$$

in which u_z is the axial component of the velocity vector, d the tube diameter, and μ the dynamic viscosity of the fluid. Considering the fluid at the temperature of 55 °C (near to the operating condition), the critical value of u_z is about 0.192 m/ s.

The fluid dynamics model, working in the laminar flow regime with an incompressible flow, was described by the continuity and Navier-Stokes equations, respec-

tively

$$\nabla \cdot \vec{\mathbf{u}} = 0 \tag{3.3.2}$$

$$\rho \left(\vec{\mathbf{u}} \cdot \nabla \right) \vec{\mathbf{u}} = \nabla \cdot \left[-p\mathbf{I} + \mu \left(\nabla \vec{\mathbf{u}} + \left(\nabla \vec{\mathbf{u}} \right)^T \right) \right] \tag{3.3.3}$$

in which $\vec{\mathbf{u}}$ is the velocity vector, ρ the fluid density, p the pressure, μ the dynamic viscosity, and $\vec{\mathbf{F}}$ the external force field.

Heat transfer in the fluid was described by the following energy conservation equation:

$$\rho C_p \, \vec{\mathbf{u}} \cdot \nabla T + \nabla \cdot (-k \nabla T) = Q \tag{3.3.4}$$

in which C_p is the heat capacity at constant pressure, T the temperature, k the thermal conductivity, and Q the power coming from a generic heat source.

To solve the previous equations it was necessary to define all the fluid properties as a function of temperature considering that it has a nonuniform distribution inside the tube reactor, and the fluid changes its thermal condition while flowing from the entrance to the outlet of the cavity. This kind of dependence, for ρ, C_p, k, and the dynamic viscosity of fluid (μ), was derived from the experimental data in [21], taken for a pressure of 1 bar and in the temperature range 20 °C to 99 °C.

From a polynomial regression of these data, the following correlations (in which T is in kelvin) have been obtained (the determination coefficient was higher than 0.9997 in all cases)

$$\rho \left[\frac{\mathrm{kg}}{\mathrm{m}^3} \right] = -3.0700 \times 10^{-3} \, T^2 + 1.5406 \, T + 8.1070 \times 10^2 \tag{3.3.5}$$

$$\begin{aligned} C_p \left[\frac{\mathrm{J}}{\mathrm{m\,K}} \right] &= 1.3130 \times 10^{-6} \, T^4 - 1.7788 \times 10^{-3} \, T^3 + \ldots \\ &\cdots + 9.1070 \times 10^{-1} \, T^2 - 2.0826 \times 10^2 \, T + 2.2088 \times 10^4 \end{aligned} \tag{3.3.6}$$

$$k \left[\frac{\mathrm{W}}{\mathrm{m\,K}} \right] = -9.8664 \times 10^{-6} \, T^2 + 7.5702 \times 10^{-3} \, T - 7.7262 \times 10^{-1} \tag{3.3.7}$$

$$\begin{aligned} \mu \left[\mathrm{Pa\,s} \right] &= -1.2714 \times 10^{-9} \, T^3 + 1.3767 \times 10^{-6} \, T^2 + \ldots \\ &\cdots - 5.0093 \times 10^{-4} \, T + 6.1556 \times 10^{-2} \end{aligned} \tag{3.3.8}$$

To have the highest reaction yields, from the thermal point of view, it was chosen to work near the optimal temperature for the specific enzyme here considered, which is about 55 °C, and avoiding the overcoming of the enzyme deactivation temperature, which is about 60 °C if this temperature is maintained for times longer than 60 min, as reported by [22]. To do this, and indicating with ΔT the difference between the maximum temperature of 60 °C and the inlet fluid temperature, the

ratio between the incident microwave power (P) and the fluid advancing velocity (and so the mass flow rate) multiplied for ΔT was fixed and maintained at a constant value ($8.12 \times 10^2\,\mathrm{N/m}$) for each run

$$\frac{P}{u_z \Delta T} = \text{constant} \tag{3.3.9}$$

Thus, in the multiphysics simulations, three different values of ΔT were considered (2 K, 5 K and 10 K), and the chosen couples of P and u_z are reported in Table 3.2.

3.3.2. Chemistry

The enzyme reaction is modeled using the kinetic described by Michaelis and Menten [23], which describes the basic mechanism for enzyme reactions as

$$\mathrm{E} + \mathrm{S} \underset{\mathrm{k}_{-1}}{\overset{\mathrm{k}_1}{\rightleftharpoons}} \mathrm{ES} \xrightarrow{\mathrm{k}_2} \mathrm{E} + \mathrm{P} \tag{3.3.10}$$

where S and E are respectively the free substrate and the enzyme molecules, ES the enzyme-substrate complex and P the reaction product, while k_1, k_{-1} and k_2 are the kinetic constant of the complex direct and inverse formation and of the product formation, respectively.

The evolution of the concentrations (indicated as [A] for the species A) is described by the following nonlinear system

$$\begin{aligned} \frac{\mathrm{d[S]}}{\mathrm{dt}} &= -\mathrm{k}_1[\mathrm{E}][\mathrm{S}] + \mathrm{k}_{-1}[\mathrm{ES}] \\ \frac{\mathrm{d[E]}}{\mathrm{dt}} &= -\mathrm{k}_1[\mathrm{E}][\mathrm{S}] + (\mathrm{k}_{-1} + \mathrm{k}_2)[\mathrm{ES}] \\ \frac{\mathrm{d[ES]}}{\mathrm{dt}} &= \mathrm{k}_1[\mathrm{E}][\mathrm{S}] - (\mathrm{k}_{-1} + \mathrm{k}_2)[\mathrm{ES}] \\ \frac{\mathrm{d[P]}}{\mathrm{dt}} &= \mathrm{k}_2[\mathrm{ES}] \end{aligned} \tag{3.3.11}$$

from which it can be seen that the enzyme concentration is preserved

$$\frac{\mathrm{d[E]}}{\mathrm{dt}} + \frac{\mathrm{d[ES]}}{\mathrm{dt}} = 0$$

and the mass conservation principle is respected

$$\frac{\mathrm{d[S]}}{\mathrm{dt}} + \frac{\mathrm{d[ES]}}{\mathrm{dt}} + \frac{\mathrm{d[P]}}{\mathrm{dt}} = 0$$

Finally, considering the relatively high energy status of the enzyme-substrate com-

plex, the pseudo steady (quasi-steady) state approximation is applicable,

$$\frac{\mathrm{d[ES]}}{\mathrm{dt}} \approx 0$$

f Introducing the Michaelis-Menten rate constant, defined as

$$\mathrm{K_M} = \frac{\mathrm{k_{-1} + k_2}}{\mathrm{k_1}} \tag{3.3.12}$$

the substrate consumption rate can be expressed as

$$\frac{\mathrm{d[S]}}{\mathrm{dt}} = -\frac{\mathrm{k_2\,[E][S]}}{\mathrm{K_M + [S]}} \tag{3.3.13}$$

which, if the substrate is present in very low concentration, so that $[\mathrm{S}] \ll K_M$, it becomes the first-order reaction rate

$$\frac{\mathrm{d[S]}}{\mathrm{dt}} = -\frac{\mathrm{k_2\,[E]}}{\mathrm{K_M}}[\mathrm{S}] \tag{3.3.14}$$

For the purposes of the simulations here presented, having considered an aqueous solution of sucrose to be hydrolysed, according to literature reports [24], for $\mathrm{K_M}$ the value of $0.06\,\mathrm{mol/\,dm^3}$ was taken, while the value of $\mathrm{k_2}$ was calculated through the relationship given by [25]

$$k_2 = \frac{k_B T}{h} \exp\left(-\frac{\Delta G^+}{RT}\right) \tag{3.3.15}$$

where k_B, h and R are respectively the Boltzmann constant, the Planck constant and the universal gas constant, T is the temperature and ΔG^+ is the Gibbs free energy variation associated with the reaction, for which the value $\Delta G^+ = 88\,\mathrm{kJ/\,mol}$ has been used, while for the initial enzyme concentration $[\mathrm{E}]_0 = 10\,\mathrm{mg/\,dm^3}$ is used [26].

In addition, a first-order enzyme deactivation in a single step is considered, so that the still active enzyme at time t is [27]

$$[\mathrm{E}]{=}[\mathrm{E}]_0 \exp\left(-\mathrm{k}_d\,\mathrm{t}\right) \qquad \text{with} \qquad k_d = \frac{k_B T}{h} \exp\left(-\frac{\Delta G_d}{RT}\right) \tag{3.3.16}$$

being $\Delta G_d = 103\,\mathrm{kJ/\,mol}$ and where the time t is evaluated considering that the liquid inside the pipe flows at a longitudinal velocity of v_{in}, so that it sweep a distance of z in $t = z/v_{in}$ units of time. Putting together the last considerations,

the final expression of the reaction rate becomes

$$R_c = \frac{\mathrm{d[S]}}{\mathrm{dt}} = -\frac{\mathrm{k_2\,[S]}}{\mathrm{K_M}}\mathrm{[E]} = \cdots \tag{3.3.17}$$

$$\cdots = -\frac{\mathrm{[S]}}{\mathrm{K_M}}\frac{k_B T}{h}\exp\left(-\frac{\Delta G^+}{RT}\right)\mathrm{[E]}_0\exp\left(-k_d\frac{z}{v_{in}}\right) \tag{3.3.18}$$

$$\tag{3.3.19}$$

where [S] is the initial concentration of sucrose.

3.4. Simulations and Results

3.4.1. Simulation Description

The simulation has been carried out using two commercial simulation software. The electromagnetic software CST Microwave Studio was used as a starting point for the design of the cavity from an electromagnetic point of view, keeping into account the temperature variation as a corresponding dielectric constant variation.

The designed cavity was then drawn in COMSOL Multiphysics, a numerical simulator that allows performing a wide range of calculations in different scientific areas (referred by the software as *Physics*) such as electromagnetics, fluidodynamics, heat transfer, mechanics, chemistry, acoustics and many others. In addition to simulations of a single area, COMSOL allows performing *full coupling* simulations, i.e. to couple simulations of different field, such that the effects of phenomena of a specific area can influence parameters and behaviors of the other areas.

For the purpose of this study, four different *physics* have been used, namely (using the same nomenclature of the software) *Electromagnetic Waves*, *Heat Transfer in Fluids*, *Laminar Flow* (the fluid dynamics simulation) and *Transport in Diluted Species* (the chemical simulation).

Furthermore, to couple these physics, different *multiphysics* has been used. In particular, an *Electromagnetic Heat Source* and a *Boundary Electromagnetic Heat Source* allows to introduce the heating generated by microwaves in the materials used. The heat in turn influences the electromagnetic parameters of the corresponding physic and so a *Temperature Coupling* between the *Heat Transfer in Fluids* and the *Electromagnetic Waves* physics has been used. In addition, a *Non-Isothermal Flow* was used to couple the *Laminar Flow* to the *Heat Transfer in Fluids*. Finally, a *Flow Coupling* and a *Temperature Coupling* was initially used to couple respectively the *Laminar Flow* and the *Heat Transfer in Fluids* with the *Transport in Diluted Species*.

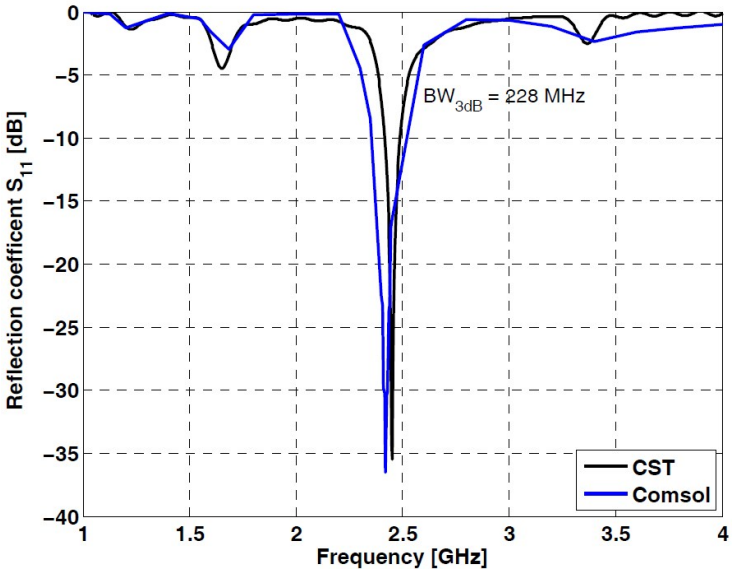

Figure 3.4

Due to the complex problem at hand, the simulation was solved in different steps. As a first step the electromagnetic simulation was carried out singularly. A quick comparison with the results obtained by CST Microwave Studio has been done. As a representative example of this comparison, in figure 3.4 is reported the reflection coefficients obtained by the two software. It can be seen that the results are in good agreement.

As a second step, a simulation including the coupling between the fluid dynamics and the heat transfer has been conduct. In particular, in this simulation, the heat source was obtained by the joule heating caused by the presence of the electromagnetic field calculated by the previous simulation. This step was necessary to obtain coherent conditions for the fluid dynamics physics for the next step. It is worth notice that the results at this point are not obtained by a full coupling simulation because the electromagnetic one was solved separately.

The final step was to use the previous solution as a starting point to calculate the full coupling solution between electromagnetics, heat transfer, fluid dynamics and chemical reaction. This step is the most resource consuming of the study.

In the attempt to speed up the process, the *Transport of Diluted Species* can be solved apart, assuming that the reaction doesn't influence the electromagnetic, fluid dynamic and thermal properties of the materials (which is a realistic assumption considering that the reaction occurs in an aqueous solution, i.e. using very low concentration of reagent and enzyme). In this case, the full coupled simulation is performed considering electromagnetic, laminar flow and heat transfer physics. The

chemical simulation is executed independently, using the variables calculated in the three-physics full coupled simulation.

3.4.2. Results

The procedure described in section 3.2 allows to design the cavity to work at the temperature at which the reaction should occur. The cavity thus obtained can be analyzed to study its behavior in different conditions. In figure 3.5a the reflection coefficent at different temperatures of a cavity designed to be matched at 20 °C are reported. It can be seen how the raise of temperature casues a shift to a higher frequency of the dip and reduces it. This is due to the reduction of the dielectric constant which has the effect to raise the resonant frequency of the modes and causes a mismatch with the feed line. The mismatch, in turn, causes a reduction of the absorbed power which means that the cavity isn't effective anymore in heating the water. This can be better seen in figure 3.5b where is shown how the power transmission coefficient (i.e. the coefficient of proportionality between incident power and absorbed power) at 2.45 GHz reduces with the raise of temperature. The red curve is obtained using the value of the reflection coefficient of the cavity, designed to be tuned (TM_{01} mode at 2.4 GHz) at 20 °C and shows that the power is largely reflected at high temperatures. The problem is partially solved tuning the cavity for every temperature. In blue curve, for every point the cavity as been re-tuned to center the mode at the working frequency. It can be seen that the absorbed power now is alway higher than 50%. The large variation of the dielectric constant with temperature makes it difficult to have a good match at high temperatures using only the physical dimension of the cavity to obtain it, but if a higher absorption is required, a λ-quarter transformer filled with a suitable dielectric can be used to nullify the reflection coefficient. Comparing different cavities, one of each designed to work at different temperatures, as shown in 3.6a, it can be seen how the power absorbed stays almost constant up to the temperature design T_{res} and rapidly decrease above the same temperature. It is possible to infer a qualitative behavior that is schematically represented in figure 3.6b. This allows to design the cavity considering only the working temperature T_{w} required for the reaction.

The fields inside the cavity are shown in figure 3.7, where a coss-section and a longitudinal cut are shown. The former shows the azimuth-independent property of the field and how the field is modified (respect to the empy cavity) by the presence of the tubes. In the latter it can be seen the two oscillations along the z-direction, due to the use of a mode with $l = 2$, which means that two half wavelength (and then two oscillations) occurs along the axis of the cavity. The field inside a tube

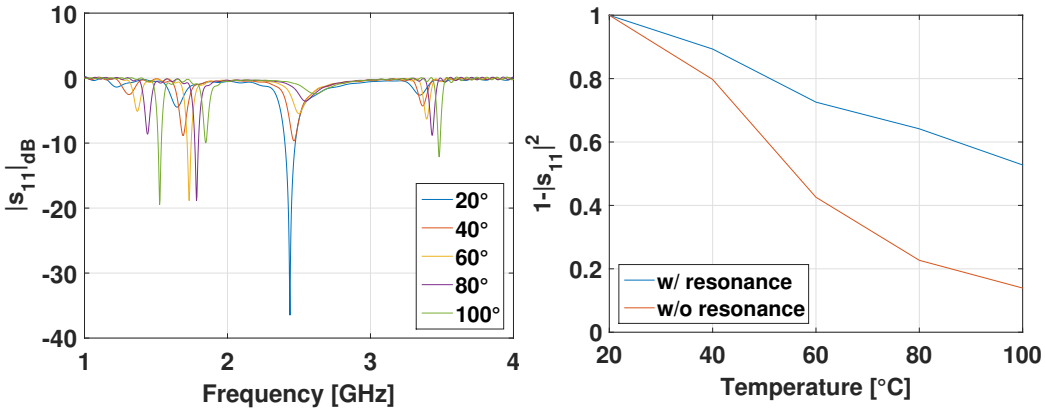

(a) Reflection Coefficient

(b) Absorbed Power

Figure 3.5

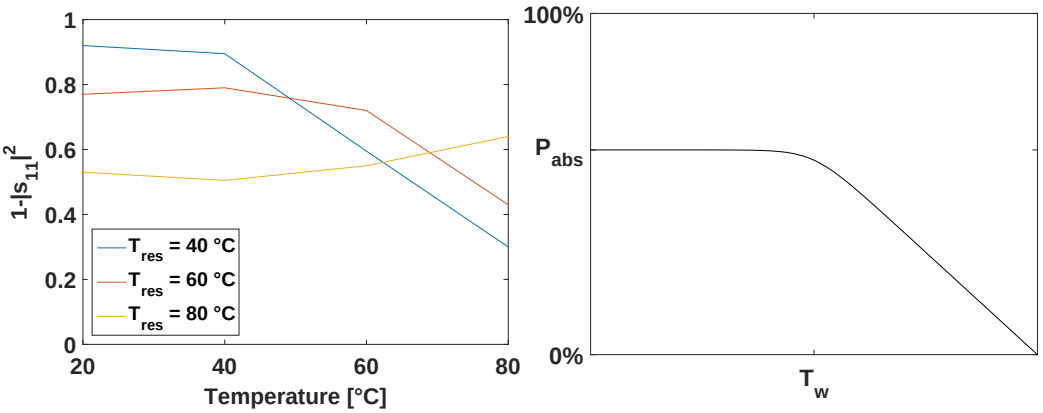

(a) Comparison of cavities designed to work at different temperatures

(b) Infered behavior

Figure 3.6

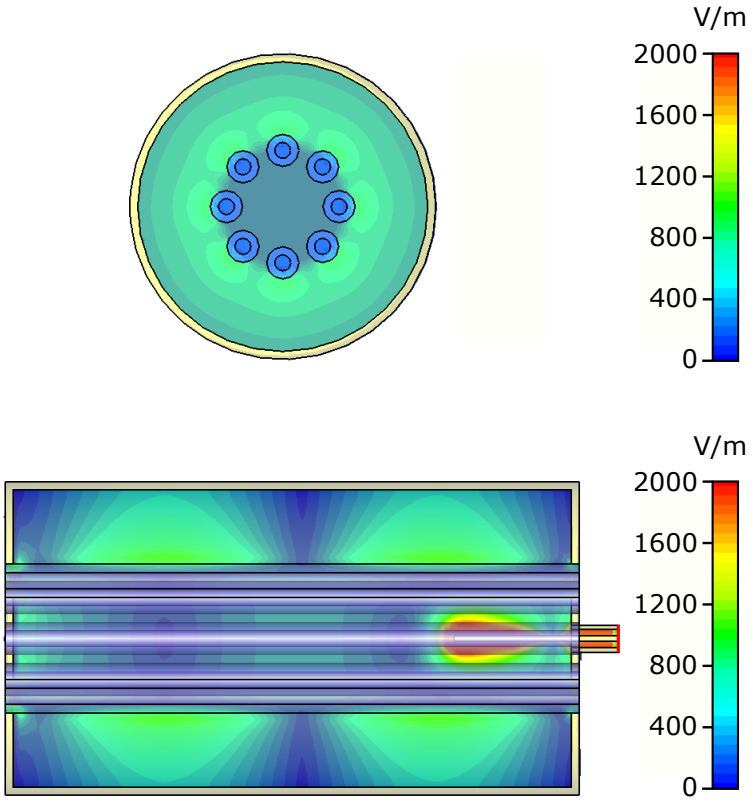

Figure 3.7 Sections of the cavity with the field reported

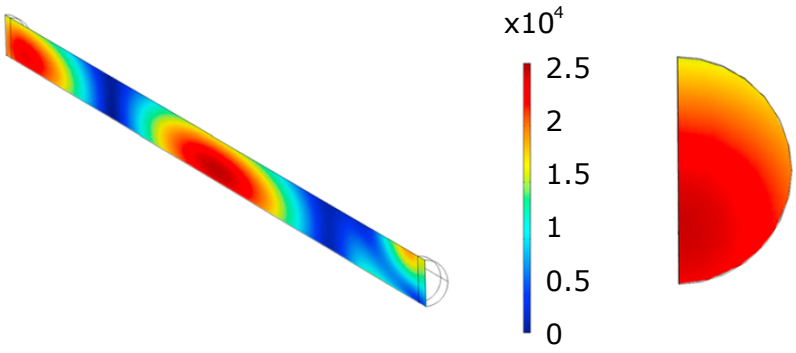

(a) Electric field [V/m]

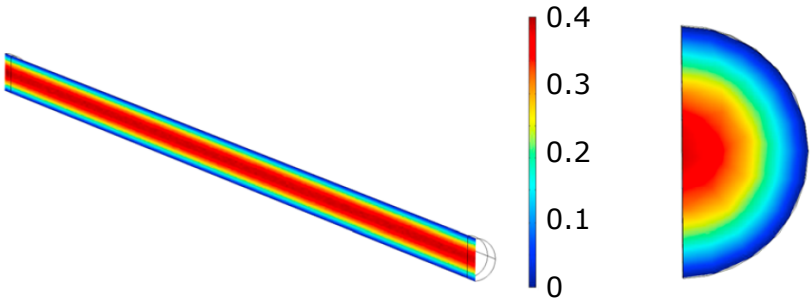

(b) Axial velocity [m/s]

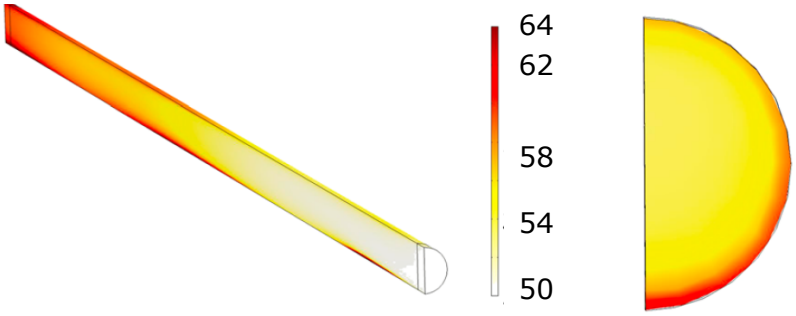

(c) Temperature [°C]

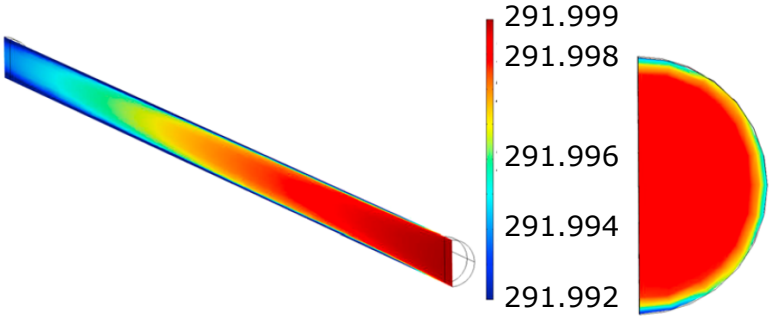

(d) Concentration distribution [mol/m^3]

Figure 3.8 Longitudinal and cross section of a tube

	T_i [°C]		
	50	55	58
u_z[m/s]		P [W]	
5×10^{-5}	1.35×10^{-1}	6.77×10^{-2}	2.71×10^{-2}
7.5×10^{-5}	2.03×10^{-1}	1.02×10^{-1}	4.06×10^{-2}
1×10^{-4}	2.71×10^{-1}	1.35×10^{-1}	5.41×10^{-1}
2.5×10^{-4}	8.12×10^{-1}	4.06×10^{-1}	1.62×10^{-1}
5×10^{-4}	1.35	6.77×10^{-1}	2.71×10^{-1}
7.5×10^{-4}	2.03	1.02	4.06×10^{-1}
1×10^{-3}	2.71	1.35	5.41×10^{-1}
2.5×10^{-3}	8.12	4.06	1.62
5×10^{-3}	1.35×10^{1}	6.77	2.71
7.5×10^{-3}	2.03×10^{1}	1.02×10^{1}	4.06
1×10^{-2}	2.71×10^{1}	1.35×10^{1}	5.41
2×10^{-2}	5.41×10^{1}	2.71×10^{1}	1.08×10^{1}
4×10^{-2}	1.08×10^{2}	5.41×10^{1}	2.17×10^{1}
6×10^{-2}	1.62×10^{2}	8.12×10^{1}	2.17×10^{1}
8×10^{-2}	2.17×10^{2}	1.08×10^{2}	4.33×10^{1}
1×10^{-1}	2.71×10^{2}	1.35×10^{2}	5.41×10^{1}
1.2×10^{-1}	3.25×10^{2}	1.62×10^{2}	6.50×10^{1}
1.4×10^{-1}	3.79×10^{2}	1.89×10^{2}	7.58×10^{1}
1.6×10^{-1}	4.33×10^{2}	2.17×10^{2}	8.66×10^{1}
1.8×10^{-1}	4.87×10^{2}	2.44×10^{2}	9.74×10^{1}
2×10^{-1}	5.41×10^{2}	2.71×10^{2}	1.08×10^{2}

Table 3.2 Sets of operating conditions for the multiphysics simulations of the resonant cavity with the reacting fluid flowing inside the multitube-irradiated reactor

can be seen in figure 3.8a, in a longitudinal and a cross section.

With the cavities properly designed to work at the three different temperatures indicated in section 3.3.1 and reported in Table 3.2, the multiphysics simulations have been carried out. The Table shows the operating conditions for every single simulation. The value of u_z is the inlet velocity of the fluid in the pipe, while the power is the incident power coming from the coaxial feed. For every couple of these two quantities, a simulation has been run.

To evaluate the effectiveness of the cavity for the reaction involved, the fractional conversion X is used for taking into account the evolution of the hydrolysis reaction. The conversion can be defined as follows

$$X = \frac{C_{\mathrm{i}} - C_{\mathrm{out}}}{C_{\mathrm{i}}} \tag{3.4.1}$$

where C_{i} is the initial concentration of sucrose, where the value of $292\,\mathrm{mol}/\,\mathrm{m}^3$ has been used as a reference value [Olmi et al., 2007; Casu et al., 2015], while C_{out} represents the sucrose concentration in the fluid outcoming from the cavity. In figure 3.9 is reported the conversion for every multiphysics simulation at the three different temperature of exercise. The results are compared with the conversion obtained using conventional heating, assuming the same amount of power given to the system. It is clear that microwave heating is more effective, especially at low inlet velocity, due to a better distribution of the electromagnetic field inside the water and consequently an optimal and faster heating, while for higher velocity the curves overlap, which is an indication of the fact that the solution don't stay enough time to be heated under the effects of the field.

In conclusion the robustness of the resonant cavity showed the possibility of operating with a fixed frequency microwave generator. The multiphysics simulation was necessary to consider all the physical and chemical phenomena occurring inside the resonant cavity and the tubes containing the reacting solution. In effect, it showed how the temperature distribution in the fluid is important in determining the effectiveness of the conversion process, and its knowledge allows a good control of the reaction conditions in order to prevent the enzyme deactivation and so greatly improving the possibility of reuse it in a process with multiple passages of the fluid inside the cavity. The most interesting operating conditions are those with average velocities between 2.5×10^{-4} and $2 \times 10^{-2}\,\mathrm{m}/\,\mathrm{s}$, as this range allows the best compromise among the highest reaction rate, good conversion values per single passage, and the limitation of the enzyme loss.

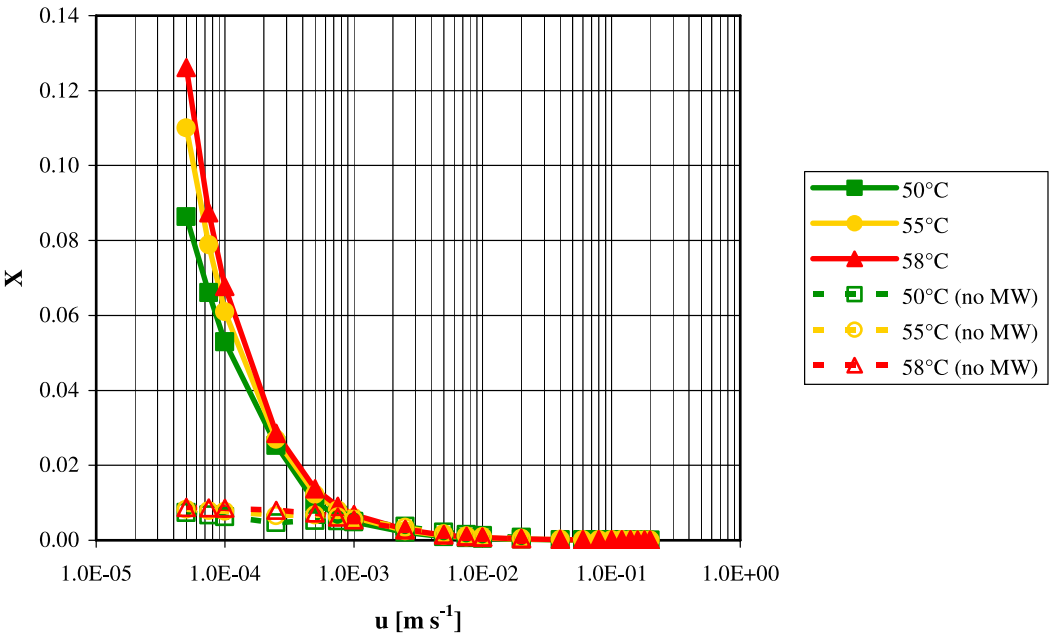
0.14
0.12
0.10
0.08
0.06
0.04
0.02
0.00
X
1.0E-05
1.0E-04
1.0E-03
1.0E-02
1.0E-01
1.0E+00
u [m s-1]
50°C
55°C
58°C
50°C (no MW)
55°C (no MW)
58°C (no MW)

Figure 3.9

Part II.

Medical Applications

4. Array of Coils for MRI

Magnetic resonance imaging (MRI) is a non-invasive medical diagnostic technique that provides information about changes in soft tissue structure and alterations inside internal organs [1]. In this technique, the proton spins of the interested body part, are first aligned in one direction by a static magnetic field, B_0, and then subject to a sequence of excitation by a radio frequency (RF) magnetic field, known as B_1 field, in the plane perpendicular to the B_0 field. More precisely, the B_1 field drives the protons into an excited state. After the exciting RF field is turned off, energy is released [2]. This energy can be measured and provides the magnetic resonance data. The frequency f_1 of B_1 field is proportional to the B_0 field $f_0 = \frac{\gamma B_0}{2\pi}$ being $\gamma = 42.6 \cdot 2\pi\,\mathrm{MHz/\,T}$ the gyromagnetic ratio [2]. Older MRI tomographic scanner employed low B_0-field (up to 1.5T, with f_1 less than 60 MHz), however modern trend is to use high-B_1 field (up to 7T and beyond), and therefore f_1 in the UHF rang [3].

RF coils are the component responsible for the sample excitation and for the detection of the signal it generates. Their function is therefore fundamental for MRI. Modern coils must ensure two main requirements, namely guarantee a large field of view (FoV) and a RF B_1 field as homogeneous as possible inside the sample [4]. The field homogeneity depends on the shape of the tissue-under-exam, but also on the geometric shape of the coil. Such shape can be chosen to fit the TUE, in order to be worn comfortably for a tomography lasting some tens of minutes. A

better FoV can be obtained by an array of coils, i.e. in two or more overlapped or closely positioned RF coils that simultaneously receive the MR signal from a bigger region of interest than a single coil [5–7]. Such multiple coils are, however, quite large and therefore they need to be geometrically adjustable to the subject to analyse [8]. A flexible receiver RF array is a device that offers several benefits, because it allows the adjustment of the coil geometry to the subject and, provides the better filling factors and improved SNR for different subjects while keeping a large field of view (FoV) of operation [9–11]. Flexible coils have already been used for various application such as wrist analysis [12], bile duct MRI [13] and human knee [14].

For MRI systems that use a low B_0 field, the frequency of the field is so low that the size of the biological object to be imaged is usually only a small fraction (less than 20%) of the wavelength of the field. Hence, the interaction between the object and the electromagnetic field is relatively weak [3]. Low-field MRI, therefore has quite small signal-to-noise ratios (SNR) and, as a consequence, reduced image quality [15].

High-quality images call for a MRI coil with a high SNR. In order to reach such high SNR, high frequency MRI systems using high magnetic fields (> 3T) have been developed [16–20]. Since the coil is a Faraday law-based sensor, the signal power is quadratic in the MRI frequency and then in the B_0 field, thus leading to a strong increase in SNR. However, as a result of the increased frequency, the size of the biological object becomes comparable to or even larger than the effective wavelength and the interaction between the biological tissues and electromagnetic field becomes much stronger raising safety concerns for the MRI systems [21].

Specific Absorption Rate (SAR) [22] is a measure of the rate of electromagnetic energy absorbed by the human body when it is exposed to the action of a radiofrequency electromagnetic field. The limits for RF exposure during MRI in volume transmit coils are defined by [22]. The SAR within the patient must remain under the following limits:

- normal: head SAR (SARhead), whole-body SAR (SARwb), and partial-body SAR (SARpb) of 3.2 W/kg, 2.0 W/kg, and from 2 to 10 W/kg, respectively
- first level controlled: SARhead, SARwb, and SARpb of 3.2 W/kg, 4.0 W/kg, and from 4 to 10 W/kg, respectively

The tolerated SAR and the associated thermal loading may be identified as prime safety considerations and as the limiting factors in clinical magnetic-resonance applications [23]. In fact, when applying radio frequency (RF), only a small percentage of the energy applied is absorbed by the MR-sensitive nuclei. The remaining energy

is converted to heat in the conducting tissue in the field of view of the coil [24]. This situation worsen with the proximity of the RF device and the human sample that has to be investigated, as in the case of flexible coils, and must be carefully monitored.

Recognizing the increased role of tissue/coil interactions, experimental and numerical evaluations of RF coils can provide essential information for understanding the behaviour of these devices. In addition, such studies can help to devise coil design modifications required to retain reasonable homogeneity for the B_1 field distribution and to minimize RF power deposition as monitored by the SAR.

The prediction of electric field distribution inside the sample is the starting point to evaluate, and control, SAR. Since in vivo measures of electric fields is impossible, it is extremely useful to exploit numerical methods for studying high-field MRI applications on human body [25–29]. Different studies have been performed to evaluate safety issues in MRI high field applications by computing the power absorbed by on human head during a 7T-MRI exam using an 8-channel ship array [30], the local SAR for a MRI multi-transmit body coil [31] and the tissue temperature rise in the case of a pregnant female model using a 16-channel birdcage coil [32]. Other studies have analyzed the MRI compatibility with other devices such as defibrillator [33] or the effect of different MRI sequences on the safety of the patient [34].

4.1. MRI Principles

MRI exploit a property of atomic nucleus called intrinsic spin angular momentum, or simply spin [35]. It can be considered due to a constant rotation about an axis at a constant rate, the axis being perpendicular to the direction of rotation.

The spin can assume a limited number of values, i.e. its a quantized amount. There are three types of these values, zero, half-integer values and integer values, depending on the atomic weigth and the atomic number. The value zero leads to nuclei that don't interact with external magnetic fields, while a nucleus having an half-integer value or an integer value is influenced by magnetic fields.

The nucleus of protium ^{1}H (the most abundant isotope for hydrogen found in nature) for example, consist of a single proton, has a spin of 1/2 and its response to an applied magnetic field is one of the largest found in nature. The human body is composed of tissues that contain primarily water and fat, both of which contain hydrogen, which makes it a good choice to be used for medical applications.

A volume of a tissue contains plenty of protons (hydrogen atoms). Every atom has its own spin vector, equal in magnitude to the others but oriented randomly. If

all the spins are summed together, the sum would be zero, due to the randomness of the orientation. If the tissue is placed in a magnetic field B_0, the atom starts to rotate perpendicular to the magnetic field. The protons are tilted slightly away from the axis of the field but the axis of rotation is parallel to B_0. The precession moto arised occurs at a constant rate, which is proportional to the field and is given by

$$f_0 = \frac{\gamma B_0}{2\pi} \tag{4.1.1}$$

γ being a constant called *gyromagnetic ratio* which for the atom of hydrogen assumes the value of $\gamma = 2\pi \cdot 42.6\,\mathrm{MHz/\,T}$, and f_0 is called the *Larmor frequency*.

By convention, B_0 and the axis of precession are defined to be oriented in the z direction of a Cartesian coordinate system. The motion can be described by its cartesian components, x, y and z. All the components are nonzero. The z component parallel to the field is constant in time while the perpendicular components vary in time.

If a vector addition is performed, under the effect of the magnetic field, the components perpendicular to the external field would still be zero. But, because there is an orientation of the precessional axis of the proton that is constant in time, there is a constant nonzero interaction or coupling between the proton and B_0, known as *Zeeman interaction*. This coupling causes a difference in energy between protons aligned parallel or along B_0 and protons aligned antiparallel or against B_0, which is proportional to B_0. The antiparallel alignment is the one at the highest energy and occurs less than the parallel one. This unequal number of protons in the two different states causes the vector sum of the spin to be nonzero and will point as the more numerous position, parallel to the field B_0. In other words, the tissue will become polarized or magnetized. The magnitude of the polarization M_0 is constant in time and proportional to B_0

$$M_0 = \chi B_0 \tag{4.1.2}$$

where χ is the magnetic susceptibility. This induced magnetization is the source of signal for all of the MR experiments. Consequently, all other things being equal, the greater the field strength, the greater the value of M_0 and the greater the potential MR signal. The magnetic resonance techniques are based on the manipulation of M_0. If a short radio-frequency pulse is applied, a given amount of its energy is absorbed by the protons. The pulse is contains many frequencies spred over a narrow range, but only the energy at a particular frequency is absorbed which is proportional to the magnetic field B_0 and follows the Larmor equation (4.1.1). The

absorption of this energy causes the proton to transit from the low energy state to the next energy level. The energy difference between the two states is proportional to f_L and thus to the magnetic field B_0

$$\Delta E = \frac{h\gamma B_0}{2\pi} \tag{4.1.3}$$

where h is Plank's constant ($6.626 \times 10^{-34}\,\mathrm{J\,s}$). Only energy at this frequency stimulates transitions between the spin up and spin down energy levels. This quantized energy is known as *resonance energy* while the frquency of energy is called *resonant frequency*. From a magnetization point of view, the pulse B_1 is chosen to be perpendicular to B_0, at a frequency of f_L such that

$$\vec{\mathbf{B}}_1 = 2B_{RF}\cos\omega_L t\,\vec{\mathbf{i}}_x \tag{4.1.4}$$

This orientation allows a coupling between the RF pulse and M_0 so that the energy can be transferred to the protons. The effect of the pulse on the magnetization vector is a rotation toward the xy-plane. If the amplitude of the pulse is high enough and the last of the pulse is sufficiently long M_0 rotate entirely into the transverse plane so that there will be no more longitudinal magnetization. In this case the pulse is called a 90° *pulse*. When the pulse is turned off, the protons release the energy absorbed and goes back to their original equilibrium orientation while releasing energy. The time after which it reaches its initial state is random but its mean value is influenced by how much the proton is bonded to the surrounding molecules, the more the bonding the fast the final state is reached. This time is indicated as T_1 and is characteristic for every material. The law governing the refurbishment of the magnetization along z is the following

$$M_z = M_0\left(1 - \exp^{-\left(\frac{t}{T_1}\right)}\right) \tag{4.1.5}$$

Another effect of magnetization decay occurs to the perpendicular magnetization, when the 90° pulse is turned off. At the end of the pulse in fact the magnetization is on the xy-plane and all the protons are rotating at the same angular frequency $\omega_L = 2\pi f_L$. Due to the interaction between the magnetic momentum of the protons, their angular velocity will be varying in a random way, and the protons that at the end of the pulse were all in-phase to each other, will start to be oriented in a random way on the plane, until they will be uniformly distributed on the xy-plane an there will not be any magnetization on the plane. The law describing the magnetization

is in the form

$$\vec{\mathbf{M}}_{xy} = M_0 \exp\left[-\frac{t}{T_2}\right]\left(\sin\omega_L t\ \vec{\mathbf{i}}_x + \cos\omega_L t\ \vec{\mathbf{i}}_x\right) \tag{4.1.6}$$

being t_2 the time constant characterizing the phenomenon.

The two mechanisms described above are independent because the first one is due to the interaction between protons and the tissue while the other is owed to the spin-spin interaction. The time constant T_2 is much more smaller than T_1, usually one order of magnitude, and independent of B_0, while T_1 is a increasing function of B_0. In any case, they both depend on the tissue.

Actually, to worsen the effect of the phase-shift between the protons there is also the dishomogeneity of the static field B_0. If the time constant due to this effect is T_{2L}, the decay of the magnetization becomes

$$\begin{aligned}\vec{\mathbf{M}}_{xy} &= M_0 \exp\left[-\frac{t}{T_2}\right]\exp\left[-\frac{t}{T_{2L}}\right]\left(\sin\omega_L t\ \vec{\mathbf{i}}_x + \cos\omega_L t\ \vec{\mathbf{i}}_x\right) = \dots \\ \dots &= M_0 \exp\left[-\frac{t}{T_2^*}\right]\left(\sin\omega_L t\ \vec{\mathbf{i}}_x + \cos\omega_L t\ \vec{\mathbf{i}}_x\right)\end{aligned} \tag{4.1.7}$$

where the constant T_2^* has been introduced, that takes into account the two effects.

4.2. Spatial Coding

To reconstruct an image of the tissue under test, it is necessary to recognize the signals emitted by protons in different locations. This is done using an additional field, varying linearly in the region of the tissue, so that the total static field is

$$\vec{\mathbf{B}} = (B_0 + G_z z)\,\vec{\mathbf{i}}_z \tag{4.2.1}$$

that causes the Larmor frequency to be variable to z

$$f_L(z) = \frac{1}{2\pi}\gamma\,(B_0 + G_z z) = f_{L0} + \frac{\gamma G_z}{2\pi} z \tag{4.2.2}$$

For a region that extend for L_z, the range of frequency will be

$$\left[f_{L0} - \frac{\gamma G z}{2\pi}\frac{L_z}{2},\quad f_{L0} + \frac{\gamma G z}{2\pi}\frac{L_z}{2}\right] \tag{4.2.3}$$

with a bandwidth of

$$B_T = \frac{\gamma G_z}{2\pi} L_z \tag{4.2.4}$$

so that if an RF signal is generated with a bandwidth over the same range of frequencies, it will excite the different zones of the body at their different resonant frequencies. The frequencies of the signal emitted are at the same frequency so that every frequency corresponds to a particolar region of the body. A spectral analysis of the signal would allow to obtain a map of the human body.

However, in pratice the signal used is a pulse with a band B_w narrow than B_T, and different pulses in adjacent bands are used. In this way only the part of the body in a small interval of z values are exited so that

$$\begin{aligned} B_W &= \frac{\gamma G_z}{2\pi}\Delta z \\ \Delta z &= \frac{2\pi B_W}{\gamma G_z} \end{aligned} \tag{4.2.5}$$

This means that the reconstructed image is obtained by different zones of length Δz, called *slices*, acquired once per time, being Δz the spatial resolution along the z direction. Typical values of B_W are comprised in the range 500 Hz–1000 Hz while the order of magnitude of G_z is 10 mT/ m.

In the same way, gradients along x and y directions are used to discriminate different points in the same slice. When the RF pulse and the gradient along z are turned off, the gradient along y is activated for a time T_y so that the static field becomes $\vec{\mathbf{B}} = (B_0 + G_y y)\,\vec{\mathbf{i}}_y$, the angular frequency will be a function of y expressed as $\omega_{L0} + \gamma G_y y$. When the y-gradient is turned off, the dipoles are not aligned but oriented with an angle dependent on y given by $\Phi(y) = (\gamma G_y y)T_y$. The same process is repeated for the x direction so a static field $\vec{\mathbf{B}} = (B_0 + G_x x)\,\vec{\mathbf{i}}_x$ is generated after which the signal is registered. If a pulse of 90° is used, the polarization along x and y are given by

$$\begin{aligned} M_x(t) &= M_0 \exp\left[-\frac{t}{T_2^*}\right] \sin\left[\omega_{L0} + \gamma G_x x)t + \Phi(x)\right] \\ M_y(t) &= M_0 \exp\left[-\frac{t}{T_2^*}\right] \sin\left[\omega_{L0} + \gamma G_y y)t + \Phi(y)\right] \end{aligned} \tag{4.2.6}$$

4.3. RF Coils

The devices used to excite and receive the signals emitted by the excited nuclei are the RF coils. The pulse transmission and the receiving of the signal can be done both by the same coil or by using a different coil for every operation. The latter solution is generally preferred (if possible) because the required characteristics of a coil are different depending on the duty of the device. A requirement for

Figure 4.1 An example of birdcage coil for MRI

transmission coil for example is to obtain the most homogeneous field possible in the volume considered, while the receiving coil the most important specifications is to obtain the higher sensibility in the region of interest. Thus, the transmitter and receiver need to be accurately designed for the specific application to obtain the best quality of the image.

There are mainly two types of RF coils for MRI, the volume coils and the surface coils. The former are closed structures in which the sample is positioned. Typical volume coils are composed of two rings with the same dimensions, coaxially aligned and joint together by a number (usually even) of segments called *legs*. The volume coils guarantee a wide field of view but they lack of a good signal to noise ratio. An important parameter of these coils is the *Filling Factor*, which is an indication of how much the sample fills the volume surrounded by the coil. In fact, the greater the filling factor, the smaller the empty volume that don't contribute to the signal but contribute to the noise. In figure 4.1 is pictured an example of a widespread volume coil, called *birdcage*.

The other type of coils are the surface coils, which are open structures able to receive a signal from adjacent superficial samples. Their signal to noise ratio is higher than the one achieved by volume coils, thanks to their limited sensitivity region which reduces the noise received. On the other hand, they are characterized by a restricted field of view, whereas a field of view as wide as possible is desirable in clinical imaging. To overcome this problem, and keeping the same signal to noise ratio, multiple coils close to each other to form an array are used. When a phased array is used for example, multiple coils are posed in parallel and every coil receive an RF signal, independent from the others, from its own sector and then the signal

received from the coil is elaborated and summed with the others to obtain a global image.

For the sake ok completeness a simple expression for the SNR, evaluated for the smallest region (called *voxel*) identified by a signal, is reported. The expression [35]

$$\mathrm{SNR}_k = \frac{V_{\mathrm{signal}}}{V_{\mathrm{noise}}} = \frac{\sqrt{2}\omega_0 \Delta V M_{xy} |B_t|}{\sqrt{4kT\Delta f R_{\mathrm{in}}}} \tag{4.3.1}$$

highlights how the signal to noise ratio of a voxel is proportional to the field B_0 (because of ω_0), which is the main reason why the trend in the past years is to use magnetic field increasingly higher.

The term B_t, is the component of B_1 transverse to the field B_0, normalized to a unitary current, and is called *effective coil sensitivity*. The aim of an RF coil design is to obtain the best coil sensitivity to achieve the highest SNR.

Finally the denominator in 4.3.1 is the noise output of the coil, where Δf is the bandwidth, k is the Boltzman's constant, and T is the effective temperature and R_{in} is the noise resistance of the coil.

4.4. Surface Coil Design

In this work a surface coil is designed to be used in a ultra high field (7 Tesla) MRI. The RF coils are responsible for the generation of the RF pulse and the reception of the signal generated by the system as response to te pulse excitation.

The magnetic field at 7 Tesla makes the sample under test excitable at its Larmor frequency given by (4.1.1), in this case 298 MHz, which fixes the operating resonant frequency of the coil.

The design of a coil starts with its equivalent model [36] as a lumped element, characterized by an inductance L_{coil}. This equivalent lumped coil have to resonate at the Larmor frequency previously calculated, so a tuning capacitance is required the value of which can be obtained by the following

$$C_{\mathrm{coil}} = \frac{1}{\omega_0^2 L_{\mathrm{coil}}} \tag{4.4.1}$$

where ω_0 is the working angular frequency and L_{coil}, the lumped inductance, depends on the size and shape of the real coil [37].

For high field MRI (and then high frequency), the lumped element assumption is not is not accurate enough because the physical dimension of the coil are comparable to the wavelength [38]. This means that the current distribution along the coil is not constant, which is the condition for the lumped model.

In order to get an almost constant current distribution, the coil is divided into N equal section, each of one shorter than $\frac{\lambda}{10}$ [3] at ω_0, using a capacitor with capacity

$$C_t = \frac{C_{\text{coil}}}{N} \tag{4.4.2}$$

to connect two adjacent sections. In this way the current in a section is constant and thanks to the capacitors, is the same in each segment. The value of C_t is then used as a starting point to obtain a fine-tuning of the coil.

In order to match the coil to the $50\,\Omega$ impedance of the generator, a matching network is required. A capacitive matching is suitable for this application, so a matching capacitance is used, and placed in parallel to the input terminals of the coil [39].

The exact value of the tuning capacitance C_t and the matching capacitance C_m can be found using a full-wave electromagnetic simulator (e.g. Ansys HFSS, or CST Studio Suite for this work). The best way to proceed is to include in the simulation, a model of the sample that will be analyzed, because there is a strong coupling between the coil and the load and this influences the resonant frequency and the input impedance of the coil. A design of the coil without taking into account the load on which it will work on, brings to a not tuned and mismatched coil. This implies that a knowledge of the samples to analyze is required and the coil needs to be designed for a particular application.

The shape of the coil has been chosen to be accurate enough but at the same time as simple as possible to resemble to a planar circular loop coil, so an octagon has been chosen [40]. The particular shape was choose in view of a hand-made realization of a prototype, made of a conductive (copper) tape, avoiding complex shapes (too many edges) and avoiding angles between edges too close to 90°. In figure 4.2 is reported the designed octagonal coil, with a radius of $r_{\text{coil}} = 4.5\,\text{cm}$

4.5. Array of Two Coil Design

The improved SNR of a surface coil respect to a volume coil is limited to a restricted region close to the coil, more precisely to the center of the coil. This clearly limits the field of view, but reduces the noise received, being the main contribution due to the broadband thermal radiation from the sample.

To improve the field of view, a bigger coil can be used. In this way, although the device cover a wider area, the signal to noise ratio will be degraded. The *local* or *surface* coil acts as a spatial filter, eliminating noise detected from outside the region of interest. In figure 4.3 [35] for example, is reported the relative SNR of different

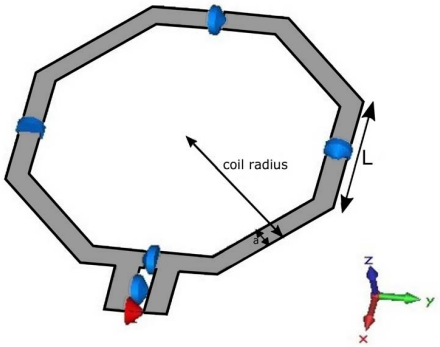

Figure 4.2 Single coil model, with the tuning and matching capacitors (blue arrows)

coil sizes evaluated in distinct positions. The figure 4.3a compare the performance of a circular loop coil with four different radius, 1.5 mm, 3 mm, 6 mm and 12 mm in terms of SNR, evaluated at a distance of 1 cm from the coil plane. It can be seen that the highest value of SNR is obtained by the smaller coil, but in a very small region. Moving away from the axis of the coil, the SNR of the smallest coil rapidly decreases and the best SNR is obtained by the second bigger coil, and so on when keeping to move away from the axis. In fact, if the same comparison is made at a higher distance from the coil axis, e.g. 12 cm as shown in figure 4.3b, the best SNR is achieved by the biggest coil. This is even true if the same comparison is made along the axis, at higher distance. In figure 4.3c is reported the SNR evaluated along the axis. As can be seen the smaller coil has the best SNR only close to the coil, and at a distance of 4.5 cm (3 times its size) it already shows the lowest SNR of the four coils. At higher distances, the bigger the coil the best SNR is achieved.

To improve the field of view without modifying the SNR of the coil, it can be used an array of coil. If more than a coil are used simultaneously, every coil has an high SNR over a small region, and the signals received by the coils can be combined together to obtain a high SNR over the entire field of view.

To improve the field of view, two equal coils are used together conveniently posed to get independent signals. In fact, when two coils are close to each other, there is a strong mutual inductance M between them and the magnetic flux density of a coil influences the other in terms of signal received and impedance matching. The maximum mutual inductance occurs when the two coils are both coaxial and coplanar and has a positive value while it becomes negative when the distance between them increases, keeping it coplanar. Hence, there is a suitable spacing for which $M = 0$ and the two coils are decoupled [37]. If this condition is verified, the

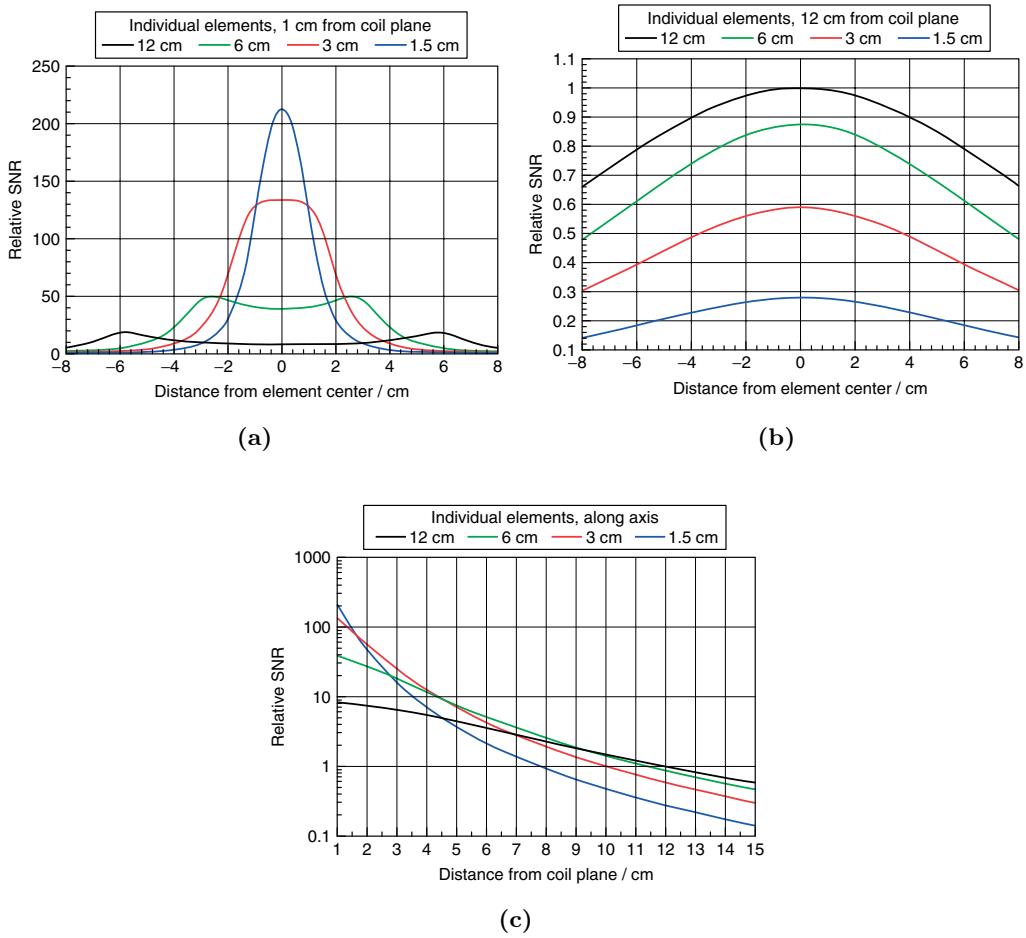

Figure 4.3 Relative SNR comparison of single coil with different radius

matching obtained for the isolated coil remains.

4.6. Results

The double coils have been realized using a conductive tape (width 6 mm) on a thin (flexible) substrate and the final double coil is shown in figure 4.4.

As stated before the coil strongly interacts with the sample under test. Therefore the matching of the coil and the resonant conditions depend on the chosen sample. Besides, the coil will be realized on a flexible substrate to allow the coil to best fit the region to be analyzed, so the curvature of the coil also modify the matching and tuning and needs to take into account in the design.

For these reasons, before starting the design, additional information of the sample are required. Usually, the design is carried out considering as a sample an homo-

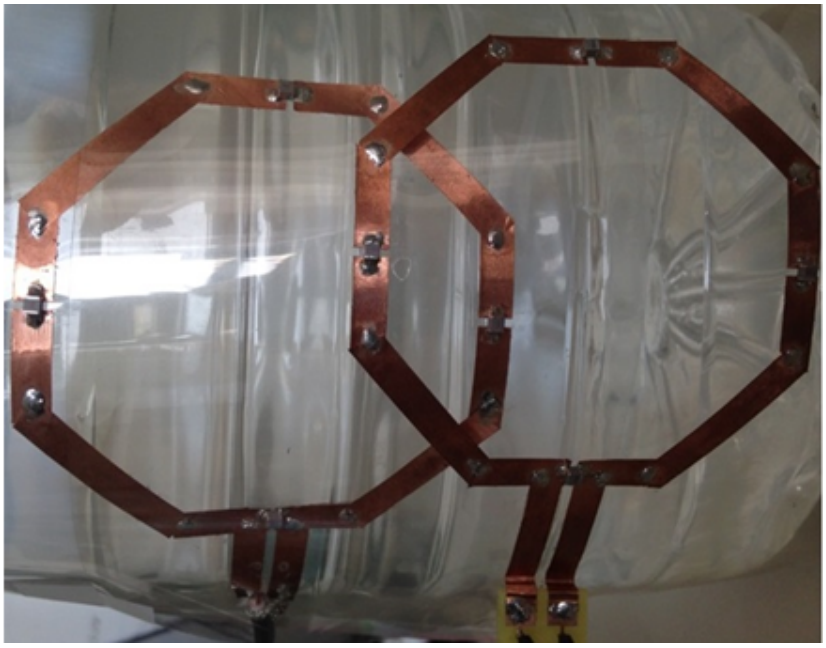

Figure 4.4

Material	Electric conductivity [S/m]	Relative Permittivity	Density [kg/m^3]
Fat	0.0764	11.75	911
Muscle	0.77	58.23	1090
Skin	0.6404	49.90	1109
Cortical bone	0.08249	13.45	1908

Table 4.1 Body tissues properties at 298 MHz [41]

geneous cylinder filled with saline solution. In this work an additional sample is considered, representative of a human thigh or a neck. In particular the two samples used are

- S_1, an homogeneous cylinder with constand dielectric $\epsilon_r = 79 - j41.62$
- S_2, a multilayer cylinder, each layer with dielectric constant of the proper biological tissues. The valuse of the dielectric constants are reported in table 4.1[41]

All test has been done with the flexible dual coil conformal to a cylindrical surface.

On the S1 sample, we first performed, considering the external radius of the sample equal to 6 cm a set of CST simulations and experimental measurements, in order to assess the simulator as viable tools to evaluate the coil behavior in

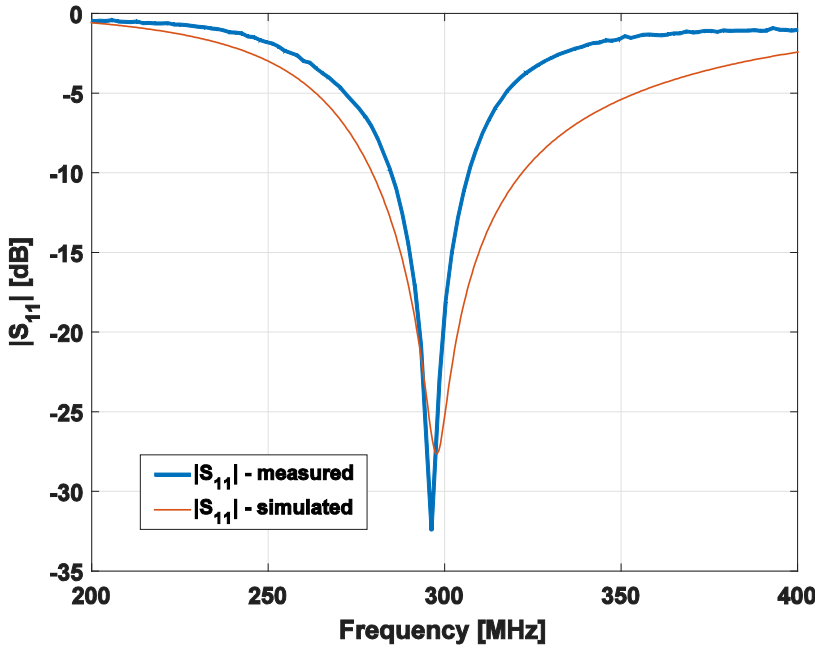

Figure 4.5 Comparison between simulated and measured S_{11}

realistic conditions. The sensor has been loaded at a distance AB=0.5 cm from the sample, and its radius of curvature BC=6 cm. These and all subsequent simulations were performed employing an adaptive mesh, starting with an initial one with a maximum mesh length of 10 mm (i.e., less than 10% of the smallest wavelength in the samples) in every region of the solution domain. The iteration stops when the energy difference is smaller than 5%.

The tuning and matching capacitances have been obtained for a frequency of 298 MHz (corresponding to a static magnetic field $B_0 = 7\,\mathrm{T}$) by the simulator on a single coil as $C_t = 4.9\,\mathrm{pF}$ and $C_m = 3\,\mathrm{pF}$. Then we searched for the optimal spacing between the coils through numerical experimentation, still exploiting simulations, and found the value of 6.75 cm, which corresponds to 0.75 r_{coil}.

The measurements have been performed using a Hewlett Packard, 8720C Vector Network Analyzer, 50 MHz – 20 GHz [42]. The measurement results and the comparison with CST simulations are reported in figure 4.5. It is clear that the agreement is very good. This confirm the accuracy of our simulations, and lead us to conclude that CST is able to deal correctly with the strong interaction between the sensor and the sample, and to model accurately the field inside the sample.

Various simulation have been carried out to study how the geometry of the coil influences the field inside the sample. Using the saline solution sample with radius

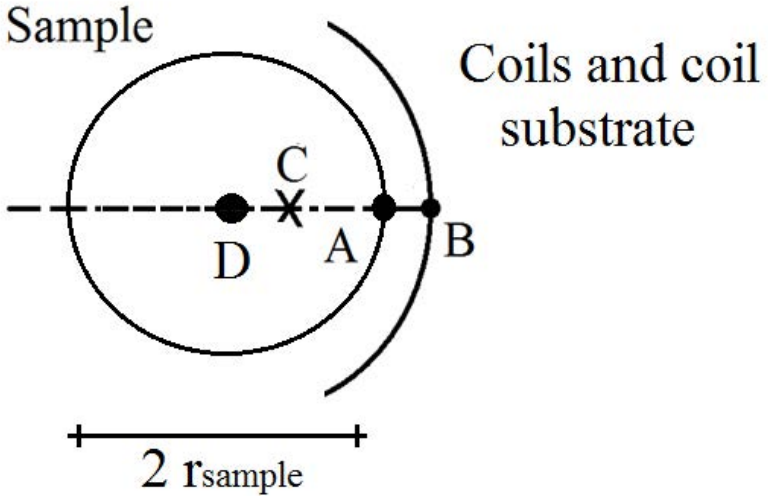

Figure 4.6 Geometry of the coil placed over the sample

|BC|[cm]	**T.C**[pF]	**M.C** [pF]	**R.F.**[MHz]	$\mathbf{S_{11}}$ [dB]	$\mathbf{Z_{11}}$ [Ω]
6	5.4	1.5	297.95	-31.21	$50.43 - j.059$
8	5.6	3.1	297.95	-41.46	$51.28 - j0.74$
10	5.6	4.4	298.1	-36.44	$50.53 - j0.22$

Table 4.2 Used capacitances, S11 and Z11 parameters depending on the different array curvatures. T.C= Tuning Capacitor, M.C= Matching Capacitor, R.F= Resonant Frequency.

of the cylinder $r$sample = 6 cm, three different radii of curvature for the sensor have been tested, namely $|BC| = 6$ cm, 8 cm and 10 cm (see figure 4.6), still at a distance $AD = 6$ cm. For all these values, first the required tuning and matching capacitors have been computed, shown in Table 4.2. For these values, the frequency response of the different coils are shown in 4.7.

Results presented in Table 4.2 show also that an increase of the sensor radius of curvature (i.e, as the sensor becomes flatter), has a marginal effect on the coil inductance (since C_t is almost the same), while the input resistance of the loop varies significantly, requiring a quite large variation of C_m.

The use of an electromagnetic simulator allows to evaluate the field inside the sample, which would be impossible in a real case. Using the electromagnetic field it is possible to evaluate the **S***pecific* **A***bsorption* **R***ate* (SAR), defined as the rate at which electromagnetic energy is absorbed by a biological tissues. It is related to

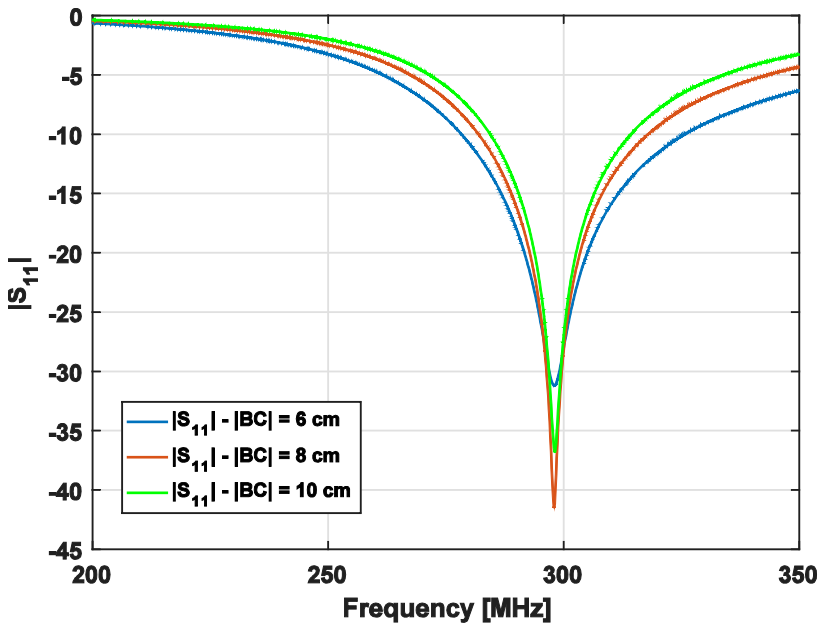

Figure 4.7 Reflection coefficient at the input of both coils of the dual coil sensor for different curvature radii and capacitance values, as reported in Table 4.2

the electric field and the properties of the tissues by the relation

$$SAR = \frac{1}{V}\int_{sample} \frac{\sigma(\vec{\mathbf{r}})\left|\vec{\mathbf{E}}(\vec{\mathbf{r}})\right|^2}{\rho(\vec{\mathbf{r}})} d\vec{\mathbf{r}} \tag{4.6.1}$$

In figure 4.8a and 4.8b present the B_1 magnetic field inside the saline sample and the corresponding SAR. It is clear from these findings that the field uniformity increases and the SAR decreases as the dual coil becomes flatter.

Then we have considered the coil behavior over a set of S2 with four layers (bone, muscle, fat, skin) as in figure 4.9b, modelling an human thigh or neck [43]. The chosen samples have a length of 8.4 cm and a diameter of 12 cm. We have tested coil response over a range of muscle thickness, considering the bone and skin layers constant and adjusting the fat thickness to leave the total diameter unchanged.

The four layer are, starting from the internal one

- bone (εr=13.45 , σ=0.082) with a diameter of 1.2 cm
- muscle (εr=58.23 , σ=0.77)
- fat (εr=11.75 , σ=0.076)
- skin (εr=49.9 , σ=0.64) with a thickness of 0.4 cm

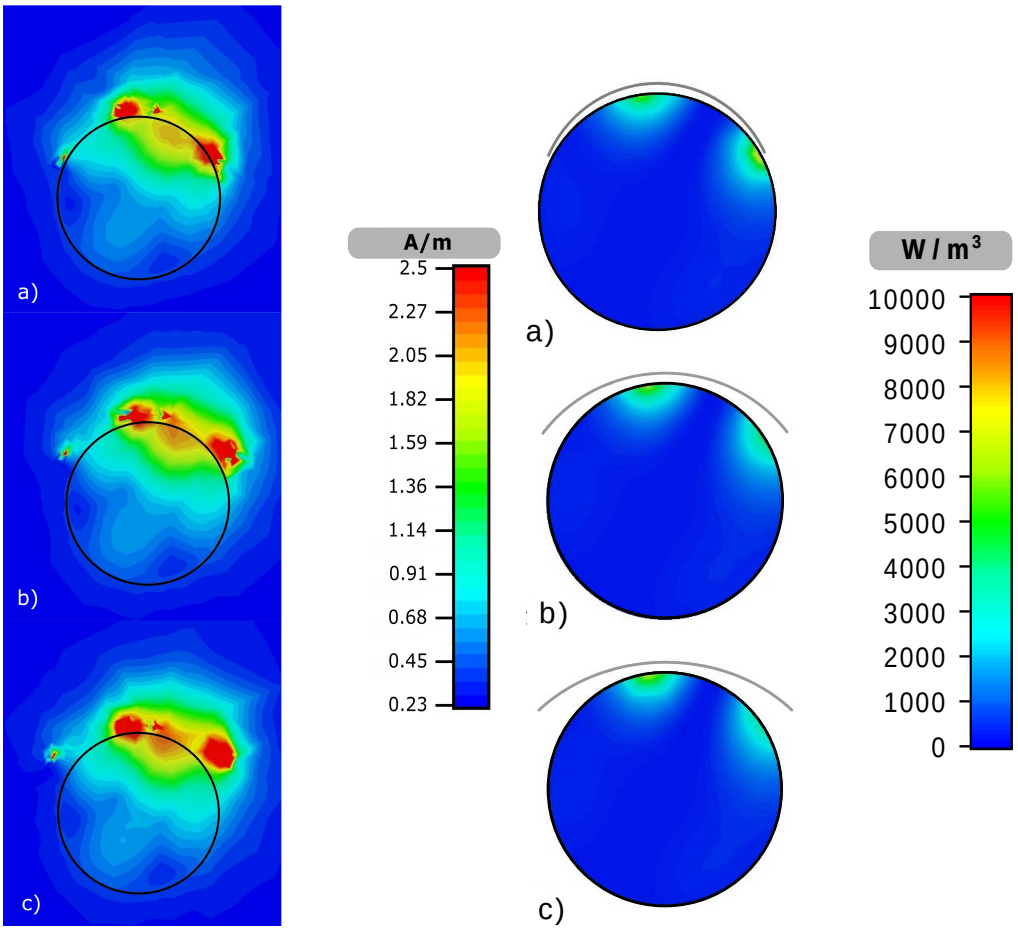

Figure 4.8 B_1 field and SAR using the sample S1 for different curvature radius of the coil

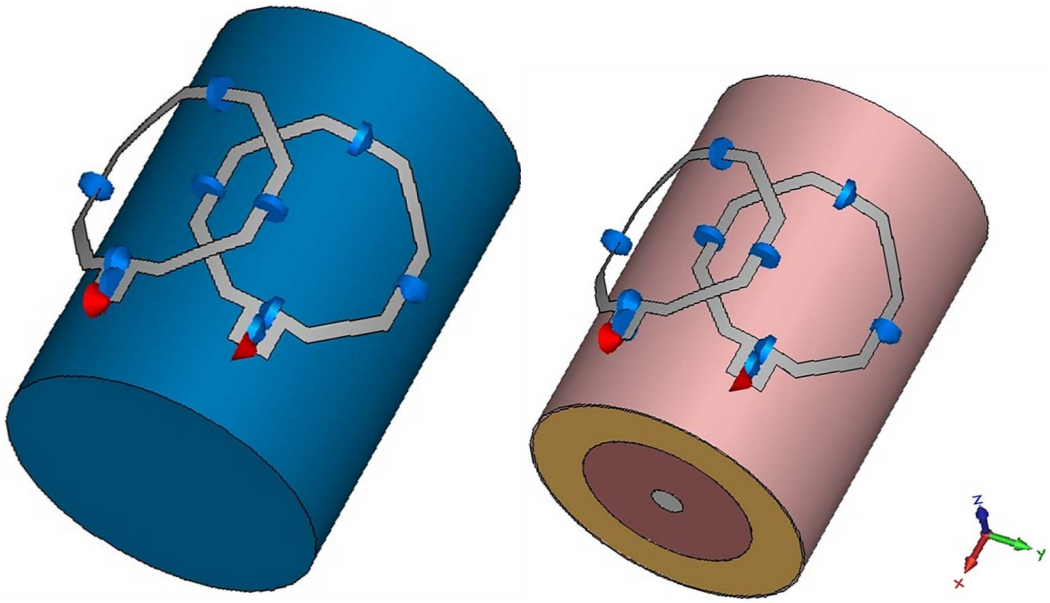

(a) **(b)**

Figure 4.9 The two samples used for the simulations

Muscle thickness has been chosen ranging between 2 cm and 3 cm, while the fat thickness has been chosen so that the total thickness of the muscle and fat layer is equal to 5 cm.

The results of 4.10 show that the muscle (and fat) thickness, has virtually no effect on the resonance frequency, whereas the $|S11|$ decreased from -27 dB (with muscle thickness of 2 cm) to -14 dB with muscle thickness of 3 cm. The B_1 field and the SAR inside the S2 sample are reported in Fig.11 and Fig.12 It is clear that, because of the smaller losses, B_1 field is large and almost uniform in a significant part of the S2 sample.

From figure 4.11a and 4.11b we can compute the maximum *local SAR* [22] which is around 5-6 W/Kg, i.e., smaller than the SAR limit stated in [22], for both cases.

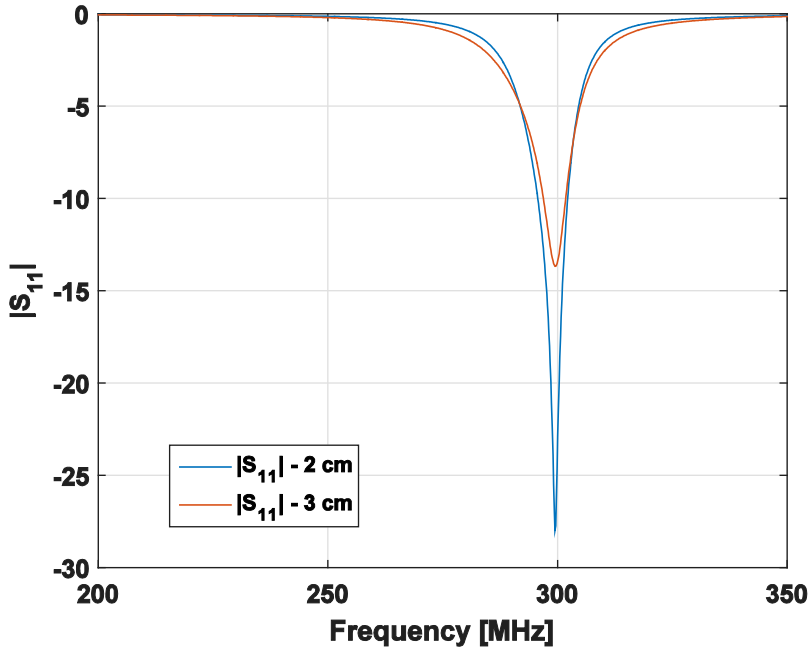

Figure 4.10 |$S11$| parameter of an array coil over a S2 sample with muscle thickness of (blue) 2 cm and (red) 3 cm sample Radius of curvature= 6 cm

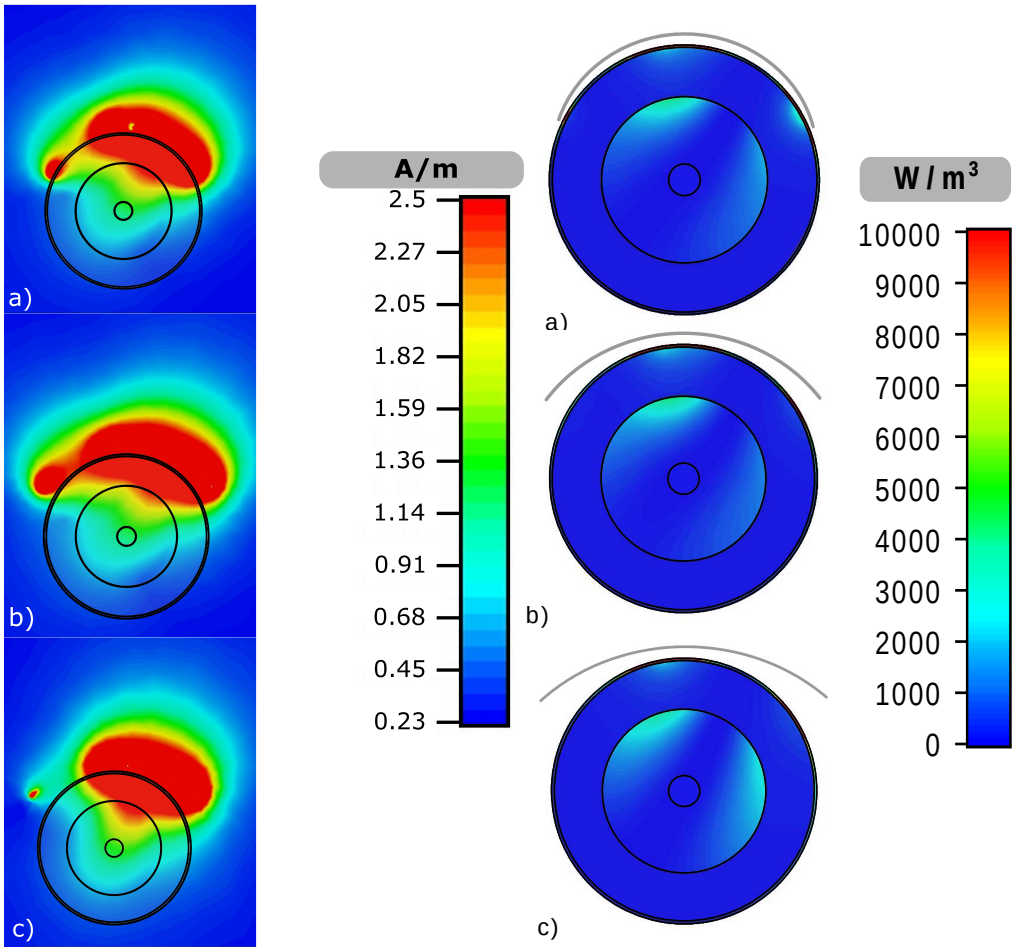

Figure 4.11 B_1 field and SAR using the sample S2 for different curvature radius of the coil

5. Evaluation of electromagnetic field of RFID systems in blood

Healthcare items are one of the most important applications of traceability, since those items must be handled often in emergency conditions and the effects of errors could even be fatal. Among those items, the traceability of blood bags has drawn the greatest amount of attention, since these bags are prepared, stored, and used in different locations, and sometimes in different buildings or even handled by different organizations. The present leading traceability technology is the barcode, but its limitations are well-known. Barcodes require physical contact between the codes and the reader, or at least a very small distance, and good alignment between the two. Moreover, each barcode must be scanned individually. Therefore, a considerable manipulation of the items, or the reader, by an operator is required, and this slows down significantly the operations for large stocks of items [1]. Furthermore, barcodes are subjected to mechanical stresses and external agents, so that they can be easily damaged.

Moreover, blood bags must be complemented with a significant amount of extra information, such as the blood group or the harvest date, which cannot be handled by barcodes, because of the limited amount of information they can store. For these reasons, RFID technology [1] is becoming the leading alternative, as it offers a number of significant advantages [1–5]; however, to become fully effective, this

technology needs a reorganization of the processes [6]. A significant reduction in the reading time can be obtained, e.g., using a portal reader. Nevertheless, its location must be chosen taking into account both the blood movement and the electromagnetic environment. Moreover, these advantages can effectively be exploited only as long as the electromagnetic (EM) field of the RFID reader does not cause any adverse effects on the blood. It is well-known that a strong EM field can heat the blood.

A large heating may even denature the blood, but for smaller temperature increase, some adverse effects can appear, such as the hemolysis of red cells and the modification of blood pH [7], and render the blood useless. Therefore, every use of RFID in blood traceability must assure that no detectable heating occurs during the reading cycle. Despite its interest [3], no standard rules exist at the moment about the use of RFID in blood bag traceability. Only a set of guidelines have been issued by the International Society of Blood Transfusion (ISBT). These guidelines strongly support the use of RFID in the HF band (i.e., at 13.56 MHz) for blood bags [8]. The main reason leading ISBT toward this choice is the quasi-static nature of this field, which is not absorbed by the blood and therefore does not heat the blood itself. Such claims are based on a Food and Drug Administration (FDA) evaluation of the effects of RF on blood cells [9–11], done in 2008. The result of this evaluation was that no heating and no red cell or platelet damages occur during typical HF-RFID reading cycles, not even if higher fields or longer reading times are used. However, HF-RFID advantages come together with some significant and intrinsic technical limitations, namely a reduced reading range and a low channel capacity, which lead to a long reading time. Moreover, multiple tag reading is possible, but not effective enough for the need of large collecting centers. Therefore, a comparison between HF-RFID and UHF-RFID is in order.

The presence of the ISO 18000-3 [12] standard, which defines the specification of the RF interface, and the worldwide availability of the HF-RFID band can be important, but the other features of HF-RFID are quite easily matched by RFID in the UHF band. All the limitations of HF-RFID can be overcome by UHF-RFID [13]; hence, this trade-off would be clearly in favor of UHF-RFID, as long as it does not cause detectable heating of the blood during a reading cycle. No systematic study on the effect of UHF electromagnetic fields on the blood has been performed. Only a few experimental data have been collected [14] by exposing blood bags to the field of a portal reader for a time longer than a typical reading cycle. After all the exposures, no significant variation of the biological indexes (pH levels, platelet (PLT) count, and PLT aggregation rate) was found. The effect on

the blood temperature has not been recorded. Therefore, the only data available have been obtained by a numerical simulation [15].

However, the setups chosen in [15], i.e., a few cylindrical tubes filled with blood plasma, exposed in a waveguide, or located in close proximity of a coil, are completely different from the actual reader field and bag shape, so the aim of this paper is to numerically evaluate the increase in temperature and the specific absorption rate (SAR) of a blood bag with a realistic shape, when exposed to a field very close to a typical UHF reader field, in order to assess, at least from this point of view, the use of UHF-RFID in blood bags traceability.

5.1. Materials and Methods

For the problem at hand, a discussion on the UHF-RFID readers is now in order. Broadly speaking, commercial readers can be grouped into two categories: hand-held readers and portal readers. Portal readers can accommodate reader antennas up to 1 m, which is an improvement compared with hand-help readers whose antennas size is around 10–15 cm. Portal readers also have a larger reading range and a relatively smaller reading area. For UHF-RFID, the wavelength $\lambda = 34.6$ cm; therefore, the antenna, whose size is a few wavelengths, has a directive gain large enough to reduce the risk of electromagnetic interferences, both active and passive [16].

For both kinds of readers, however, the bottleneck for the reading range is the reader power [2]. This power must fulfill national regulations limits on the so-called effective radiated power [17]:

$$\mathrm{ERP} = G_T \cdot P_T \tag{5.1.1}$$

where G_T is the product of the reader antenna's gain, and P_T is the reader power. In Europe, this limit is $ERP \leqslant 2\,\mathrm{W}$ [18]. Therefore, a large reader antenna allowed by a portal reader, which has a larger G_T, calls for a smaller P_T, with no benefit for the reading range (but, of course, with a smaller field outside the reading region).

The field distribution of the reader antenna in the reading region depends essentially on the distance between it and the reader [19]. Outside a sphere whose radius is around 4–5 λ (i.e., 1.4–1.8 m) for an hand-held reader antenna and around 10 λ (i.e., 3.5 m) for a portal reader antenna, there is the antenna far field and a field that behaves like a spherical wave, with a dependence on the distance source-field point r. Now, such a spherical wave can be well approximated by a plane wave in every region whose radial depth is less than $r/10$. Since the bag is quite small (less

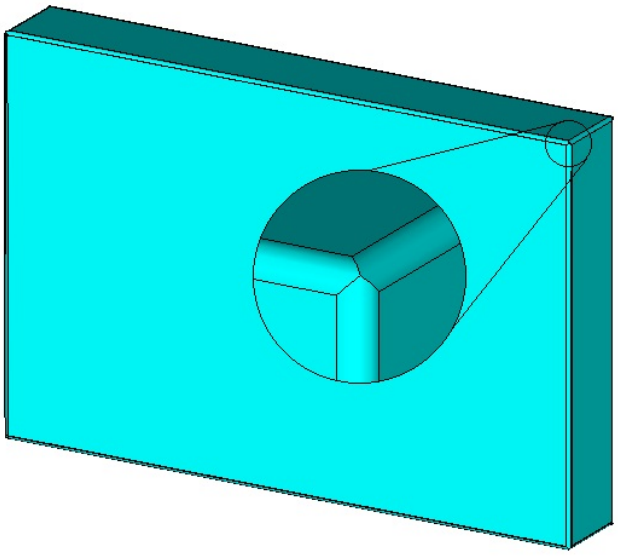

Figure 5.1 Blood bag parallelepiped rounded wedges.

than $\frac{\lambda}{2}$), we can use the plane-wave approximation when the bag is in the antenna far-field. The amplitude of the plane-wave is equal to

$$E_{\mathrm{MAX}} = 7.75 \cdot \frac{\sqrt{G_T \cdot P_T}}{r} [\mathrm{V/m}] \tag{5.1.2}$$

where r is the (average) reader-bag distance, and E_{MAX} is the maximum of the sinusoidal electric field.

When the bag is not in the reader far-field, the antenna field has a far stronger spatial variation, both with the radial distance (since the dominant term is now proportional to $1/r^3$) and with the angular position. The details of this variation are strongly dependent on the antenna, but all the actual main features of the field are shared by a simple half-wavelength dipole field, with the same ERP as the actual antenna.

The blood bag has been modeled to mimic an actual (filled) bag, namely as a thin rectangular envelope (with a thickness equal to 100 µm) of PVC, whose dimensions (see figure 5.1) have the typical values of an actual filled bag: $a = 17\,\mathrm{cm}$, $b = 11.3\,\mathrm{cm}$, and $c = 2.7\,\mathrm{cm}$ [20].

As apparent from figure 5.1, the lateral wedges have been rounded, with a curvature radius of 1 mm to better conform to the actual bag shape.

Inside the bag, we put a dielectric material with the same (temperature-dependent) dielectric constant of the blood [21]. This bag was exposed with a plane-wave linearly polarized along the a–side of the bag, and traveling in a direction normal to

the bag face, and to the field of a half-wavelength dipole, lying parallel to the a-side of the bag at the bag center. The dipole-bag distance was set to 5 cm, 10 cm, and 15 cm.

The numerical simulations were done using CST Studio Suite (CST Microwave Studio and CST Multiphysics Studio) [22]. This software is based on the finite integration technique (FIT) [23], a differential technique which, unlike other, equally popular, differential techniques, solves an exact set of equations between averaged fields and therefore is conceptually suited to our scope since all compliance regulations use averaged field values [24]. As a by-product, the FIT allows for the obtainment of the charge and energy conservation in an exact way at no cost. The main approximation required by the FIT is on the constitutive relations, which are local ones and must be approximated by relations between spatially averaged (i.e., integrated on small volumes) fields.

To perform all CST simulations, the bag was placed at the origin of the CST coordinate system and was surrounded by an air box, which extended 1 m from every side of the bag. On the box's faces, the "open (add space)" boundary conditions were set. This corresponds to the perfectly matched layer conditions [25]. Two types of CST sources were used. The first one is a plane wave, set to impinge orthogonally to the bag. The second one is a discrete port, set as S-parameter type, as a feed for the dipole.

The *time domain solver* was used and set up with the adaptive mesh feature.

Since the FIT is a differential technique, it gives the field distribution (in fact, the distribution of a field spatially-averaged over cells smaller than $\lambda/20$) in the whole domain of interest. We present in the following section two types of data (for all considered cases):

- field distribution along a straight line, orthogonal to the bag face, crossing the bag
- the local SAR in the whole bag

The latter data was then used to evaluate the time required to increase the bag temperature of 0.1 °C. Because of the convective motion inside the bag (and because the electric field varies slowly there), we computed the temperature increase using the maximum value of the SAR, which is clearly the worst case. It is worth noting that, as we will show later, this time is far larger than a typical reading cycle (which lasts a few tens of seconds).

#	X (mm)	Y (mm)
1	0	0
2	84.11	55.51
2	80	10
2	10	50
2	95	0
2	0	60

Table 5.1 Segment Position

5.2. Results and Discussion

We report here the effect of a reader's field on a blood bag, under various exposure conditions covering all the cases in the "production" environment.

Portal readers use moderate-gain antennas but the bag is located below the portal at several wavelengths from the reader (a wavelength $\lambda = 34.6\,\text{cm}$ at 867 MHz), so their field is a linearly polarized plane wave when evaluated on and around the bag. Therefore, we simulated this reader's field as a plane wave traveling downward and then impinging normally on the side of a flat bag, with a maximum amplitude of $50\,\text{V/m}$ (corresponding to a power density of $3.3\,\text{W/m}$). Portable readers have a small gain antenna and usually works in near field. Their field has been simulated by a single half-wavelength dipole, radiating 1 W and located close to the bag. The bag has been simulated with a box whose size is $17 \times 11.3 \times 2.7\ \text{cm}^3$, with rounded wedges and an enclosure of PVC of 100 µm.

The box is filled with a lossy dielectric with $\epsilon_r = 61 - j33$ equal to the typical dielectric constant of actual blood [26]. The field was sampled on six segments (labeled from 1 to 6) crossing the bag normally and extending 50 cm on both sides. Their transverse position (and labeling) is shown in figure 5.2 and table 5.1. The field on these segments is shown in figures 5.3 to 5.8 for different expositions, where the zero of the x-axis is set to the starting point of the segment. In each figure, we report on the field computed on these segments, and the different graphs are labeled with the segment number.

The plane wave field clearly shows (figures 5.3 and 5.4), on each curve, the interference between the incident and reflected field before the bag, and a steady return to the incident (i.e., unperturbed) value beyond the bag. The main difference between the curves is the strong peak along the upper wedge. The incident field is polarized orthogonally to this wedge; therefore, from the Meixner's condition [27], we should expect a singular field here just outside the blood bag. This is the reason

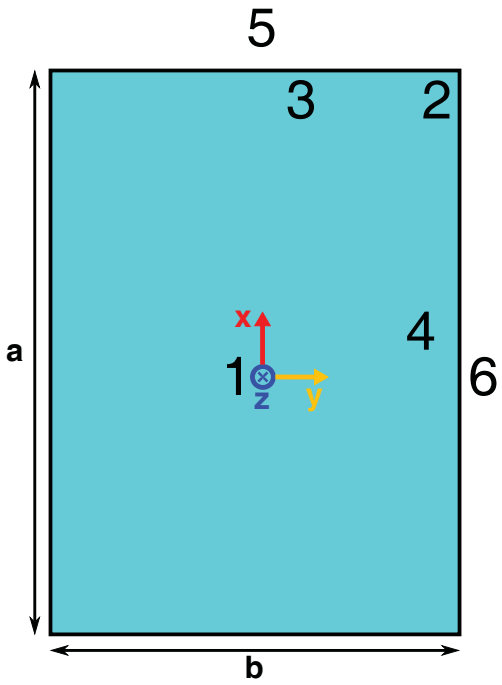

Figure 5.2 Position of the test lines into the bag. Exact positions are reported in Table 1

for the strong field in the air (up to 3 times the incident one) in figure 5.4, while no such effect is on Curves 5 and 7 of figure 5.3, where the incident field is polarized along the wedge [27]. In every case, the field inside the bag is quite small (figure 5.5), with an average value of around 30% of the incident value and a peak of 50 V/m (equal to the incident one) at the bag angle. This is easily explained, since the blood has a small wave impedance [19] and thus acts as a screen.

This effect is present also in the (vertical) dipole field, with a reduced field value both inside the blood and beyond the bag, when compared with the field without the bag. To save space, we show here (figures 5.6 and 5.7) only the field for a dipole located at 15 cm from the bag, but the plots are essentially the same (but for the maximum value) at different distances. The same behavior is shown also in figure 5.8, together with the singular behavior just outside the horizontal wedges (which are orthogonal to the dipole fields), reaching 80 V/m.

The (relatively) small field value in the bag leads to a small SAR value. The SAR distribution in the two cases considered here is shown in figure 5.9a (plane wave) and figure 5.9b (close dipole field). From them, it follows that a plane wave with an incident power density of 3.3 W/m^2 causes a SAR smaller than 0.75 W/kg, while the SAR produced by a 1 W dipole located at 15 cm is no larger than 1 W/kg. However, a closer look at the SAR distribution in figures 5.9a and 5.9b reveals that

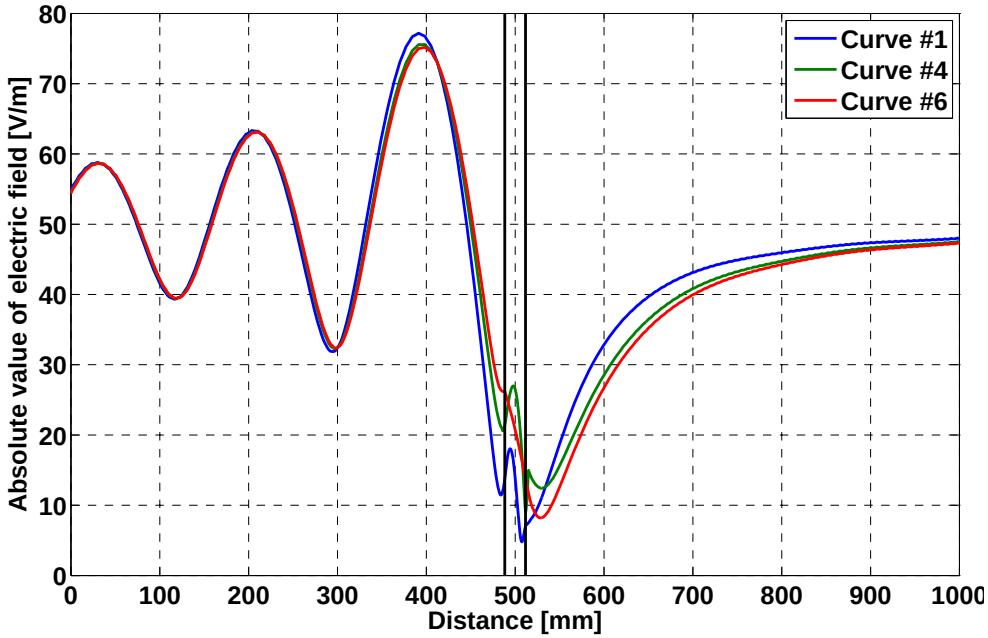

Figure 5.3 Plane wave field inside and around the bag. The curve number refers to the segments in figure 5.2

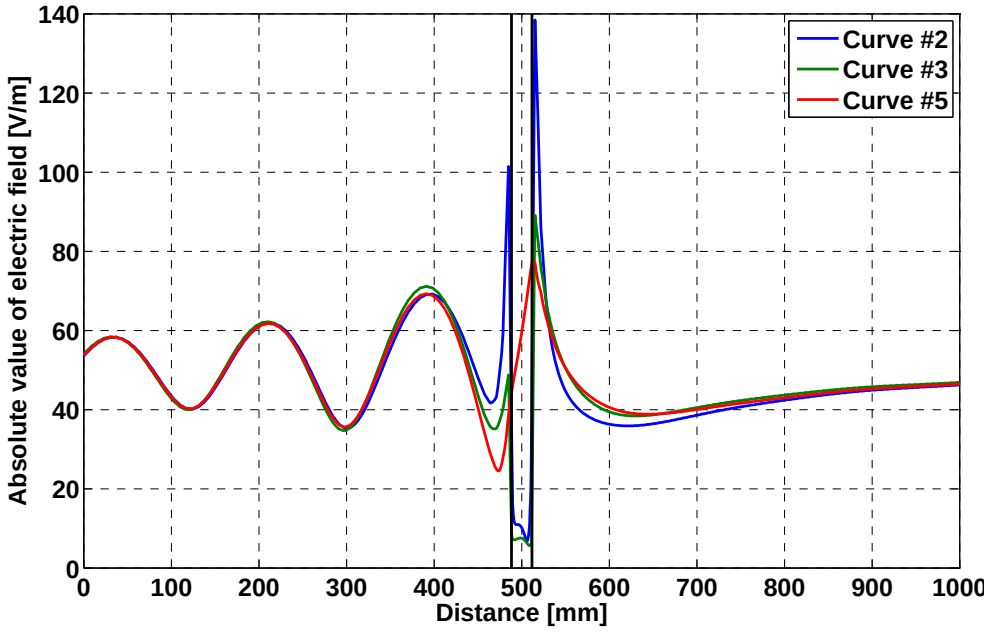

Figure 5.4 Plane wave field inside and around the bag. The curve number refers to the segments in figure 5.2

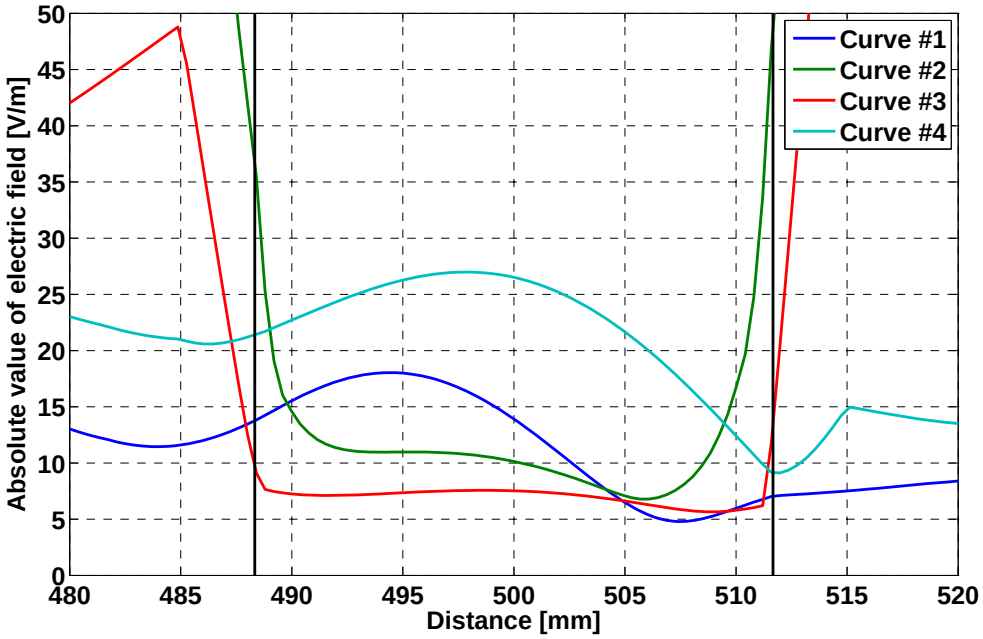

Figure 5.5 Expanded view of the field inside the bag, for plane wave incidence. The curve number refers to the segments in figure 5.2

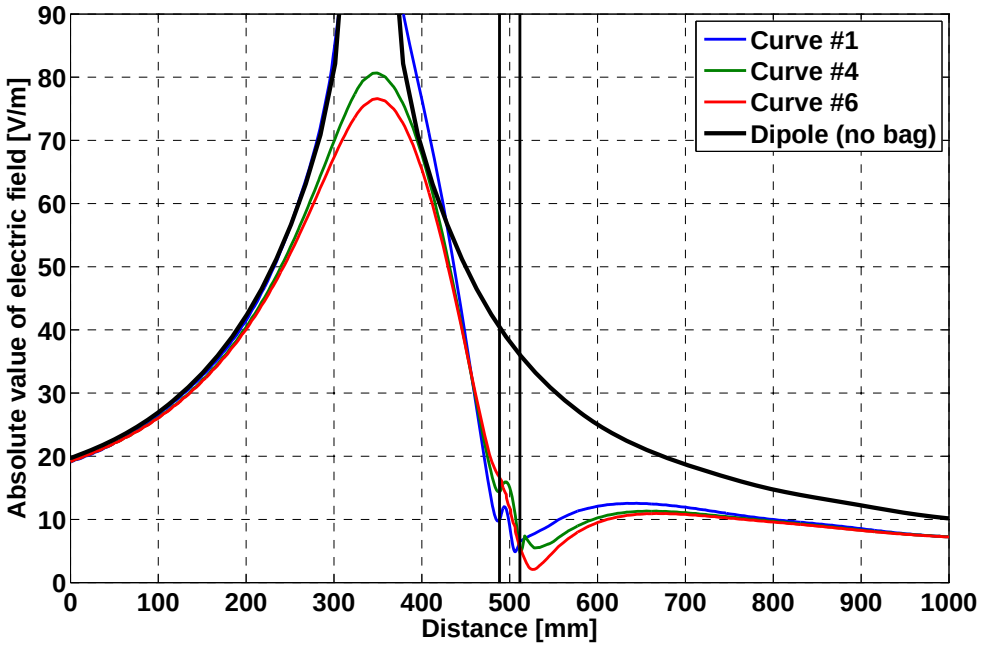

Figure 5.6 Field due to a dipole located at 15 cm from the bag side. The curve number refers to the segments in figure 5.2. The curve labeled "Dipole (no bag)" shows, for comparison, the free-space dipole field comparison.

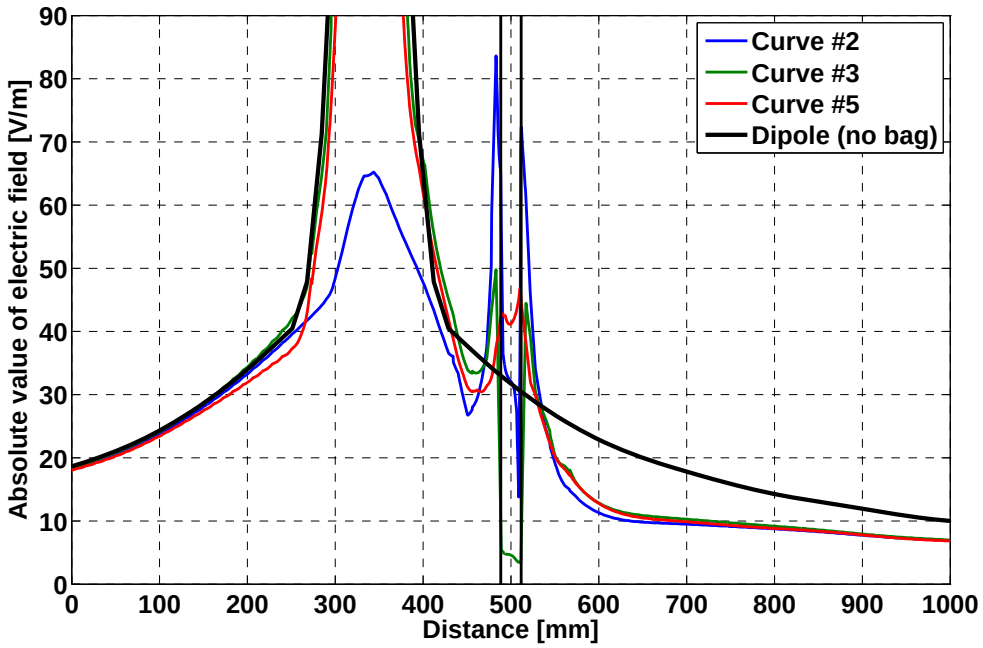

Figure 5.7 Field due to a dipole located at 15 cm from the bag side. The curve number refers to the segments in figure 5.2. The curve labeled "Dipole (no bag)" shows, for comparison, the free-space dipole field comparison.

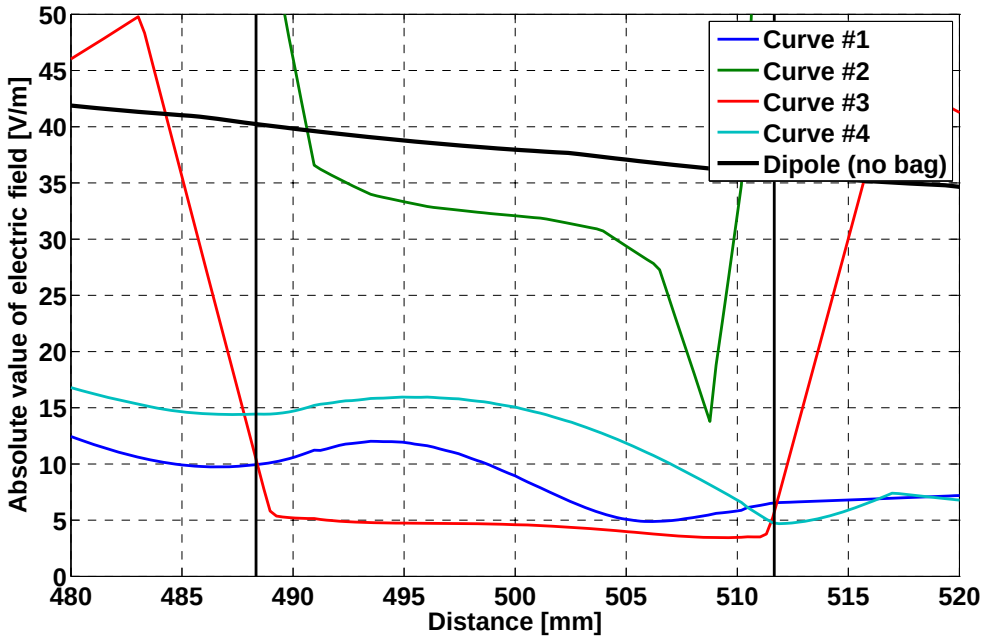

Figure 5.8 Expanded view of the field inside the bag, due to a dipole located at 15 cm from the bag side. The curve number refers to the segments in figure 5.2. The curve labeled "Dipole (no bag)" shows,for comparison, the free-space dipole field comparison.

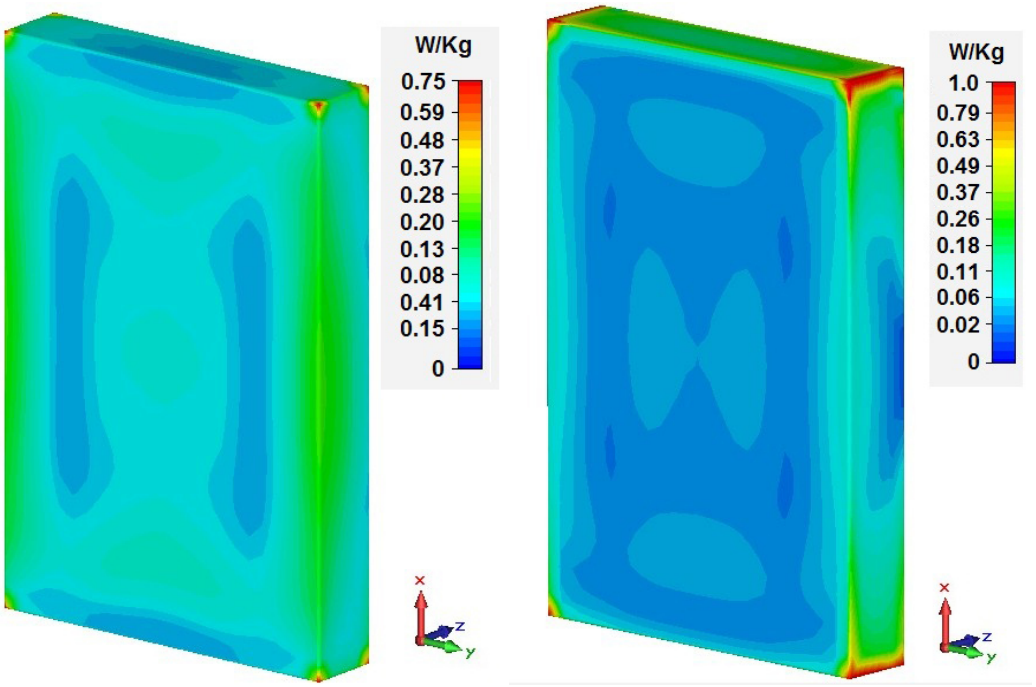

(a) SAR distribution for plane wave at the frequency of 867 MHz on blood bag parallelepiped rounded wedges.

(b) SAR distribution for close dipole at the frequency of 867 MHz on blood bag parallelepiped rounded wedges.

Figure 5.9

the SAR distribution has narrow peaks at the bag boundary, while the SAR value in the bulk of the bag is significantly lower, around 20%–40% of the peak.

The order of magnitude of these SAR values can be compared with the ICNIRP guidelines [24] for the exposures of the general population. They state that we are protected against known adverse health effects as long as the localized SAR is smaller than 2 W/kg. Such a value is larger than the SAR developed in our bag under test, so we can reliably assume that no adverse effects are caused in the blood by the field we have considered here.

As a final test, we also evaluated the time ΔT needed to raise the blood temperature by 0.1 °C, which is shown in table 5.2 for a dipole at different distances. ΔT is of the order of 10–60 min (depending on the distance dipole-bag). Therefore, after a reading sequence lasting less than one minute, no temperature increase can be registered.

Distance betweend Blood Bag and Dipole (cm)	**SAR (W/kg)**	**ΔT (min) for Increases the Temperature of the Blood around** 0.1 °C
5	0.44	16
10	0.11	62
15	<0.01	-

Table 5.2 Time ΔT needed to raise the temperature of the blood in the bag by 0.1 °C

Conclusions

In this thesis different applications of microwaves have been proposed, outside of the telecommunication field. A general method for the design of the procedure or the device have been described and one or more special cases have been analyzed.

Soil disinfection by means of high power microwaves irradiation requires the knowledge of the physical parameters of the soil and its humidity, which can be obtained by measurements. A numerical model to determine the temperature profile in the soil has been developed and used to provide a procedure to keep the critical temperature (related to the bacteria objective of the disinfection) for the desired amount of time required for the disinfection. The model can be easily adapted to different cultivation styles.

The use of a microwave resonant cavity as a controlled environment for a chemical reaction in an aqueous solution is proposed which allows to control the temperature of the solution and to optimize the effectiveness of the enzyme and then the yield of the reaction. The optimal parameters to set up the apparatus for the rection in use can be obtained. Not least, the designed cavity for a given reaction can be used as a tool to study the influence of the electromagnetic field to the kinetic parameters of the reaction, for a better understanding of the non-thermal effects due to the field.

An RF surface coil is designed to be used for magnetic resonance imaging. The coil has been designed and realized on a flexible substrate for an optimal adaption to the body part to be analyzed. This allows to achieve a higher penetration depth and an improved SNR. The use of an array of coils, conveniently designed to reduce the coupling between them, allowed to cover a wider area with the same performances of a single coil (thanks to the decoupling).

Finally, the numerical analysis of the electromagnetic field inside a full blood bag due to sources equivalent to an RFID reader has shown low values of field even for a continuous exposition (worst case) suggesting that the blood will not be degraded by the radiation and RFID technology will not be harmful for this application. An in-vitro study is required to confirm the numerical results.

Bibliography

Chapter 1

[1] F. T. Ulaby, E. Michielssen, and U. Ravaioli. *Fundamentals of Applied Electromagnetics, 6 ed.* 2010.

[2] M.-H. Carpentier B. L. Smith. *The Microwave Engineering Handbook, Vol. 3, Microwave systems and applications*. 1993.

[3] International Telecommunication Union. "Article 1.15, definition: Industrial, scientific and medical (ISM) applications (of radio frequency energy) / ISM application". In: *ITU Radio Regulations, Section IV. Radio Stations and Systems* ().

[4] R.J. Meredith A.C. Metaxas. *Industrial Microwave Heating*. 2008.

Chapter 2

[1] A. S. Komarova, A. A. Likhacheva, and D. G. Zvyagintsev. "Influence of microwave radiation on soil bacteria". In: *Mosc. Univ. Soil Sci. Bull., vol. 63* (2008).

[2] M. A. Oliver and P. J. Gregory. "Soil, food security and human health: A review". In: *Eur. J. Soil Sci., vol. 66, no. 2* (2015).

[3] E. Mitscherlich and E. H. Marth. *Microbial Survival in the Environment – Bacteria and Rickettsiae Important in Human and Animal Health*. 1984.

[4] A. G. Gao et al. "Fungal pathogen protection in potato by expression of a plant defensin peptide". In: *Nature Biotechnol., vol. 18, no. 12* (2010).

[5] J. Bezchlebova, J. Cernohlavkova, J. Lana, I. Sochova, K. Kobeticova, and J. Hofman. "Effects of toxaphene on soil organisms". In: *Ecotoxicol. Environ Saf., vol. 68, no. 3* (2007).

[6] M. Margni, D. Rossier, P. Crettaz, and O. Jolliet. "Life cycle impact assessment of pesticides on human health and ecosystems". In: *Agric. Ecosyst. Environ., vol. 93, no. 1* (2002).

[7] C. Bonaventura and F. M. Johnson. "Healthy environments for healthy people: Bioremediation today and tomorrow". In: *Environ. Health Perspect., vol. 105, no. 1* (1997).

[8] J. J. Obryck, J. D. Harwood, T. J. Kring, and R. J. O'Neil. "Aphidophagy by coccinellidae: Application of biological control in agroecosystems". In: *Biol. Control, vol. 51, no. 2* (2009).

[9] W. Devliegher and W. Verstraete. "The effect of lumbricus terrestris on soil in relation to plant growth: Effects of nutrient-enrichment processes (NEP) and gut-associated processes (GAP)". In: *Soil Biol. Biochem., vol. 29, no. 3* (1997).

[10] G. R. Vela, J. F. Wu, and D. Smith. "Effect of 2450 MHz microwave radiation on some soil microorganisms in situ". In: *Soil Sci., vol. 121* (1976).

[11] G. R. Vela and J. F. Wu. "Mechanism of lethal action of 2.450 MHz radiation on microorganisms". In: *Appl. Environ. Microbiol., vol. 37* (1979).

[12] Ulaby FT, Batlivala PP, and Dobson MC. "Microwave backscatter dependence on surface roughness, soil moisture, and soil texture: part I-bare soil". In: *IEEE Trans Geosci Electron* (1978).

[13] Ulaby FT, Moore RK, and Fung AK. *Microwave remote sensing: active and passive*. 1982.

[14] Ulaby FT, Moore RK, and Fung AK. "Microwave remote sensing: active and passive". In: *In: IEEE Transactions on Geoscience Electronics. Vol. 3* (1986).

[15] Baghdadi N, Zribi M, Loumagne C, et al. "Analysis of TerraSAR-X data and their sensitivity to soil surface parameters over bare agricultural field". In: *Remote Sens Environ* (2008).

[16] Das K and Paul PK. "Present status of soil moisture estimation by microwave remote sensing". In: *Cogent Geosci.* (2015).

[17] Hallikainen MT, Dobson MC, Ulaby FT, et al. "Microwave dielectric behavior of wet soil-part 1: empirical models and experimental observations". In: *IEEE Trans Geosci. Remote Sens.* (1985).

[18] Valbonesi S and Bisceglia B. "EMF application to soil disinfestation and agro-food processing for a sustainable development". In: *Proceedings of the 15th IEEE Mediterranean Microwave Symposium* (2015).

[19] Helszajn J. *Ridge waveguides and passive microwave components*. 2000.

[20] Wang JR and Schmugge TJ. "An empirical model for the complex dielectric permettivity of soils as a function of water content". In: *IEEE Trans Geosci Remote Sens.* (1978).

[21] Fung AK. *Microwave scattering and emission models and their applications.* 1994.

[22] Guattari C, Ramaccia D, Bilotti F, and others. "Permittivity of sub-soil materials retrieved through transmission line model and GPR data". In: *Prog Electromagn Res.* (2015).

[23] M. C. Dobson, F. T. Ulaby, M. T. Hallikainen, and M. A. El-Rayes. "Microwave dielectric behavior of wet soil – Part II: Dielectric mixing models". In: *IEEE Trans. Geosci. Remote Sens.* (1985).

[24] P. S. Ray. "Broadband complex refractive indices of ice and water". In: *Applied Optics* (1972).

[25] Vian A, Davies E, Gendraud M, et al. "Plant responses to high frequency electromagnetic fields". In: *BioMed Res Int.* (2016).

[26] Du RY, Wen D, Zhao PH, et al. "Effect of bacterial application on metal availability and plant growth in farmland-contaminated soils". In: *J Bioremed Biodeg.* (2016).

[27] Coppola A, Basile A, Menenti M, et al. "Spatial distribution and structure of remotely sensed surface water content estimated by a thermal inertia approach". In: *IAHS-AISH Publ.* (2007).

[28] Incropera, DeWitt, Bergman, and Lavine. *Fundamentals of Heat and mass Transfer.* 2006.

[29] J.H. Lienhard V and J.H. Lienhard IV. *A Heat Transfer Textbook.* 2011.

[30] A. Cengel Yunus and A. Boles Michael. *Thermodynamics.* 2001.

[31] A.C. Metaxas and Meredith RJ. *Industrial Microwave Heating.* 2008.

[32] Scheid F. *Schaum's Outline of Numerical Analysis.* 1968.

[33] Montaldo N, Albertson JD, and Mancini M. "Vegetation dynamics and soil water balance in a waterlimited Mediterranean ecosystem on Sardinia, Italy". In: *Hydrol Earth Syst Sci Discuss.* (2008).

[34] Montaldo N, Corona R, and Albertson JD. "On the separate effects of soil and land cover on Mediterranean ecohydrology: two contrasting case studies in Sardinia, Italy". In: *Water Resour Res.* (2013).

[35] E. Shlevin, I. S. Saguy, Y. Mahrer, and J. Katan. "Modeling the survival of two soilborne pathogens under dry structural solarisation". In: *Phytopathology* (2003).

[36] Wadell C. *Transmission Line Design Handbook*. 1991.

Chapter 3

[1] K. R. Foster. "Thermal and nonthermal mechanisms of interaction of radio-frequency energy with biological systems". In: *IEEE Trans. Plasma Sci., 28* (2000).

[2] O. P. Gandhi, G. Lazzi, and C. M. Furse. "Electromagnetic absorption in the human head and neck for mobile telephones at 835 and 1900 MHz". In: *IEEE Trans. Microwave Theory Tech., 44* (1996).

[3] H. Akiyama, T. Sakugawa, T. Namihira, K. Takaki, Y. Minamitani, and N. Shimomura. "Industrial applications of pulsed power technology". In: *IEEE Trans. Dielectr. Electr. Insul., 14* (2007).

[4] K. Rawal, M. K. Mishra, M. Dixit, and M. Srinivasarao. "Microwave assisted solvent free synthesis of α-α'-bis (arylidene) cycloalkanones by sulfated zirconia catalyzed cross aldol condensation of aromatic aldehydes and cycloalkanones". In: *J. Ind. Eng. Chem., 18* (2012).

[5] F. Monteil-Rivera and L. Paquet. "Solvent-free catalyst-free microwave-assisted acylation of lignin". In: *Ind. Crops Prod., 65* (2015).

[6] G. Keglevich, E. Bálint, Ė. Karsai, A. Grün, M. Bálint, and I. Greiner. "Chemoselectivity in the microwave-assisted solvent-free solid-liquid phase benzylation of phenols: O- versus C-alkylation". In: *Tetrahedron Lett., 49* (2008).

[7] X. Guo, D. Han, H. Xi, L. Rao, X. Liao, X. Hu, and J. Wu. "Extraction of pectin from novel orange peel assisted by ultra-high pressure, microwave or traditional heating: A comparison". In: *Carbohydr. Polym., 88* (2012).

[8] R. Carta and F. Desogus. "The effect of low-power microwaves on the growth of bacterial populations in a plug flow reactor". In: *AIChE J., 56* (2010).

[9] R. Carta and F. Desogus. "Possible non-thermal microwave effects on the growth rate of Pseudomonas aeruginosa and Staphylococcus aureus". In: *Int. Rev. Chem. Eng., 4(4)* (2012).

[10] R. Carta and F. Desogus. "The enhancing effect of low power microwaves on phenol oxidation by the Fenton process". In: *J. Environ. Chem. Eng., 1* (2013).

[11] R. Carta, F. Desogus, and M. Errico. "Effect of microwave radiation on the growth rate of Bacillus clausii at 37°C". In: *17th International Congress of Chemical and Process Engineering, CHISA, Prague, Czech Republic* (2006).

[12] A. Shazman, S. Mizrahi, U. Cogan, and E. Shimoni. "Examining for possible non-thermal effects during heating in a microwave oven". In: *Food Chem., 103* (2007).

[13] F. Zuo, A. Badev, S. Saunier, D. Goeuriot, R. Heuguet, and S. Marinel. "Microwave versus conventional sintering: Estimate of the apparent activation energy for densification of α-alumina and zinc oxide". In: *J. Eur. Ceram. Soc., 34* (2014).

[14] G. Gong, D. Liu, and Y. Huang. "Microwave-assisted organic acid pretreatment for enzymatic hydrolysis of rice straw". In: *Biosystems Eng., 107* (2010).

[15] D. Yu, H. Wu, A. Zhang, L. Tian, L. Liu, C. Wang, and X. Fang. "Microwave irradiation-assisted isomerization of glucose to fructose by immobilized glucose isomerase". In: *Process Biochem., 46* (2011).

[16] A. K. Anderson and H. S. Guraya. "Effects of microwave heat-moisture treatment on properties of waxy and non-waxy rice starches". In: *Food Chem., 97* (2006).

[17] P. C. Molgero Da Rós, W. Costa e Silva, D. Grabauskas, V. H. Perez, and H. Ferreira de Castro. "Biodiesel from babassu oil: Characterization of the product obtained by enzymatic route accelerated by microwave irradiation". In: *Ind. Crops Prod., 52* (2014).

[18] M. R. Avhad and J. M. Marchetti. "A review on recent advancement in catalytic materials for biodiesel production". In: *Renewable Sustainable Energy Rev., 50* (2015).

[19] David M. Pozar. *Microwave Engineering, 4ed.* 2012.

[20] R. F. Harrington. *Time-Harmonic Electromagnetic Fields.* 1961.

[21] E. W. Lemmon, M. O. McLinden, and D. G. Friend. "Thermophysical properties of fluid systems". In: *NIST Chemistry WebBook, NIST Standard Reference Database Number 69* (2016).

[22] P. Vrábel, M. Polakovic, V. Stefuca, and V. Báleš. "Analysis of mechanism and kinetics of thermal inactivation of enzymes: Evaluation of multitemperature data applied to inactivation of yeast invertase". In: *Enzyme Microb. Technol., 20* (1997).

[23] L. Michaelis and M. L. Menten. "Die kinetik der invertinwirkung". In: *Biochemische Zeitschrift, 49,* (1913).

[24] H. Besserdich, E. Kahrig, R. Krenz, and D. Kirstein. "Kinetische untersuchungen zur substratüberschuss-hemmung gelöster und trägerficierter invertase". In: *J. Mol. Catal., 2* (1977).

[25] R. M. Daniel and M. J. Danson. "Temperature and the catalytic activity of enzymes: A fresh understanding". In: *FEBS Lett., 587* (2013).

[26] J. Vásquez-Bahena, M. C. Montes-Horcasitas, J. Ortega-López, I. Magaña-Plaza, and L. B. Flores-Cotera. "Multiple steady states in a continuous stirred tank reactor: An experimental case study for hydrolysis of sucrose by invertase". In: *Process Biochem., 39* (2004).

[27] Ajit Sadana. "Enzyme Deactivation". In: *Biotech. Adv. Vol. 6* (1988).

Chapter 4

[1] G. Liney. "MRI in Clinical Practice". In: (2006).

[2] V. Kuperman. *Magnetic Resonance Imaging: Physical Principles and Applications.* 2000.

[3] J. Jin. *Electromagnetic Analysis and Design in Magnetic Resonance Imaging.* 1998.

[4] P. M. Robitaille and L. Berliner. *Ultra High Field Magnetic Resonance Imaging.* 2006.

[5] P. B. Roemer, W. A. Edelstein, C. E. Hayes, S. P. Souza, and O. M. Mueller. "The NMR phased array". In: *Magn Reson Med, vol. 16, no. 2* (1990).

[6] S. M. Wright, R. L. Maginv, and J. R. Kelton. "Arrays of mutually coupled receiver coils: theory and application". In: *Magn Reson Med, vol. 17, no. 1* (1991).

[7] D. K. Sodickson, C. A. McKenzie, M. A. Ohliger, E. N. Yeh, and M. D. Price. "Recent advances in image reconstruction, coil sensitivity calibration, and coil array design for SMASH and generalized parallel MRI". In: *MAGMA, vol. 13, no. 3* (2002).

[8] J. Rousseau, P. Lecouffe, and X. Marchandise. "A new, fully versatile surface coil for MRI". In: *Magnetic Resonance Imaging, vol. 8, no. 4* (1990).

[9] M. Woytasik et al. "Characterization of flexible RF microcoils dedicated to local MRI". In: *Microsystem Technologies, vol. 13, no. 11–12* (2007).

[10] J. R. Corea et al. "Screen-printed flexible MRI receive coils". In: *Nature Communications, vol. 7* (2016).

[11] B. Gruber and S. Zink. "Anatomically adaptive local coils for MRI Imaging – Evaluation of stretchable antennas at 1.5T". In: *ISMRM 24th Annual Meeting and Exhibition* (2016).

[12] J. A. Nordmeyer-Massner, N. De Zanche, and K. P. Pruessmann. "Mechanically adjustable coil array for wrist MRI". In: *Magnetic Resonance in Medicine, vol. 61, no. 2* (2009).

[13] M. M. Ahmad et al. "Catheter-based flexible microcoil RF detectors for internal magnetic resonanceimaging". In: *J. Micromech. Microeng., vol. 19* (2009).

[14] B. Wu et al. "Flexible transceiver array for ultrahigh field human MR imaging". In: *Magnetic Resonance in Medicine, vol. 68, no. 4* (2012).

[15] B. L. Stehouwer et al. "7T versus 3T contrast-enhanced breast Magnetic Resonance Imaging of invasive ductulolobular carcinoma: First clinical experience". In: *Magnetic Resonance Imaging, vol. 31, no. 4* (2013).

[16] R. R. Ernst, G. Bodenhausen, and A. Wokaun. *Principles of nuclear magnetic resonance in one and two dimensions*. 2004.

[17] P. C. Molgero Da Rós, W. Costa e Silva, D. Grabauskas, V. H. Perez, and H. Ferreira de Castro. "Biodiesel from babassu oil: Characterization of the product obtained by enzymatic route accelerated by microwave irradiation". In: *Ind. Crops Prod., 52* (2014).

[18] M. R. Avhad and J. M. Marchetti. "A review on recent advancement in catalytic materials for biodiesel production". In: *Renewable Sustainable Energy Rev., 50* (2015).

[19] David M. Pozar. *Microwave Engineering, 4ed.* 2012.

[20] R. F. Harrington. *Time-Harmonic Electromagnetic Fields*. 1961.

[21] Robitaille PML. "On SAR's, RF power requirements and intrinsic MRI sensitivity at 8.0 tesla". In: *Proceedings of workshop on new insights into safety and compatibility issues affecting in vivo MR, International Society for Magnetic Resonance in Medicine* (1998).

[22] IEC Internation Electrotechnical Comission IEC Standard 60 601-2-33:2010 2010. *Medical electrical equipment part 2–33: particular requirements for the basic safety and essential performance of magnetic resonance equipment for medical diagnosis*. 2010.

[23] C. M. Collins, S. Li, and M. B. Smith. "SAR and B1 field distributions in a heterogeneous human head model within a birdcage coil. Specific energy absorption rate". In: *Magn Reson Med, vol. 40, no. 6* (1998).

[24] D. I. Hoult and N. S. Ginsberg. "The quantum origins of the free induction decay signal and spin noise". In: *J. Magn. Reson., vol. 148, no. 1* (2001).

[25] C. M. Collins et al. "Temperature and SAR calculations for a human head within volume and surface coils at 64 and 300 MHz". In: *J Magn Reson Imaging, vol. 19, no. 5* (2004).

[26] G. Eichfelder and M. Gebhardt. "Local specific absorption rate control for parallel transmission by virtual observation points". In: *Magn Reson Med, vol. 66, no. 5* (2011).

[27] Y. Zhu, L. Alon, C. M. Deniz, R. Brown, and D. K. Sodickson. "System and SAR characterization in parallel RF transmission". In: *Magn Reson Med, vol. 67, no. 5* (2012).

[28] I. Graesslin et al. "A specific absorption rate prediction concept for parallel transmission MR". In: *absorption rate prediction concept for parallel transmission MR,"* (2012).

[29] E. Zastrow J. Córcoles and N. Kuster. "On the estimation of the worst-case implant-induced RF-heating in multi-channel MRI". In: *Phys Med Biol, vol. 62, no. 12* (2017).

[30] D. O. Brunner, J. Paska, J. Froehlich, and K. P. Pruessmann. "SAR assessment of transmit arrays: Deterministic calculation of worst- and best-case performance". In: *Proceedings of the ISMRM, Honolulu, Hawaii, USA* (2009).

[31] E. Neufeld, M.-C. Gosselin, M. Murbach, A. Christ, E. Cabot, and N. Kuster. "Analysis of the local worst-case SAR exposure caused by an MRI multi-transmit body coil in anatomical models of the human body". In: *Phys Med Biol, vol. 56, no. 15* (2011).

[32] M. Murbach et al. "Virtual population-based assessment of the impact of 3 Tesla radiofrequency shimming and thermoregulation on safety and B1 + uniformity". In: *Magn Reson Med, vol. 76, no. 3* (2016).

[33] E. Mattei, G. Calcagnini, F. Censi, M. Triventi, and P. Bartolini. "Role of the lead structure in MRI-induced heating: In vitro measurements on 30 commercial pacemaker/defibrillator leads". In: *Magn Reson Med, vol. 67, no. 4* (2012).

[34] G. J. Metzger et al. "Dynamically Applied B1+ Shimming Solutions for Non-Contrast Enhanced Renal Angiography at 7.0 Tesla". In: *Magn Reson Med, vol. 69, no. 1* (2013).

[35] J. Thomas Vaughan and John R. Griffiths. *RF Coils for MRI*. 2012.

[36] T. K. Foo, C. E. Hayes, and Y. W. Kang. "An analytical model for the design of RF resonators for MR body imaging". In: *Magn Reson Med, vol. 21, no. 2* (1991).

[37] F. W. Grover. *Inductance Calculations: Working Formulas and Tables*. 2004.

[38] C. Puddu, A. Fanti, N. Curreli, and G. Mazzarella. "Challenging the lumped birdcage coil model for high-field MRI". In: *Loughborough Antennas and Propagation Conference* (2014).

[39] J. Mispelter, M. Lupu, and A. Briguet. *NMR Probeheads for Biophysical and Biomedical Experiments: Theoretical Principles and Practical Guideline*. 2006.

[40] X. Zhang, K. Ugurbil, and W. Chen. "Microstrip RF surface coil design for extremely high-field MRI and spectroscopy". In: *Magn Reson Med, vol. 46, no. 3* (2001).

[41] *Federal Communications Comission - Body Tissue Dielectric Parameters*. URL: https://www.fcc.gov/general/body-tissue-dielectric-parameters.

[42] *8720C Microwave Network Analyzer Keysight (formerly Agilent's Electronic Measurement)*. URL: https://www.keysight.com/en/pd-1000002254%3Aepsg%3Apro-pn-8720C/microwave-network-analyzer?cc=IT&lc=ita.

[43] "Bioelectrical impedance analysis in body composition measurement: National Institutes of Health Technology Assessment Conference Statement". In: *Am. J. Clin. Nutr., vol. 64, no. 3 Suppl* (1996).

Chapter 5

[1] K Finkenzeller. *RFID Handbook: Fundamentals and Applications in Contactless Smart Cards and Identification*. 2003.

[2] D.M. Dobkin. *The RF in RFID: UHF RFID in Practice*. 2012.

[3] J.-C. Chiao and D. Kissinger. "Medical Applications of RF and Microwaves—Applications and Events". In: *IEEE Microw.,* (2015).

[4] K.N. Bocan and E. Ervin Sejdic. "Adaptive Transcutaneous Power Transfer to Implantable Devices: A State of the Art Review". In: *Sensors* (2016).

[5] G. Borelli, F.V. Caredda, A. Fanti, G. Gatto, G. Mazzarella, P.F. Orrù, and F. Zedda. "Preliminary study of RFID technologies for healthcare applications". In: *Proceedings of the 23rd Congress of the International Federation of Hospital Engineering (IFHE)* (2014).

[6] G. Borelli, F.V. Caredda, A. Fanti, G. Gatto, G. Mazzarella, R. Montanari, P.F. Orrù, A. Volpi, and F. Zedda. "Healthcare Supply Chain optimization: A comparison between two RFID-based reengineered processes". In: *Proceedings of the Summer School Francesco Turco* (2014).

[7] R. Davis, J. Gottschall, A. Gutierrez, C. Hohberger, D. Veeramani, and J. Holcombe. "Absence of acute adverse in vitro effects on AS-1 RBCs and whole blood–derived platelets following prolonged exposure to 13.56 MHz radio energy". In: *Transfusion* (2010).

[8] R. Knels, P. Ashford, F. Bidet, W. Böcker, et al. "Guidelines for the use of RFID technology in transfusion medicine". In: *Int. J. Blood Transf. Med.* (2010).

[9] R. Davis and A. Gottschall J.and Gutierrez. "Cellular and Protein Impact of RF Energy on Red Cells and Platelets". In: *Report to the FDA; Food and Drug Administration: Silver Spring, MD, USA* (2008).

[10] R. Davis, J. Gottschall, and A. Gutierrez. "Temperature Impact of High RF Energy on Blood Products". In: *Report to the FDA; Food and Drug Administration: Silver Spring, MD, USA* (2008).

[11] C. Hohberger and J. Gottschall. "Joule Heating of Blood Products by Intense RF Magnetic Fields". In: *Report to the FDA; Food and Drug Administration: Silver Spring, MD, USA* (2008).

[12] "International Organization for Standardization. ISO/IEC 18000-3:2010, Information Technology—Radio Frequency Identification for Item Management—Part 3: Parameters for Air Interface Communications at 13,56 MHz". In: *ISO: Geneva, Switzerland* (2010).

[13] A. Fanti, R. Secci, G. Boi, S. Casu, G.A. Casula, G. Mazzarella, and G. Montisci. "A polycarbonate RFID tag for blood chain tracking". In: *Proceedings of the 2015 IEEE International Symposium on Antennas and Propagation and USNC/URSI National Radio Science Meeting, Vancouver, BC, Canada* (2015).

[14] Q.-L. Wang, X.-W. Wang, H.-L. Zhuo, C.-Y. Shao, J. Wang, and H.-P. Wang. "Impact on storage quality of red blood cells and platelets by ultrahigh-frequency radiofrequency identification tags". In: *Transfusion* (2011).

[15] R. Otin. "Numerical study of the thermal effects induced by a RFID antenna in vials of blood plasma". In: *Prog. Electromagn. Res. Lett.* (2011).

[16] C.R. Paul. *Introduction to Electromagnetic Compatibility*. 1992.

[17] IEEE Antennas and Propagation Society. "IEEE Standard Definitions of Terms for Antennas 145-2013". In: *IEEE: New York, NY, USA* (2013).

[18] European Telecommunications Standards Institute. ETSI 302 208-1 ERM. "RFID Operating in the Band 865 MHz to 868 MHz with Power Levels up to 2 W, Part 1: Technical Requirements and Methods of Measurement". In: *ETSI: Sophia Antipolis, France* (2011).

[19] C.A. Balanis. *Modern Antenna Handbook*. 2008.

[20] *Promedical s.r.l.* 2016. URL: http://www.promedical.it.

[21] P.S. Ray. "Broadband complex refractive indices of ice and water". In: *Appl. Opt., 11* (1972).

[22] In: ().

[23] M. Weiland and T. Clemens. "Discrete electromagnetism with the finite integration technique". In: *Prog. Electromagn. Res. Lett., 32,* (2001).

[24] International Commission on Non-Ionizing Radiation Protection (ICNIRP). "ICNIRP statement on the 'Guidelines for limiting exposure to time-varying electric, magnetic, and electromagnetic fields (up to 300 GHz)'". In: *Health Phys.* (2009).

[25] J.-P. Berenger. "A perfectly matched layer for the absorption of electromagnetic waves". In: *J. Comput. Phys.* (1994).

[26] *IFAC—Dielectric Properties of Body Tissues*. 2016. URL: http://niremf.ifac.cnr.it/tissprop/.

[27] J. Van Bladel. "Field singularities at metal-dielectric wedges". In: *IEEE Trans. Antennas Propag., 33* (1985).

List of publications

Articles

[1] Desogus F., Casu S., Muntoni G., Bruno Lodi M., and Schirru L. "Design and simulation of a RF resonant reactor for biochemical reactions". In: *Chemical Engineering Transactions, Year 2016, Volume 52, Pages 1183-1188* (2016).

[2] Desogus F., Fanti A., Casu S., Spanu M., Bruno Lodi M., Mazzarella G., and Bisceglia B. "Use of microwaves for disinfection of farmland: A feasibility study". In: *Chemical Engineering Transactions, Year 2016, Volume 52, Pages 1195-1200* (2016).

[3] A. Fanti, S. Casu, F. Desogus, N. Djuric, and G. Mazzarella. "Design and optimization of a microwave irradiated and resonant continuous biochemical reactor". In: *Radio Science, Volume: 51, Issue: 7* (2016).

[4] A. Fanti, S. Casu, and G. Mazzarella. "A Numerical Estimation of a RFID Reader Field and SAR inside a Blood Bag at UHF". In: *Electronics, Volume 5 Issue 4, pag. 77* (2016).

[5] Spanu M., Fanti A., Bruno Lodi M., Casu S., Desogus F., Bisceglia B., and Mazzarella G. "Microwaves disinfection of farmland". In: *Journal of Electromagnetic Waves and Applications, Volume 30, Issue 16* (2016).

[6] Fanti A., Casu S., Desogus F., Montisci G., Simone M., Casula G.A., Maxia P., Mazzarella G., and Carta R. "Evaluation of a microwave resonant cavity as a reactor for enzyme reactions". In: *Journal of Electromagnetic Waves and Applications, Volume 29, Issue 17* (2015).

[7] Casu S., Fanti A. Lodi M.B., Spanu M., Desogus F., and G Mazzarella. "Numerical Estimation of Agricultural Raised Beds Microwave Disinfection". In: *Radio Science* (2018).

Conferences

[1] Robustness of 7T-MRI flexible array coil behaviour. "A. Melis and S. Casu and C. Puddu and A. Fanti and N. Djuric and G. Mazzarella and F. Maggiorelli and A. Retico and G. Tiberi". In: *Loughborough Antennas and Propagation Conference* (2017).

[2] A. Melis, S. Casu, A. Fanti, G. Mazzarella, Claudio Puddu, and P. Boccacci. "Robustness of flexible 7T-MRI coil behaviour". In: *International Applied Computational Electromagnetics Society Symposium - Italy (ACES)* (2017).

[3] M. B. Lodi, A., and Sergio Casu. "Analysis of superparamagnetic scaffolds: For bone tissue engineering in static magnetic and dynamic fields". In: *Loughborough Antennas and Propagation Conference* (2016).

[4] M. Spanu, M. B. Lodi, A. Fanti, S. Casu, F. Desogus, and G. Mazzarella. "A feasibility study for disinfection of farmland using microwaves". In: *Loughborough Antennas and Propagation Conference* (2016).

[5] Desogus F. and G. Casu S. Muntoni. "Design of a chemical reactor under microwave irradiation in resonance conditions". In: *EFFICIENCY, COST, OPTIMIZATION, SIMULATION AND ENVIRONMENTAL IMPACT OF ENERGY SYSTEMS (ECOS)* (2016).

[6] S. Casu, A. Fanti, N. Djuric, F. Desogus, and G. Mazzarella. "Microwave resonant cavity as a reactor for the enzymatic hydrolysis of sucrose". In: *IEEE 15th Mediterranean Microwave Symposium (MMS)* (2015).

[7] G. Muntoni, S. Casu, A. Fanti, and G. Mazzarella. "A simple model for SE evaluation of MWCNT composite". In: *Loughborough Antennas and Propagation Conference* (2015).

[8] S. Casu, A. Fanti, V. Floris, G. Gatto, G. Mazzarella, M. D. Migliore, and I. L. Spano. "Evaluation of the effects of UHF electromagnetic fields on a blood bag". In: *Loughborough Antennas and Propagation Conference (LAPC)* (2015).

Acknowledgments

I would like to thank all the people I met in this three year long journey.

First, I'd like to thank my advisor prof. Giuseppe Mazzarella for his technical support, my co-advisor Alessandro Fanti and all the people of the electromagnetic group.

I want to thank Francesco Desogus for his help on the multidisciplinary aspects on part of my work.

Thanks to all the other Ph.D students of the group, Marco, Luca, Nicola and Matteo, with a special thanks to my travel mate, Giacomo, author of the funniest translations I've ever heard in my life. It was easier to tread this path in good companion.

Also a special thanks goes to Riccardo with whom I have shared all the turning points of the last years... and thanks to all the students that have stopped for a while in the laboratory, Andrea, I will always owe you a breakfast, Davide, I will never forget the great results we achieved, Michele the keeper of my spot, Nicola with all his stories, Stefania for her free psychoanalysis sessions on me and Nicola, Alessandra, for her jokes on my outfit, Ilenia for her pranks, Paola, I hope you're doing great, and all the others... I didn't realize you were so many until now.

Finally, the biggest thanks goes to my family, for their suggestions and their support always there.